PLASMONIC GOLD NANOHELICOID MEDIATED CHIRAL LIGHT-MATTER INTERACTION

GAO HAN

PhD

The Hong Kong Polytechnic University

2022

The Hong Kong Polytechnic University

Department of Electrical Engineering

Plasmonic Gold Nanohelicoid Mediated Chiral Light-matter Interaction

GAO HAN

A thesis submitted in partial fulfilment of the requirements for the degree of Doctor of Philosophy

Jan 2022

CERTIFICATE OF ORIGINALITY

I hereby declare that this thesis is my own work and that, to the best of my knowledge and belief, it reproduces no material previously published or written, nor material that has been accepted for the award of any other degree or diploma, except where due acknowledgement has been made in the text.

_____(Signed)

GAO HAN_____(Name of student)

Abstract

Chiral light-matter interaction attracts significant interests in classical and quantum optics due to its underlying applications in quantum communication, all-optical selection and separation, and biosensing, etc. Chiral plasmonic nanostructures can uniquely and controllably enhance the chiral light-matter interaction effectively at the nanoscale. Top-down lithography techniques are applied to fabricate plasmonic chiral nanostructures with two-dimensional geometries, and it has remained challenging to prepare three-dimensional nanostructures. Recently, a bottom-up wet-chemistry strategy has been developed for synthesizing nanoparticles with innate chirality. Chiral gold nanohelicoids (GNHs) with intense chiroptical activity are synthesized in the presence of chiral amino acids/ peptides. These GNHs with intrinsic chiral structures open a new pathway for building up nanophotonic systems with single chiral nanostructures. To unleash the great potential in nanophotonics, it is important to unravel the underlying mechanism responsible for the interaction between chiral light and these GNHs. This thesis reports the GNH-mediated chiral light-matter interaction by investigating the interaction between the GNHs and chiral light, an achiral photonic microcavity, and chiral molecules.

Firstly, I present a thorough study on the chiral excitation and emission properties of GNHs at the single-particle level to deeply understand the chiroptical properties of the GNHs. The photoluminescence (PL) of a single GNH under circular light excitation is also circularly polarized, and the polarization-resolved PL spectroscopy

of chiral PL signals have a preferential handedness to the excitation polarization. Two physical models are developed to understand these experimental observations.

Based on the understanding of the GNH's chiral absorption and emission properties, I subsequently investigate the effect of electromagnetic coupling between the GNH and an achiral photonic microcavity in the chiral Purcell enhancement of the hybrid system. The present of the GNH on the SiO_2/Si FP cavity introduces an additional phase change at their interface, leading to compound peaks spectrally detuned from the original FP modes. Importantly, the introduced GNHs on the SiO_2/Si substrate could modulate the Si Raman signals in a chiral manner, demonstrating the effectiveness of chiral modulation in the local near-field regime.

Finally, to extend the chiral light-matter interaction of the GNH with chiral active materials, and further explore the feasibility of GNHs in practical applications, I combine the GNHs with chiral molecules for enantioselective recognition by Raman spectroscopy. In the presence of GNHs, I observe a significant difference in the Raman scattering signal intensities of two enantiomers probably due to surface-enhanced chiral Raman scattering.

In summary, the chiral excitation and emission characteristics of the GNH reveals the relationship between the handedness of chiral emitters and incident circular polarization states. Chiral scatterometry and Raman scattering of the GNH-FP hybrid cavity extends the coupling of localized surface plasmon resonances and FP modes to the chiral regime with an enhanced chiroptical effect. Pairing the use of GNHs with chiral molecules' recognition through Raman spectroscopy reports underlying appli-

cations of the GNHs in chirality-based biosensing and probing. Those works on plasmonic GNHs provide comprehensive insights of chiral light-matter interaction mechanisms of chiral plasmonic nanostructures, and thus flourish their applications in chiral imaging, photonic circuits, and enantio-discrimination.

List of Publications

Journal publications based on this thesis work:

([#] equally contributed, * corresponding author)

1. Z. L. Cao[#], **H. Gao**[#], M. Qiu, W. Jin, S. Z. Deng, K.-Y. Wong, D. Y. Lei*, "Chirality transfer from sub-nanometer biochemical molecules to sub-micrometer plasmonic metastructures: Physiochemical mechanisms and biosensing opportunities", Advanced Materials 32 (41), 1907151 (2020)

2. **H. Gao**[#], P. G. Chen[#], T. W. Lo, W. Jin, D. Y. Lei*, "Selective Excitation of Polarization-steered Chiral Photoluminescence in Single Plasmonic Nanohelicoids", Advanced Functional Materials 2101502 (2021)

Acknowledgement

My PhD study would not have been gone on well without the kind help and invaluable support of many people.

First and foremost, I would like to express my deepest thanks to my chief supervisor, Prof. Wei Jin. He understood the stress and anxiety a PhD student would suffer, and he spared no effort to help me solve all the problems I met. Without his support, I would have quit my PhD study at the very beginning. I also want to thank my co-supervisor Dr. Dangyuan Lei. Under his supervision, I got to know that while doing the research work, being independent is the most important merit of being a mature researcher, and how important to protect your own research work. In addition, I would express my grateful thanks to Prof. Haitao Huang. It is because of his support that, I could finish most of my experiments in the Department of Applied Physics in PolyU.

I would also like to express my grateful thanks to many of my lab-mates. Dr. Siqi Li is the person who taught me the basic things about chemical experiments. He was always willing to share his experimental experience and ideas with me. It is due to his help and suggestions that I am able to get started in my PhD research work. During the time doing my two important PhD projects, Peigang Chen helped me on the simulation calculations and theory explanation. Without his efforts, the two works could not have been finished perfectly. Dr. Tsz Wing Lo and Dr. Danjun Liu were always prepared and willing to instruct me on how to perform the operations of many characterization machines. Though the research study did not start well, it is my luck to have

had guidance from these lab-mates.

I have also received much support from many people. Prof. Yongmin Liu, my previous master supervisor, enlightened me during many of my confusions on how to be a PhD student and how to get along with supervisors. He also gave me helpful suggestions on my research work. Dr. Jianzhong Zheng taught me many useful experimental and article writing skills, and he gave me many supports, both on research and daily life. Dr. Wei Ma and Yihao Xu were always well-prepared to help me solve my research problem and listen to the awful things that had happened to me. XingXing Xu and Yingzhen Hong were always by my side and accompanied me during all my happy and tough times in Hong Kong.

Lastly, I would like to thank my parents, for their incredible love, support and sacrifices. Three years of PhD study is the hardest and the most stressful time I have ever had. Without their inspiration and support, I would not have had the determination and power to accomplish my PhD work in Hong Kong.

Table of Contents

Abstract ..... **I**

List of Publications ..... **IV**

Acknowledgement ..... **V**

List of Figures ..... **X**

Chapter 1 Introduction **1**

1.1 Overview of nanoscale light-matter interactions 1

1.2 The Purcell effect in optical resonators 3

1.3 Propagating surface plasmon polaritons and localized surface plasmon resonances 5

1.4 Circular dichroism 8

1.4.1 Circular dichroism of chiral molecules 8

1.4.2 Plasmonic circular dichroism 10

1.5 Outline of the thesis 12

Chapter 2 Synthesis and characterization of gold nanohelicoids **14**

2.1 Overview of chiral plasmonic nanostructures 14

2.2 Chemical synthesis of gold nanohelicoids 17

2.3 Structural characterization gold nanohelicoids 18

Chapter 3 Chiral photoluminescence from gold nanohelicoids **24**

3.1 Introduction 24

3.1.1 Single-photon photoluminescence of gold nanoparticles 24

3.1.2 Circularly polarized luminescence 27

3.2 Experimental methodology 30

3.2.1 Sample preparation 30

3.2.2 Single-particle scattering and photoluminescence spectroscopy 30

3.3 Chiral photoluminescence in single gold nanohelicoids 32

3.3.1 Selective excitation of polarization-steered chiral photoluminescence 32

3.3.2 A phenomenological model for chiral photoluminescence 39

3.3.3 Super-chiral near-field enhancement and the chiral Purcell effect ..43
3.4 Conclusion 49
Chapter 4 Gold nanohelicoid modulated chiral Raman scattering through a Fabry-Perot cavity 50
4.1 Introduction 50
4.1.1 Chiral gold nanoparticle modulation in nanophotonic systems 50
4.1.2 Fabry-Perot optical cavity 51
4.1.3 Fabry-Perot cavity coupled with plasmonic nanostructures 53
4.1.4 The chiral Purcell effect in a gold nanohelicoid-FP cavity coupling system 55
4.2 Experimental methodology 57
4.2.1 Sample preparation 57
4.2.2 Single-particle scattering and Raman spectroscopy 58
4.3 Gold nanohelicoid modulated chiral Raman scattering through a Fabry-Perot Cavity 58
4.3.1 Gold nanohelicoid modulated chiral Raman scattering 58
4.3.2 An extended chiral-modulated Fabry-Perot cavity model 67
4.4 Conclusion 73
Chapter 5 Gold nanohelicoids based chiral molecule recognition using Raman spectroscopy 75
5.1 Introduction 75
5.1.1 Raman spectroscopy 75
5.1.2 Surface enhanced Raman spectroscopy 76
5.1.3 Raman optical activity 78
5.2 Experimental methodology 81
5.2.1 Sample reparation 81
5.2.2 Raman characterization 82
5.3 Gold nanohelicoid assisted Raman enantioselective recognition 83
5.4 Conclusion 87
Chapter 6 Summary and outlook 89

6.1 Conclusion 89

6.2 Future perspective 91

Appendices 93

(A) Design of the optical path to realize circularly polarized light excitation ..93

(B) ITO substrate influence on gold nanohelicoid chiral photoluminescence ..96

(C) Geometric handedness dependent chiral photoluminescence 97

(D) Gold nanohelicoid modulated chiral Raman scattering on SiO_2/Si substrate with different thicknesses 100

References 103

List of Figures

Figure 1.1 The major developments of light and matter research.[1] 2

Figure 1.2 Schematic illustration of the nanoscale resonator with mode volume radiation losses V.[19] 5

Figure 1.3 Illustration of surface plasmon polaritons and localized surface plasmon resonances. Collective oscillation of electrons excited by incident electromagnetic field at (a) gold-air interface and in (b) gold (Au) nanoparticles.[27] 7

Figure 1.4 Schematic illustration of two approaches to realize plasmonic circular dichroism. (a) Dipole-dipole interaction. (b) Chiral plasmonic nanostructure.[43] 11

Figure 2.1 (a) Chiral twisted stacked crosses.[61] (b) Tapered gold helices.[63] (c) Gold nanoparticles bonded on DNA origami formed left- and right-handed helix structures.[64] 15

Figure 2.2 Schematic of geometric evolution of different gold nanohelicoids.[69] 16

Figure 2.3 Grouping of scanning electron microscopy (SEM) images of (a) left- and (b) right-handed gold nanohelicoids (GNH) with sizes ranging from 120-150 nm. Insets are the corresponding three-dimensional (3D) chiral constructs. Zoomed in SEM images of (c) left- and (b) right-handed GNH. Blue arrows and white dashed lines (linking the orange vertices) assert the helicity of the GNH enantiomers. 19

Figure 2.4 (a) Schematics of the CD and extinction measurements of the GNHs solution. (b) Experimental extinction (solid line) and calculated extinction, scattering and absorption (dashed blue, green, and red lines, respectively) spectrums of the left-handed GNH in CTAB aqueous solution. (c) Experimental (solid lines) and calculated (dashed lines) CD spectrums of

the left-handed GNH (L-GNH) and right-handed (R-GNH). In the calculated spectrums, the crests and trough at around 700 nm may be attributed to the difference between the real morphology and the simplified ideal model. (d) Experimental *g*-factor spectrums of GNHs with different handedness. 21

Figure 2.5 The simplified 3D model and monitored cross section of the gold nanohelicoid. Blue shadowed area indicates the cross-section shape of the monitor. 22

Figure 2.6 (a) Simulated electric near-field intensity distribution for an R-GNH under 593.5 nm LCP excitation. (b) Simulated magnetic near-field intensity distribution for an R-GNH under 593.5 nm LCP excitation. (c) The intensity difference of electric field in an R-GNH under circular polarization excitation. (d) The intensity difference of magnetic field in an R-GNH under circular polarization excitation. 23

Figure 3.1 Illustration of the single-photon photoluminescence (PL). 25

Figure 3.2 (a) PL and scattering spectrums of lithographically made gold nanodisks with different diameters.[76] (b) PL spectrums of a single gold nanorod under 532 nm and 633 nm excitation.[77] (c) PL and scattering spectrum of a single gold nanobipyramid.[78] 26

Figure 3.3 (a) PL spectrums of Al_2O_3 coated gold film with and without single Au NP under 532 nm and 633 nm excitation.[81] (b) PL excitation illustration and spectrums of Au NP dimer on a glass substrate and a thin gold film.[82] 27

Figure 3.4 Schematic illustration of circularly polarized luminescence (CPL).[84] 28

Figure 3.5 Schematic diagram of the nanoassemblies-participated CPL generation, amplification, and applications.[84] 28

Figure 3.6 Schematic illustration of three approaches to realize CPL in nanoassemblies.[84] 29

Figure 3.7 The illustration of single-particle experiment setup for polarization-resolved dark-field scattering and PL measurements. HWP: Half waveplate, QWP: Quarter waveplate, BS: Beam splitter, SPF: 600 nm short pass filter, LPF: 600 nm long pass filter, Pol.: Polarizer, AS: Aperture slot. 32

Figure 3.8 Scattering spectra of a (a) left-handed GNH (L-GNH) and a (b) right-handed GNH (R-GNH) (structure used for the 593.5 nm laser illumination) under white right circularly polarized (RCP i.e., σ^-, red) and left circularly polarized light (LCP i.e., σ^+, green) light illumination. 33

Figure 3.9 (a, b) PL spectrum of a single (a) L-GNH and (b) an R-GNH under RCP (σ^-, red) and LCP (σ^+, blue) laser excitation at 593.5 nm. The PL intensity has a cliff at 600 nm (black dashed line) is attributed to the cut-off response of the long-pass filter applied in the optical path. The solid lines show the Lorentzian fits of the raw data. (c) Scattering spectrums of an achiral nanocube with RCP (red) and LCP (green) light excitation. (d) PL spectrums of an achiral nanocube under RCP (red) and LCP (green) laser excitation at 593.5 nm. 34

Figure 3.10 (a, b) Emission polarization-resolved PL spectrum for the achiral nanocube under the RCP (a) and LCP (b) laser excitation at 593.5 nm. (c-f) Emission polarization-resolved PL spectrum for the L-GNH (c, e) and the R-GNH (d, f) under the RCP (c, d) and LCP (e, f) laser excitation at 593.5 nm. The solid lines show the Lorentzian fits of the raw data. 36

Figure 3.11 (a) PL spectrum of a single L-GNH under RCP (σ^-, red) and LCP (σ^+, blue) laser excitation at 532 nm. (b) Similar results as (a) for a single R-GNH structure. (c-f) Emission polarization-resolved PL spectrum for the L-GNH (c, e) and R-GNH (d, f) under the RCP (c, d) and LCP (e, f) laser excitation at 532 nm. The solid lines show the Lorentzian fits of the raw data. 38

Figure 3.12 Scattering spectra of (a) a L-GNH and (b) an R-GNH used for the

laser excitation conditions in Figure 3.11 (a) and (b), measured under white RCP (σ^-, red) and LCP (σ^+, green) light excitation. 39

Figure 3.13 Schematic graph of the chiral PL process of the chiral nanostructures. Here take the L-GNH under 593.5 nm excitation as an example. The RCP light (red thick upward arrow) generates more d-band electrons of gold to the sp-band based on its larger absorptivity compared to that of the LCP light (green thinner upward arrow). The majority of the energetic electrons transfer to the localized surface plasmon (LSP) band while a minority of them directly recombine with the holes (brown thin downward arrow). Following this, the excited LSPs undergo either radiative decay to generate PL emission (red and green dashed arrows) or non-radiative decay leading to Ohmic loss. The PL emission can be modulated by the geometric chirality of the GNH. 41

Figure 3.14 The L-GNH chiral PL g-factors structure under near-resonant 593.5 nm (upper panel) and off-resonant 532 nm (lower panel) illuminations. Black dots suggest experimental data while orange and green lines indicate calculation results. Blue dashed lines assert the averaged g-factor at the PL crests (shadowed region): 0.12 for the 593.5 nm illumination and 0.1 for the 532 nm illumination. 43

Figure 3.15 (a) Calculated near-field chirality distribution in the R-GNH under LCP 593.5 nm excitation. (b) Calculated near-field chirality distribution in the R-GNH under RCP 593.5 nm excitation. 44

Figure 3.16 (a) The integrated net optical chirality for a L-GNH under RCP (red) and LCP (black) excitation. (b) $\frac{\overline{C^+}}{C_0} + \frac{\overline{C^-}}{C_0}$ represents the totality of the integrated optical chirality for GNHs under RCP and LCP excitation. The non-zero value relates to the chiral antenna mode of the GNHs, with the greatest dissymmetry factor appearing at about 600 nm. For $\lambda > 600$ nm, the parameter $\frac{|\overline{C^-}|}{U^-} - \frac{|\overline{C^+}|}{U^+}$ is negative, which manifests the polarization

steering activity in polarization-resolved PL. 47

Figure 3.17 (a) Calculated dissymmetry contrast *D* of CPL. $D = (I_{LCP} - I_{RCP})/(I_{LCP} + I_{RCP})$. I_{LCP} and I_{RCP} is derived from the x and y component of the electric field as $I_{LCP} = |E_x + iE_y|^2$ and $I_{RCP} = |E_x - iE_y|^2$. CPL spectra of the R-GNH (pink) and L-GNH (blue) under (b) 593.5 nm and (c) 532 nm laser excitation. The solid lines show the Lorentzian fits of the raw data. 48

Figure 4.1 (a) Schematic illustration of chiral gold nanoparticles participated photothermal chirality excitation.[111] (b) Polarization resolved PL emission from WS_2 with and without a chiral nanoparticle on WS_2 under right circularly polarized light excitation. [112].....51

Figure 4.2 Schematic illustration of a Fabry-Perot (FP) cavity with two parallel planar mirrors.[115] 53

Figure 4.3 (a) Cross view of the disc dimer on top of a double layer FP cavity.[127] (b) Schematic illustration of a hybrid nanoparticle-microcavity system. The FP cavity is formed by high refractive index film deposited on low-index substrates.[120] (c) Schematic illustration of an Au nanosphere monomer and dimer on SiO_2/Si FP cavity.[129].....55

Figure 4.4 Enhanced CD of a polarization-preserved cavity. The mirror reflection coefficients are 90.0% (black line) and 99.8% (red line). The refractive index of the chiral molecule is 1.5. The illustration depicts the polarization situation in the two cavities.[102].....57

Figure 4.5 Schematic illustration of a single gold nanohelicoid on the SiO_2/Si FP cavity. 59

Figure 4.6 Scattering spectrums of the (a) L-GNH and the (b) R-GNH structures on the 1000 nm SiO_2/Si substrate measured under white RCP (red) and LCP (green) light illumination. The data are calculated by averaging 8 different GNHs scattering spectrums. Scattering spectrums of an (c) L-GNH and an (d) R-GNH structure on the pure glass substrate measured under white RCP (σ^-, red) and LCP (σ^+, green) light illumination.....61

Figure 4.7 Scattering spectra of an achiral structure on (a) pure Si substrate and (b) 1000 nm SiO_2/Si substrate measured under white RCP (σ^-, red) and LCP (σ^+, green) light illumination. Scattering spectrums of a single L-GNH structure on (c) pure Si substrate and (d) 1000 nm SiO_2/Si substrate under white light illumination with no circular polarization state. 62

Figure 4.8 (a, b) Raman spectrums of the single (a) L-GNH and (b) R-GNH structure on 1000 nm SiO_2/Si substrate under RCP (σ^-, red) and LCP (σ^+, blue) laser excitation at 593.5 nm. (c, d) Raman spectrums of the single (c) L-GNH and (d) R-GNH structure on pure Si substrate under RCP and LCP laser excitation at 593.5 nm.....64

Figure 4.9 (a, b) Raman spectrums of an achiral structure on the (a) 1000 nm SiO_2/Si and (b) pure Si substrate under RCP (σ^-, red) and LCP (σ^+, blue) laser excitation at 593.5 nm. (c, d) Raman spectrums of a (c) bare 1000 nm SiO_2/Si and (d) bare Si substrate under RCP and LCP laser excitation at 593.5 nm.....65

Figure 4.10 (a, b) Raman spectrums of the single (a) L-GNH and (b) R-GNH structure on the 1000 nm SiO_2/Si substrate under RCP (σ^-, red) and LCP (σ^+, blue) laser excitation at 532 nm. (c, d) Raman spectrums of the single (c) L-GNH and (d) R-GNH structure on pure Si substrate under RCP and LCP laser excitation at 532 nm. 66

Figure 4.11 (a) Simulated and calculated relative intensity of the bare 1000 nm SiO_2/Si FP cavity. (b) Simulated and calculated scattering spectra of the GNH on the 1000 nm SiO_2/Si FP cavity. (c) Simulated and calculated relative intensity of the GNH on the 1000 nm SiO_2/Si FP cavity. (d) Electric field distribution of a cross section of the GNH on SiO_2/Si substrate hybrid FP cavity system. 71

Figure 4.12 (a) The simulated (red) and calculated (blue) CD of the GNH on the 1000 nm SiO_2/Si substrate using the FP modulated model. The CD of the GNH on the infinity SiO_2 substrate. (b) The simulated (red) and calculated

(blue) CD difference of the GHN on the 1000 nm SiO_2/Si substrate using the FP modulated model. 73

Figure 5.1 Schematic illustration of Rayleigh scattering and two kinds of Raman scattering processes.[135] 76

Figure 5.2 Number of publications on surface enhanced Raman (SERS) technique research.[139] 77

Figure 5.3 (a) Schematic illustration of SERS process.[136] (b) LSPRs range of Ag, Au and Cu.[139] 78

Figure 5.4 (A) Incident circular polarization (ICP) and (B) scattered circular polarization (SCP) Raman optical activity (ROA) form with incident light of angular frequency ω.[150] 79

Figure 5.5 Molecular structures of cysteine, glutathione, and tryptophan. 82

Figure 5.6 (a) CD spectra of 1 mM L-Cys and D-Cys solution. (b) Raman spectra of pure 10mM L-Cys and D-Cys. 83

Figure 5.7 Raman spectra of (a) L-GNH/ D-Cys and L-GNH/ L-Cys and (b) R-GNH/ D-Cys and R-GNH/ L-Cys at around 497 cm^{-1}. 84

Figure 5.8 The deviation index (Di) curve of L-GNH and R-GNH. 85

Figure 5.9 (a) CD spectra of 10 mM D-Trp and L-Trp solutions. Raman spectra of (b) L-GNH/ D-Trp and L-GNH/ L-Trp and (c) R-GNH/ D-Trp and R-GNH/ L-Trp at around 755 cm^{-1}. 86

Figure 5.10 (a) CD spectra of 100 μM L-GSH solution. (b) Raman spectra of L-GNH/ L-GSH and R-GNH/ L-GSH at around 927 cm^{-1} 86

Figure A1 Beam splitter reflectance profile of the BSW10R. 94

Figure A2 Schematic illustration of circularly polarized light generation with a half-quarter waveplate combination. 95

Figure A3 Beam splitter transmission profile of the BSW10R. 95

Figure A4 (a) Net optical chirality, $\frac{\overline{C^+}}{C_0}+\frac{\overline{C^-}}{C_0}$, and $\frac{|\overline{C^-}|}{U^-}-\frac{|\overline{C^+}|}{U^+}$ of a 150 nm gold nanohelicoid under a 1.32 effective refractive index. (b) $\frac{\overline{C^+}}{C_0}+\frac{\overline{C^-}}{C_0}$ represents

the totality of the integrated optical chirality for GHNs under RCP and LCP excitation with an effective refractive index of 1.32. The non-zero value corresponds to the chiral antenna mode of the GNHs, with the largest dissymmetry factor appearing at about 600 nm. For λ > 600 nm, the parameter $\frac{|\overline{C^-}|}{U^-} - \frac{|\overline{C^+}|}{U^+}$ is negative, which manifests the polarization-steering effect in polarization-resolved PL. 97

Figure A5 (a) SEM image and 3D model of left-handed gold helicoid II (GNH II). (b) Scattering spectra of left-handed GNH II used for 593.5 nm excitation under RCP (red) and LCP (green) white light illumination. (c) CD (orange) and extinction (blue) spectra of left-handed GNH II in an aqueous medium. (d) Experimental *g*-factor spectra of left-handed GNH II. 98

Figure A6 (a) Chiral PL spectra of a left-handed GNH II structure under the illumination of 593.5 nm RCP (red) and LCP (green) laser. (b) Emission polarization-resolved PL spectrum for a left-handed GNH II in (a) under the illumination of 593.5 nm RCP (b) and LCP (c) laser, respectively. The solid line shows the Lorentzian fits of the raw data. 99

Figure A7 CPL spectrum of left-handed GNH II under 593.5 nm illumination. Dots describe the real CPL signal of GNH II. The solid line shows the Lorentzian fits of the raw data. (b) Experimental chiral PL *g*-factor spectra of left-handed GNH II which has an averaged *g*-factor of ~0.17 at the main peak region (shadowed area). The cliff at 600 nm in each PL spectrum (black dashed line) is due to the cut-off wavelength of the long-pass filter used in the optical path. 99

Figure A8 (a-d) Near field optical chirality distribution of right-handed GNH II under LCP (a, c) and RCP excitation (b, d). The colored bar scale of (a) and (b) is modulated to highlight the distribution inside the nanohelicoids. In (c) and (d), an actual optical chirality of 80 can be achieved at the outer corners of the nanostructure. 100

Figure A9 Scattering spectra of a L-GNH on the (a) 100 nm, (b) 300 nm, and (c) 500 nm SiO_2/Si substrate under RCP (σ^-, red) and LCP (σ^+, green) white light illumination. Raman spectra of a single L-GNH on the (d)100 nm, (e) 300 nm, and (f) 500 nm SiO_2/Si substrate under RCP (σ^-, red) and LCP (σ^+, blue) laser excitation at 593.5 nm. (b) Similar results as (d-f) for corresponding same single L-GNH on the (g)100 nm, (h) 300 nm, and (i) 500 nm SiO_2/Si substrate under RCP and LCP laser illumination at 532 nm. 102

Chapter 1 Introduction

1.1 Overview of nanoscale light-matter interactions

The interaction between an oscillating electromagnetic field and the charged particles in the matter results in the classical light-matter interaction. Absorption, fluorescence, and light induced ionization and photochemistry are all common forms of light-matter interaction. Light-matter interaction is pervasive and important in a vast realm of physical processes including atom optics, electrical engineering with frequency, and condensed matter physics. Manipulation of these phenomena enables the development of frontier technologies ranging from atomic transitions to photosynthesis on earth.[1] However, on a subwavelength scale, the light-matter interaction is restricted by the optical diffraction limit.[2, 3] The restriction severely hinders the control of the optical phenomena within the subwavelength regime. Therefore, precise manipulation of light-matter interaction, in particular, in the subwavelength scale, becomes emergent. The appearance of plasmonic can enhance the light-matter interaction effectively, making the light-matter interaction research more important. It should be stressed that, when the sizes of noble metals reach ~100 nm or smaller, these nanostructures possess elusive electronic, optical, and catalytic properties, which are totally different from their bulk counterparts.[4-7] The plasmonic induced strong light-matter interactions can be applied in the field of plasmon-enhanced photoluminescence (PL),[8, 9] surface enhanced Raman scattering (SERS),[10, 11] and plasmon-

enhanced interaction between the molecules.[12]

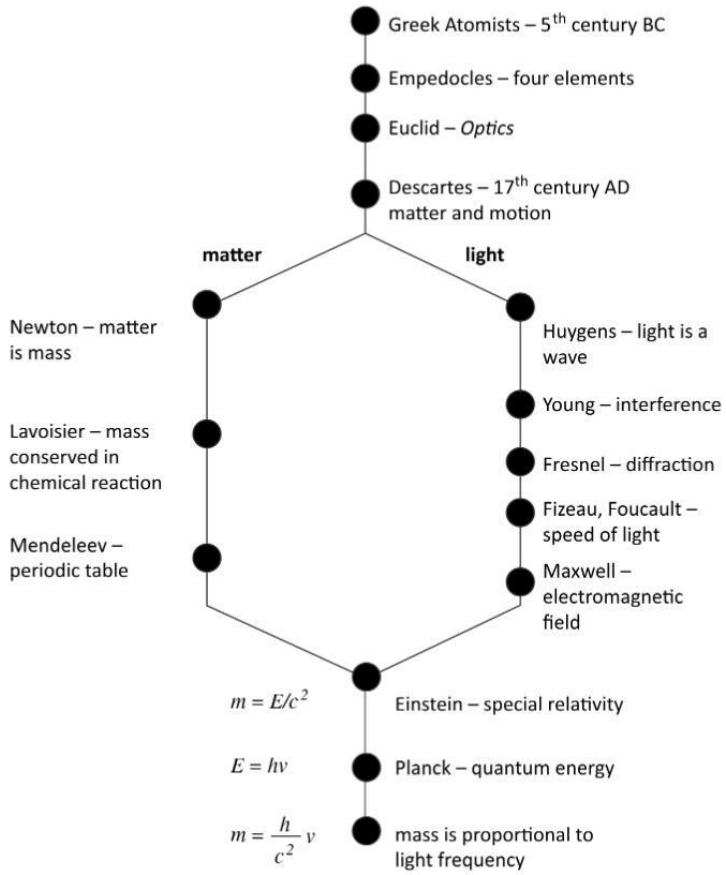

Figure 1.1 The major developments of light and matter research.[1]

When twist light into left- or right-handed state, it produces crucial characteristics which can be used for many chirality-related natural and technological phenomena discrimination. Compared with light-matter interaction, chiral-light matter interaction is more complicated and less studies have been done on it. It has been found that, in the field of pharmaceuticals, the interaction of chiral light with chiral matters is non-invasive to the chiral matters (e.g., chiral molecules), and can hinder the unwanted side-effects. However, the chiral light-matter interaction is also restricted by the optical diffraction limit. Chiral plasmonic nanostructures have drawn great attention

due to their enhancement of chiroptical activity and sensitivity of chiral molecules.[13, 14] Thus, chiral plasmonic materials are essential to broadening the research of chiral light-matter interactions on the nanoscale.

1.2 The Purcell effect in optical resonators

The spontaneous decay rate of a quantum emitter relies on the electromagnetic environment. In the 1940s, Edward Mills Purcell developed the process of increasing the nuclear magnetic transition rates by importing atoms into a resonant cavity.[15] The Purcell effect reflects the spontaneous emission enhancement of a quantum system via its environment. The magnitude of the enhancement, which is expressed by the ratio of the modified emission rates to the free-space emission rates is called the Purcell factor. The introduction of the Purcell factor has allowed a path to of light-matter interaction studies.

The derivation of the Purcell factor starts from Fermi's Golden rule. For an achiral emitter and its spontaneous decay rate is expressed as:[16, 17]

$$\Gamma = \frac{2\pi}{\hbar^2} |\mathbf{p} \cdot \mathbf{E}(\mathbf{r})|^2 \rho(\omega) \tag{1.1}$$

where $\mathbf{p}$ is an electric dipole of the emitter, and $\rho(\omega)$ is the density of electromagnetic modes at the frequency ω. Semi-classical normalization factor α is used to normalize the classical electric fields $\mathbf{E}(\mathbf{r})$ of the cavity mode, which is given by:[17]

$$\alpha^2 = \frac{2\pi\hbar\omega_0}{\int \varepsilon(\mathbf{r})|\mathbf{E}_{\max}(\mathbf{r})|^2 d^3\mathbf{r}} \tag{1.2}$$

where $|\mathbf{E}_{\max}|^2$ is the intensity of the electric field at the maximum position and ω_0 is the cavity resonant frequency. After normalization, the spontaneous decay rate can be written as:

$$\Gamma = \frac{2\pi}{\hbar^2}\alpha^2|\mathbf{p}|^2|\mathbf{E}_{\max}|^2\rho(\omega)\frac{|\mathbf{E}(\mathbf{r})|^2}{|E_{\max}(\mathbf{r})|^2}\eta^2 \tag{1.3}$$

where η is the orientation factor representing the orientation matching of the electric dipole moment $\mathbf{p}$ and the cavity mode $\mathbf{E}(\mathbf{r})$. η is expressed as:

$$\eta \equiv |\mathbf{p}\cdot\mathbf{E}(\mathbf{r})|/\{|\mathbf{p}|^2|\mathbf{E}(\mathbf{r})|^2\} \tag{1.4}$$

Inside the single mode cavity, the mode density is given by:[16]

$$\rho(\omega) = \frac{2}{\pi\Delta\omega_0}\frac{\Delta\omega_0^2}{4(\omega-\omega_0)^2+\Delta\omega_0^2} = \frac{2Q}{\pi\omega_0}\frac{\omega_0^2}{4Q^2(\omega-\omega_0)^2+\omega_0^2} \tag{1.5}$$

where $\Delta\omega_0$ and $Q \equiv \frac{\omega_0}{\Delta\omega_0}$ are the linewidth and quality factor of the single cavity mode, respectively. The mode volume of the cavity is defined as $V = \int \varepsilon|\mathbf{E}(\mathbf{r})|^2\, d^3\mathbf{r}/(\varepsilon|\mathbf{E}_{\max}|^2)$. The decay rate in free space is $\Gamma_0 = 32n|\mathbf{p}|^2\pi^3/3\hbar\lambda^3$. The spontaneous decay rate normalized by decay rate in the free space is expressed as:

$$\Gamma = F_p\frac{\omega_0^2}{\omega_0^2+4Q^2(\omega-\omega_0)^2}\frac{|\mathbf{E}(\mathbf{r})|^2}{|\mathbf{E}_{\max}(\mathbf{r})|^2}\eta^2 \tag{1.6}$$

The cavity decay rate enhancement is evaluated by the Purcell effect, which is defined as:

$$F_p \equiv \frac{3}{4\pi^2}\left(\frac{\lambda}{n}\right)^3\left(\frac{Q}{V}\right) \tag{1.7}$$

This formula reveals the requirement of the emission rate enhancement in an optical resonator: light confinement down to small dimensions and long-time light storage.[18] The temporal and spatial confinement of light is attributed to the quality factor and the cavity mode volume, respectively.[19] The Purcell factor can be a powerful tool to further understand and control the light-matter interaction in a resonator.

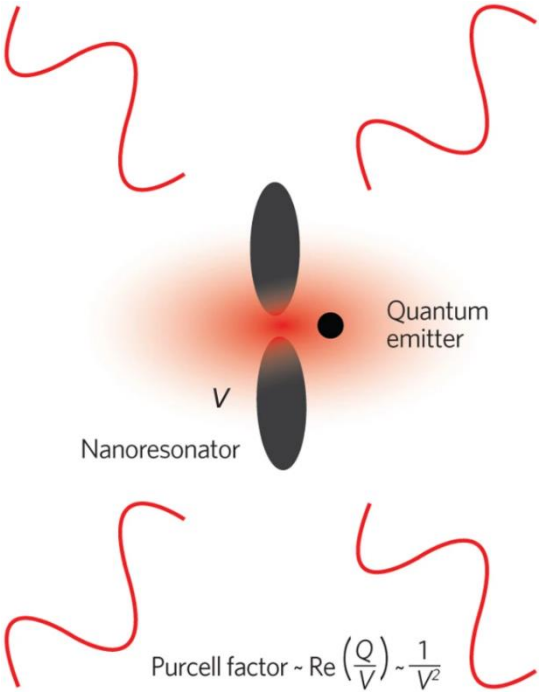

Figure 1.2 Schematic illustration of the nanoscale resonator with mode volume radiation losses V.[19]

Photonic crystal microcavities[20] and plasmonic nanocavities[21] are two common optical resonators which have high quality factors, which in turn could provide extremely high mode confinements. Compared with photonic crystal, plasmonic nanocavities are not confined by the diffraction limit. This is because the light can be restricted on length scales down to the dimensions of the plasmonic nanocavities due to the light coupling to electron oscillations or plasmons in the metal.[22]

1.3 Propagating surface plasmon polaritons and localized surface plasmon resonances

Surface plasmons are defined as the hybrid electron-photon oscillations at the metal-dielectric interface and occur at any metal-dielectric interface.[23] The name and

theoretical description of surface plasmons were raised by Rtichie in 1957.[24] Later on, Andreas Otto, Erich Kretschmann, and Heinz Ritchie came up with the optical excitation of surface plasmons, and two independent approaches for surface plasmon generation were reported.[25] Surface plasmon polaritons (SPPs) are termed as surface bounded mode of coupled collective electron oscillations and electromagnetic wave at the metal-dielectric interface.[26] Generally, SPPs are characterized by dispersion and spatial profile. Owing to the surface mode nature, the SPPs are able to confine light beyond diffraction limit. However, it is impossible to directly excite SPPs with electromagnetic waves. This is because the SPP dispersion relation $\omega(k)$ is below that of free-space light leading to a momentum mismatch between the SPP and free-space light.

In two- or three- dimensionally confined plasmonic nanoparticles, plasmon resonances become highly localized and are defined as localized surface plasmon resonances (LSPRs). LSPRs are collective and non-propagating oscillations of free electrons in the conduction band of metallic nanostructures (Figure 1.3).[27] Compared with SPPs, LSPRs have several distinctive features.[28] First, subwavelength scale plasmonic nanostructure enables the direct coupling of propagation light in free space with the plasmonic localized modes. Second, the LSPRs exhibits higher tunability in the resonance frequency. The wavelengths of LSPRs can be tuned from ultraviolet to near-infrared regions by varying the composition, size, and configuration of the metallic nanocrystals. At last, the LSPRs of metal nanocrystals confine light into localized space, which enhance the near-field significantly. The prominently enhanced optical

density of states leads to strong light-matter interactions and extends the plasmon-enhanced spectroscopy areas,[29] plasmon-enhanced nonlinear effect,[30, 31] as well as plasmon-participated catalytic reactions.[32]

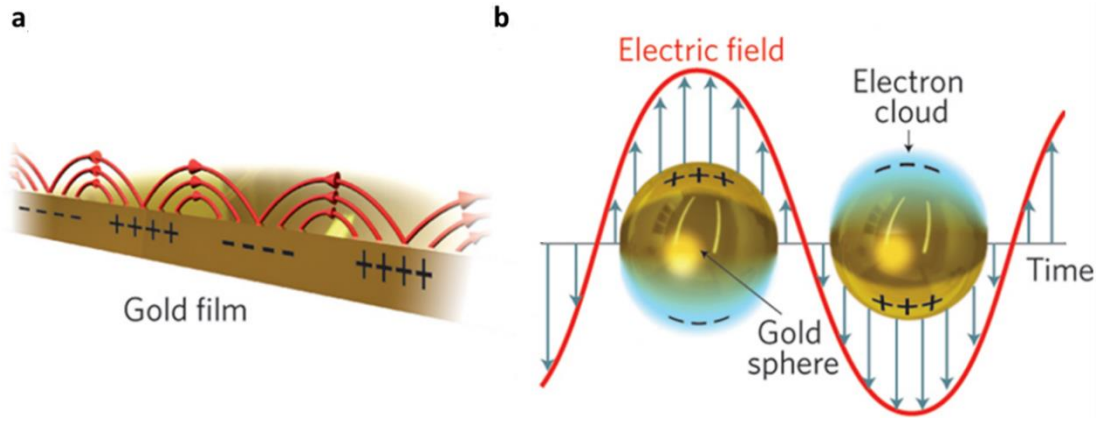

Figure 1.3 Illustration of surface plasmon polaritons and localized surface plasmon resonances. Collective oscillation of electrons excited by incident electromagnetic field at (a) gold-air interface and in (b) gold (Au) nanoparticles.[27]

In the past few years, metal nanocrystals, typically gold (Au) and silver (Ag) nanoparticles (NPs) are the most widely studied plasmonic materials due to their good chemical stability and high electrical conductivity. Thanks to the improvement of numerical methods precise control of noble nanocrystals with different geometries and the appearance of high-sensitivity optical characterization techniques, the 1900s became the period the field of plasmonics rapidly developed. Specifically, dark-field scattering spectroscopy with the help of scanning electron microscopy (SEM) imaging became a useful tool to probe the plasmonic characteristics of nanocrystals at the single-particle level. Subsequently, the plasmon coupling hybridization model[33] and

quantum plasmon resonances of single metallic nanocrystals[34] were reported. Compared to the individual plasmonic nanostructures, the combination of plasmonic nanostructures and molecules could create some new optical responses and modify the plasmon properties of plasmonic nanostructures. In order to recognize the weak chiroptical response of natural entity, the chiral plasmonic system seems promising, which has been developed rapidly in recent years.[35]

1.4 Circular dichroism

1.4.1 Circular dichroism of chiral molecules

Circular dichroism (CD) reflects the absorption difference between left and right circularly polarized (RCP and LCP) light of the same molecular system. CD appears in chiral molecules in which a mirror image could not be superimposed. The handedness of incidence causes the different decay rate of different molecules. If a chiral molecule is strongly coupled to one handed circularly polarized light instead of opposite handed, there will occur a decay rate difference of the molecules. CD originates from the differential decay rate of chiral molecules. CD is an intriguing phenomenon of biomolecules.

Herein, the microscopic origin of CD in chiral molecules is summarized. According to Fermi's Golden Rule, the decay rate of a molecule from the state $|(n-1)(\mathbf{k},h)\rangle$ to the sate $|n(\mathbf{k},h)\rangle$ can be expressed as:

$$\Gamma = \frac{2\pi}{\hbar^2}\rho|V_{\mathrm{fi}}|^2 = \frac{2\pi}{\hbar^2}\rho|\langle(n-1)(\mathbf{k},h)|H_{\mathrm{int}}|n(\mathbf{k},h)\rangle|^2 \quad (1.8)$$

where ρ, V_{fi}, $\mathbf{k}$, are the density of states, transition matrix elements and momentum of light, respectively. $h=L/R$ is the helicity of light, where L and R are denoted as left and right handedness, respectively. A chiral molecule is modeled as an electric dipole $\mathbf{p}$ and magnetic dipole moment $\mathbf{m}$, and the interaction Hamiltonian of a chiral molecule is written as:

$$H_{\text{int}} = -\mathbf{p}\cdot\mathbf{E} - \mathbf{m}\cdot\mathbf{B} \tag{1.9}$$

Substituting Equation 1.9 into the transition matrix elements, we could get:

$$V_{\text{fi}} = -\mathbf{p}\cdot\langle(n-1)(\mathbf{k},\lambda)|\mathbf{E}|n\left(\mathbf{k},\frac{L}{R}\right)\rangle - \mathbf{m}\cdot\langle(n-1)\left(\mathbf{k},\frac{L}{R}\right)|\mathbf{B}|n\left(\mathbf{k},\frac{L}{R}\right)\rangle \tag{1.10}$$

Quantized electromagnetic fields are expressed as:

$$\mathbf{E}(\mathbf{r}) = i\sum_{\mathbf{k},\lambda}\sqrt{\frac{\hbar\omega}{2\varepsilon_0}}\left(\mathbf{e}^{(h)}a^{(h)}(\mathbf{k})e^{i\mathbf{k}\cdot\mathbf{r}} - \mathbf{e}^{-(h)}a^{(h)\dagger}(\mathbf{k})e^{i\mathbf{k}\cdot\mathbf{r}}\right) \tag{1.11}$$

$$\mathbf{B}(\mathbf{r}) = i\sum_{\mathbf{k},\lambda}\frac{1}{C}\sqrt{\frac{\hbar\omega}{2\varepsilon_0}}\left(\mathbf{b}^{(h)}a^{(h)}(\mathbf{k})e^{i\mathbf{k}\cdot\mathbf{r}} - \mathbf{b}^{-(h)}a^{\dagger(h)}(\mathbf{k})e^{i\mathbf{k}\cdot\mathbf{r}}\right) \tag{1.12}$$

In terms of circular polarization, $\mathbf{b}^{L/R}(\mathbf{k}) = \hat{\mathbf{k}}\times\mathbf{e}^{L/R}(\mathbf{k}) = \mp i\mathbf{e}^{L/R}(\mathbf{k})$.

Using the quantized fields, the transition matrix elements are given by:

$$V_{\text{fi}}^{\pm} = \sqrt{\frac{\hbar\omega}{2\varepsilon_0}}\left(-i\mathbf{p} \mp \frac{1}{c}\mathbf{m}\right)\cdot\mathbf{e}^{(L/R)}e^{i\mathbf{k}\cdot\mathbf{r}} \tag{1.13}$$

Because angular momentum operator $\mathbf{L}$ is determined by the magnetic dipole, and it is purely imaginary, that the electric dipole moment $\mathbf{p}$ is purely real and the magnetic dipole is completely imaginary.[36] Thus the rotational averaged spontaneous decay rate can be expressed as:

$$\langle\Gamma_0^{\pm}\rangle = \frac{\omega^3 n}{3\pi\varepsilon_0\hbar c^3}\left(|\mathbf{p}|^2 + \frac{1}{c^2}|\mathbf{m}|^2 \mp \frac{2}{c}\text{Im}[\mathbf{p}\cdot\mathbf{m}]\right) \tag{1.14}$$

Subscript ± denotes the decay rate under the right (-) and left (+) circularly polarized light excitation, respectively. Here, $\rho(\omega) = (\omega^2 n^3/\pi^2 c^3)$, the density of states in the

homogeneous medium of refractive index *n* is used. Consequently, the differential decay rate resulting in CD of chiral molecules can be written as:[37]

$$\Delta\Gamma_0 \equiv \langle\Gamma_0^+\rangle - \langle\Gamma_0^-\rangle = -\frac{4\omega^3 n}{3\pi\varepsilon_0\hbar c^4}\mathrm{Im}[\mathbf{p}\cdot\mathbf{m}] \quad (1.15)$$

For CD spectroscopy, it is a technique based on Beer's law, and directly reflects intensity of CD signals in terms of wavelength. CD spectrum is reported as ellipticity θ, and is measured in units of mdeg.

1.4.2 Plasmonic circular dichroism

Plasmonic CD refers to the CD responses at LSPR region of plasmonic nanomaterials.[38] For the CD spectroscopy sensitivity improvement, plasmonic nanomaterials are good candidates due to their unique optical properties.[39, 40] There are two types of plasmonic circular dichroism. One is the plasmonic CD signaling of achiral plasmonic nanostructures, which originate from the molecular chirality transferring to plasmonic nanostructures. In general, to acquire meaningful CD signals of biochemical molecules with adequate signal-to-noise ratios,[41, 42] a high concentration is required because their chiroptical response is extremely weak and generally appears in the ultraviolet (UV) band. The electronic structures of molecules lead to the UV response, and the weak chiral optical activity results from the dimension difference between UV light (hundreds of nanometers) and molecules (nanometers or below). Consequently, scientists took advantage of plasmon resonance of achiral metallic nanostructures to enhance the electronic transition of adjacent chiral molecules, and

thus, enhanced the CD signals of molecules. At the same time, a new CD signal at the LSPR band of achiral plasmonic materials appears.[43] The interaction between chiral molecules and the achiral plasmonic nanostructure can be explained by a dipole-dipole interaction system. As shown in Figure 1.4a, the resonance of the chiral molecule is regarded as a two-level system with two coupled dipoles: magnetic and electric dipole. The newly induced plasmonic CD signal originates from the Coulombic (dipole and multi-dipole) interactions between chiral analytes and achiral plasmonic nanomaterials.[43-45] Chiral molecules attached to the single achiral nanoparticles,[12, 44, 46] and achiral nanoparticles linked together by chiral molecules are two common approaches to realize the chiral plasmonic activity.[13, 47, 48]

The other type of plasmonic circular dichroism originates from chiral plasmonic nanostructures (Figure 1.4b). Due to the mature technique of metasurface fabrication, metallic nanostructures such as a helix or a spiral can be artificially designed. These nanostructures with distinct handedness exhibit intrinsic chiral responses at their plasmon resonance band. The chiral assembly caused plasmonic circular dichroism mechanism will be discussed in detail in Chapter 2.

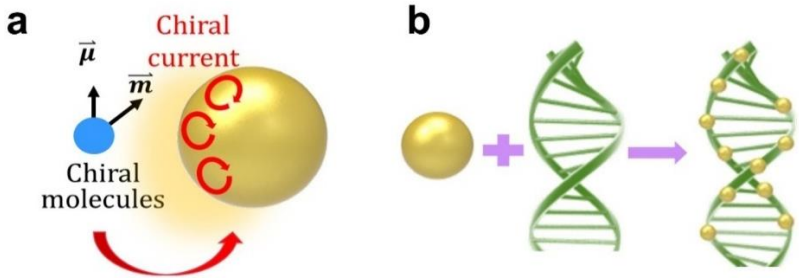

Figure 1.4 Schematic illustration of two approaches to realize plasmonic circular dichroism. (a) Dipole-dipole interaction. (b) Chiral plasmonic nanotructure.[43]

1.5 Outline of the thesis

The thesis is organized as following chapters:

In chapter 1, we first briefly review the light-mater interaction concept and history, followed by an introduction and comparison of SPP and LSPR. Then the Purcell effect in a resonator, and two kinds of plasmonic CDs are summarized.

In Chapter 2, a review of chiral plasmonic nanostructures and works done on single gold nanohelicoids (GNHs) on substrate are given first. In the second part, the synthesis method, optical and morphological properties, as well as simulated electric and magnetic distribution of the GNH used in the work are introduced.

In Chapter 3, a thorough research on chiral PL features of the single GNH is presented. For one specific circular polarization light excited PL, signals of GNH enantiomers have a reverse intensity trend due to different circular dichroism absorption, while the polarization-resolved chiral PL signal is driven by circular polarization.

In Chapter 4, we exploit the scattering spectra properties of the single GNH on a Fabry-Perot (FP) cavity. Two strong scattering peaks with the same intensity contrast towards right and left circularly polarized white light illumination are observed. It is also found that, through the local field modulation of GNHs, the Si Raman signals of the FP cavity could have chiral features.

In Chapter 5, we report the GNH assisted Raman enantioselective recognition of chiral molecules. According to the Raman spectroscopy, three kinds of chiral molecules (cysteine, glutathione, tryptophan) and their handedness can be discriminated

via Raman spectra. The Raman scattering intensity difference between cysteine enantiomers can reach twofold.

In Chapter 6, we summarize the three works done using GNHs and provide some future work that could be done on the single GNHs.

Chapter 2 Synthesis and characterization of gold nanohelicoids

In this chapter, I will briefly review the chiral plasmonic nanostructures and works done on the single GNH. The synthesis method and properties of GNHs are also introduced. The following works in the thesis are all based on the synthesized GNH.

2.1 Overview of chiral plasmonic nanostructures

In chirality related research, chiral plasmonic structures have drawn a lot of attention because of their intense chiroptical signals and strong light-matter interactions compared with pure chiral molecular systems, which paved the way for the development of chiral sensing,[49-51] chiral imaging,[52-54] chirality switching,[55, 56] and polarization manipulation.[57-59]

Chiral plasmonic nanostructures with geometric chirality are the most commonly used chiral plasmonic nanostructures. Two rules can be used to fabricate artificial chiral nanostructures with strong optical chiral response: (1) the electric and magnetic resonances are oriented non-orthogonally; (2) two non-parallel electric resonances are placed in different equiphase planes of the incident light.[60] The two kinds of resonant modes are coupled with each other by the physical connection or near-field.

Conventionally, there are two strategies to make intrinsic chiral plasmonic nanostructures. One is the top-down fabrication technique used to make planar chiral patterns[61, 62] or three-dimensional (3D) chiral nanostructures;[57, 63] the other is the bot-

tom-up method in which chiral molecules like DNA,[56, 64, 65] phospholipids,[66] or peptides[67] act as links or templates to assist metallic particles forming chiral configurations (Figure 2.1).

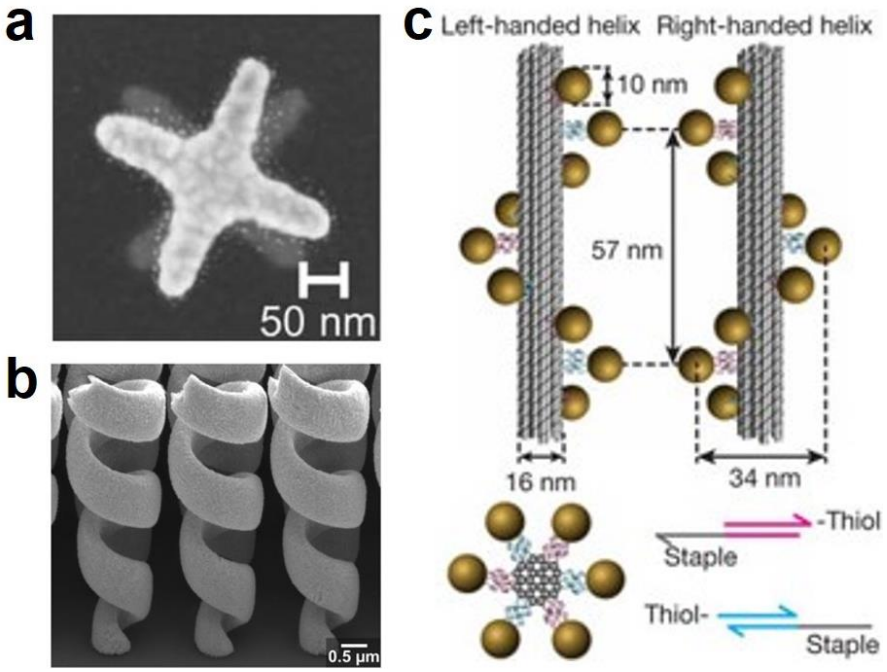

Figure 2.1 (a) Chiral twisted stacked crosses.[61] (b) Tapered gold helices.[63] (c) Gold nanoparticles bonded on DNA origami formed left- and right-handed helix structures.[64]

However, both strategies cannot generate highly-customized 3D plasmon nanostructures cost-effectively. Lately, a newly pioneered water-based bottom-up approach was reported; the method introduced the application of cysteine and cysteine-based peptides, therefore various 3D intrinsic right- and left-handed chiral as well as achiral NPs were shown to be synthesized.[68] To synthesis these kinds of chiral Au NPs, a seed-mediated synthesis method was used, and during the colloidal growth procedure amnio acids or peptides act as chiral shape modifiers to guide the formation of chiral morphology. Since then, based on the new synthesis method, some other chi-

ral Au NPs have been reported,[69-71] and the single-step synthesis approach has been improved to the multi-chirality-evolution step to achieve chiral Au NPs with a higher chiroptical response.[72] The geometry of chiral Au NPs can be adjusted by the synthesis conditions including the amount and morphology of the seed, the introduction of different chiral molecules, as well as injection time of chiral ligand. Figure 2.2 depicts several chiral Au NP growth pathways under different synthesis parameters. The flexibility of fabricating those chiral Au NPs will be beneficial in designing varies chiral plasmonic nanostructures for chirality sensing, 3D chiral imaging, microstructure analysis, etc.

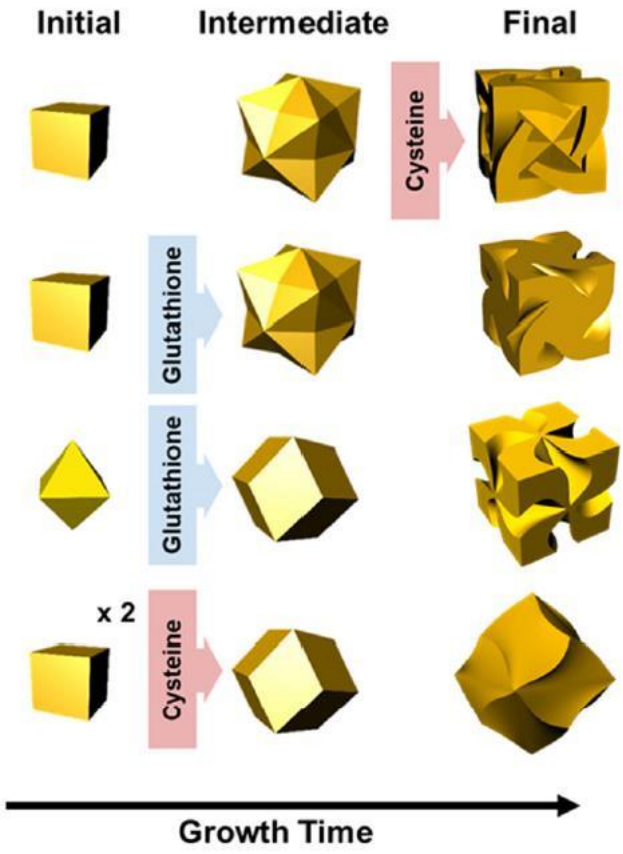

Figure 2.2 Schematic of geometric evolution of different gold nanohelicoids.[69]

2.2 Chemical synthesis of gold nanohelicoids

Chemicals

Tetrachloroauric (iii) trihydrate ($HAuCl_4$), Hexadecyltrimethylammonium bromide (CTAB), sodium borohydride ($NaBH_4$), ascorbic acid (AA), and L-/D-Cysteine (L-/D-Cys) were purchased from Aladdin and all chemicals were used without purification. Deionized water (DI) was used for all the experiments.

Synthesis of Gold Seeds

Small 2-nm-sized spherical gold seed nanoparticle synthesis was achieved by adding 0.25 mL 10 mM $HAuCl_4$ to 7.5 mL 100 mM CTAB, and then rapidly injecting 0.8 mL 10 mM $NaBH_4$ into the mix solution. Immediately after the injection, the mixture became dark brown. The resulting mixture was aged at 28 ℃ for 3 h.[69]

Synthesis of Cubic Seed Gold Nanoparticles

Using a growth solution containing 8 mL DI water, 0.2 mL $HAuCl_4$ (10 mM), 1.6 mL CTAB (100 mM), and 0.95 ml 50 mM AA, and by adding 55 μL 1/10 diluted spherical gold seeds to the growth solution, large cubic seed gold nanoparticles were prepared. After 15 min, the final solution turned pink, and which is then centrifuged twice and redispersed in the 1 mM CTAB solution.[73]

Synthesis of Chiral Gold Nanoparticles

A growth solution to synthesize GNHs was readied by mixing 3.95 mL DI water, 0.8 mL 100 mM CTAB, 0.475 mL 100 mM AA, 0.1 mL 10 mM $HAuCl_4$, and 5 μL 100 μM L/D-Cys. The synthesis of GNHs was performed by adding 100 μL of pre-

made cubic nanoparticles to the growth solution, and allowing the mixture to process for 1h. After two centrifugations, unreacted chemicals were removed, and the chiral nanoparticles were placed in a 1 mM CTAB solution for following measurement.[68, 69]

2.3 Structural characterization gold nanohelicoids

Scanning Electron Microscopy (SEM)

SEM images were taken by Field Emission Scanning Electron Microscope (Tescan MAIA3), and were used to characterize the chiral geometric morphologies of gold nanohelicoid. 100 μL gold nanohelicoids were centrifuged twice to remove the attached CATB, and the resultant solution was redispersed in 50 μL DI water. Then they were drop-cast on an ITO glass for SEM imaging. Since ITO is conductive, using ITO glass could avoid gold deposition, which is better to observe the chiral morphology of gold nanohelicoids. The left panels of Figure 2.3 show the SEM image of left- and right-handed gold nanohelicoid (L-/R-GNH) structures and their corresponding 3D constructs (in the illustrations). Figure 2.3c and d depict the zoomed in SEM images of L-/R-GNH configurations, the white dashed lines illustrate the handedness of the two constructs, where structural chirality can be seen at both the surfaces and corners of the GNHs.

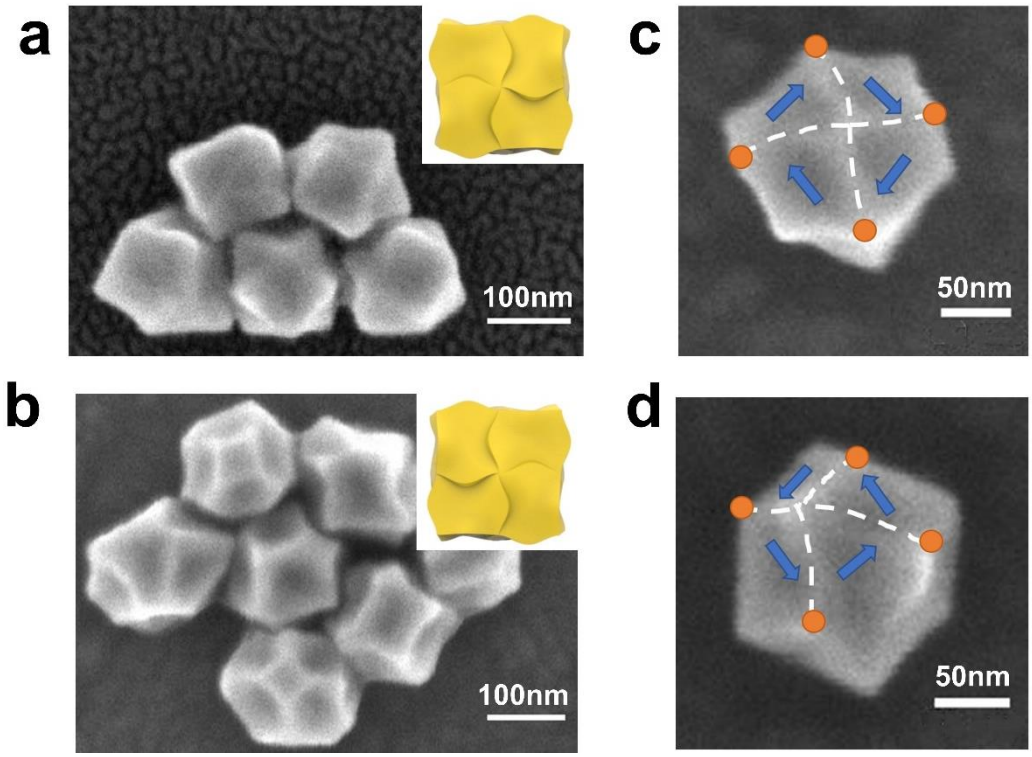

Figure 2.3 Grouping of scanning electron microscopy (SEM) images of (a) left- and (b) right-handed gold nanohelicoids (GNH) with sizes ranging from 120-150 nm. Insets are the corresponding three-dimensional (3D) chiral constructs. Zoomed in SEM images of (c) left- and (b) right-handed GNH. Blue arrows and white dashed lines (linking the orange vertices) assert the helicity of the GNH enantiomers.

Circular Dichroism Spectroscopy (CD)

CD spectroscopy reflects measured CD as a function of wavelength. L-/R-GNH solutions with appropriate concentrations were loaded in a 1-cm-thick quartz cell for extinction and CD spectra measurement by JASCO CD spectrometer (J-100). Through calculating the extinction and CD spectra, the *g*-factor spectra can be converted directly from the CD spectrometer.

As shown in Figure 2.4a, the CD spectrometer measures the different intensities of LCP and RCP light beams after passing through the quartz cuvette. Figure 2.4b and

c depict the extinction and CD spectrums of the L-/R- GNHs in an aqueous solution of CTAB, both having good concordance in relation to both the simulated calculations (dashed lines) and experimental results (solid lines). As can been seen from Figure 2.4b that the extinction cross section spectrum of the L-GNHs is mainly monopolized by a broadband electric dipole resonance crest from about 500 to 800 nm. It is interesting to note that, the CD spectrums for both L-GNHs and R-GNHs (Figure 2.4c) flip at about 610 nm (close to the experimental extinction peak at about 650 nm) and exhibit mirror-symmetric bisignate resonances with opposite helicity. In the meanwhile, the degree of the innate geometric chirality for the GNHs can be evaluated by a CD *g*-factor, defined as $g_{\mathrm{CD}} = 2\frac{A^{+}-A^{-}}{A^{+}+A^{-}}$, where A stand for the circularly polarized extinction and the superscripts "+" and "-" are denoted as the helicity of circular polarization excitation. The results in Figure 2.4d reveal that the maximum CD *g*-factors of the L-GNHs and R-GNHs are about -0.012 and 0.008, respectively, which are comparable to the values of ±0.01 in the reported work.[69]

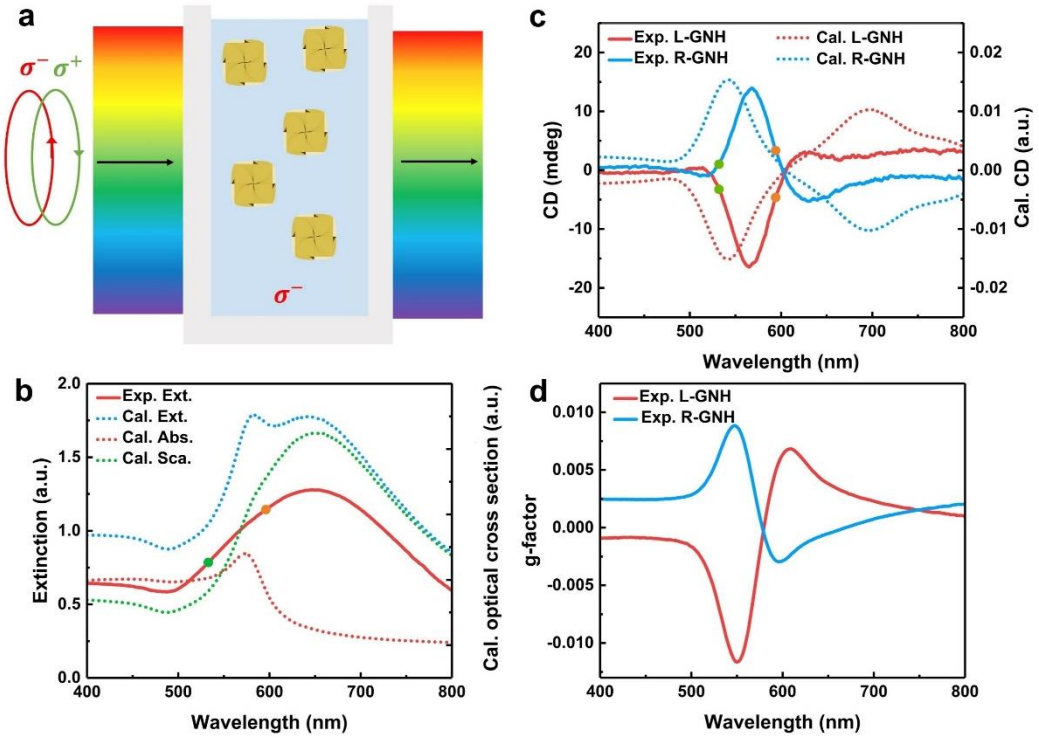

Figure 2.4 (a) Schematics of the CD and extinction measurements of the GNHs solution. (b) Experimental extinction (solid line) and calculated extinction, scattering and absorption (dashed blue, green, and red lines, respectively) spectrums of the left-handed GNH in CTAB aqueous solution. (c) Experimental (solid lines) and calculated (dashed lines) CD spectrums of the left-handed GNH (L-GNH) and right-handed (R-GNH). In the calculated spectrums, the crests and trough at around 700 nm may be attributed to the difference between the real morphology and the simplified ideal model. (d) Experimental *g*-factor spectrums of GNHs with different handedness.

Electromagnetic Simulation

Considering Finite-difference Time-domain (FDTD) could produce a full spectrum with a single run and enable the observation of the electromagnetic field distribution at any time of the simulation. The FDTD method was applied to study the electric and magnetic characters of the GNH. The monitored cross section of a simplified 3D GNH model used for FDTD simulation is described in Figure 2.5. The circularly polarized light is vertically illuminated on the model surface.

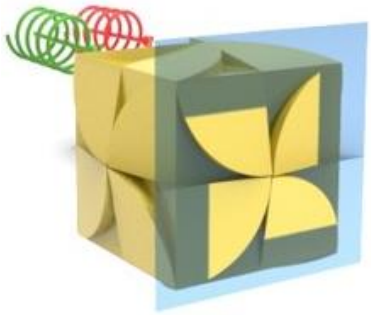

Figure 2.5 The simplified 3D model and monitored cross section of the gold nanohelicoid. Blue shadowed area indicates the cross-section shape of the monitor.

Figure 2.6a and b depict the simulated electric and magnetic near-field distributions in the middle-plane cross section (dashed 'pinwheel' pattern) of the chiral nanostructure. Figure 2.6c and d render the calculated electric and magnetic near-field intensity difference for the R-GNH structure under RCP and LCP excitation, which manifests that the chiral optical response of the GNH is caused by its intrinsic geometric chirality. Herein, we only show one right-handed structure simulation due to the sole difference of GNH enantiomer being helicity.

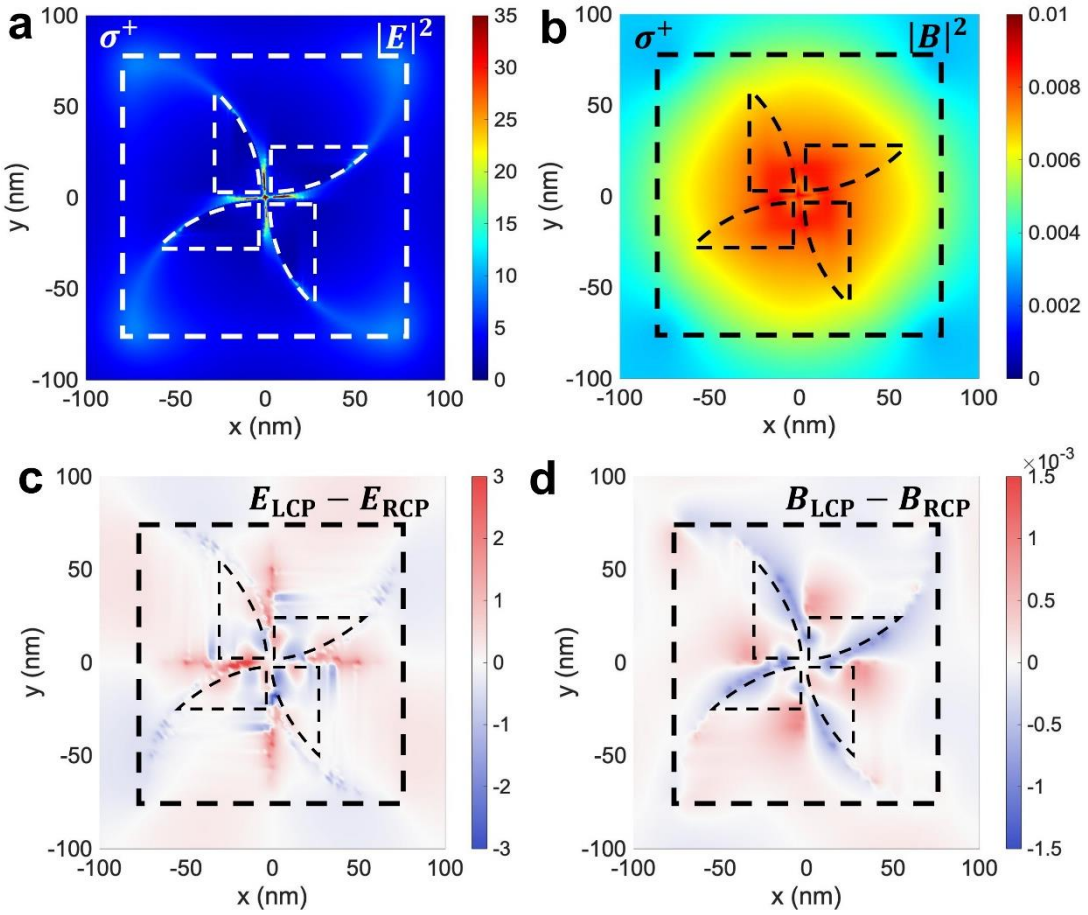

Figure 2.6 (a) Simulated electric near-field intensity distribution for an R-GNH under 593.5 nm LCP excitation. (b) Simulated magnetic near-field intensity distribution for an R-GNH under 593.5 nm LCP excitation. (c) The intensity difference of electric field in an R-GNH under circular polarization excitation. (d) The intensity difference of magnetic field in an R-GNH under circular polarization excitation.

Chapter 3 Chiral photoluminescence from gold nanohelicoids

3.1 Introduction

3.1.1 Single-photon photoluminescence of gold nanoparticles

Similar to semiconductors or fluorophores, interband transition in metal causes single-photon absorption induced luminescence, i.e., PL. Mooradian, in 1969, initially depicted the idea of PL of gold in both experiment and theory.[74] As shown in Figure 3.1, the emission of bulk gold is attributed to the radiative process that occurs when the combination of electrons exist in the *sp* band, while holes remain in the *d* band. However, the emission quantum efficiency is only approximately around an order of 10^{-10}. In 1986, Boyd *et al*. observed enhanced PL from roughed metal films with ~10^{-6} quantum efficiency. They reported a widely adopted electric field enhancement theory, which suggests that the improvement of both excitation and emission efficiency is caused by the enhanced local electric field at corresponding wavelengths.[75]

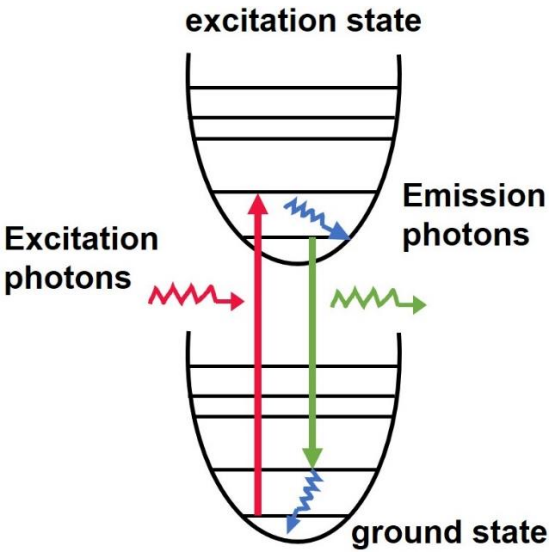

Figure 3.1 Illustration of the single-photon photoluminescence (PL).

Subsequently, a series of observations of PL enhancement in metallic nanostructures, in particular, gold nanostructures, have been reported. Hu *et al*. reported the PL and scattering spectra of different individual gold nanodisks with different diameters, nanotriangle, and nanorod.[76] As shown in Figure 3.2a, the PL peak position of a single gold nanodisk is modulated by the plasmon resonances, which are strongly dependent on the shape and size of single Au nanostructures. Later on, scientists expanded the PL study on colloidal Au NPs. Zhang *et al*. experimentally revealed that the PL properties of a single gold nanorod depend on the polarization of excitation light (Figure 3.2b).[77] Different conversion efficiencies of interband transition and plasmon emission lead to the polarization-dependent PL quantum yield (QY). In addition, stronger mode coupling results in higher plasmon emission efficiency, which means localized surface plasmon (LSP) mode coupling attributes to the plasmon emission efficiency. Rao *et al*. compared the PL properties of Au nanobipyramids and Au nanorods under

different excitation and detection polarization (Figure 3.2c).[78] For gold nanobipyramids and gold nanorods with similar surface plasmon resonance ranges, the PL QY of a single gold nanobipyramid is twofold higher. This difference is because gold nanobipyramids have stronger field intensities integrated over their volume.

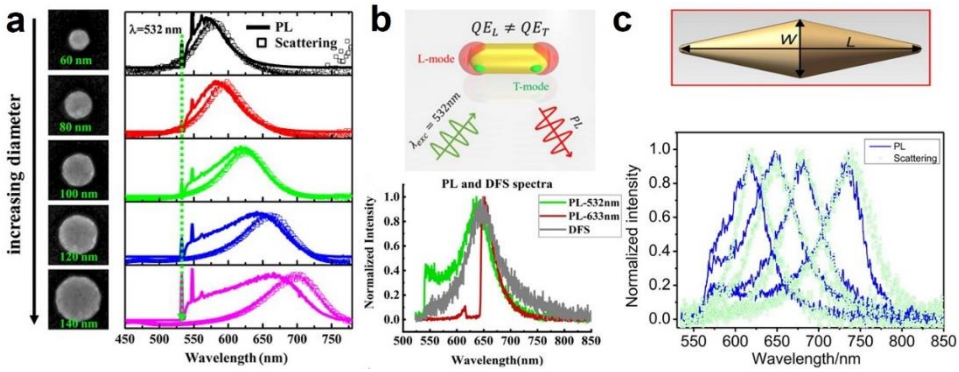

Figure 3.2 (a) PL and scattering spectrums of lithographically made gold nanodisks with different diameters.[76] (b) PL spectrums of a single gold nanorod under 532 nm and 633 nm excitation.[77] (c) PL and scattering spectrum of a single gold nanobipyramid.[78]

The e-h pair exhibited PL in gold is correlated with the enhanced local electric fields at the plasmon resonance frequency; the level of PL enhancement by Au NPs is limited. Recently, scientists found that a plasmonic system formed by metallic nanoparticles deposited on metallic or highly polarizable substrates[79] could generate strong localized resonances near the gap between the particle and the substrate, which can be used to significantly enhance the PL.[80] Lumdee *et al*. studied the gap-mode-enhanced PL of the single Au NP on an Al_2O_3-coated gold film (Figure 3.3a).[81] Based on this system, it was noted that under 633 nm excitation, the largest PL enhancement factor that could be observed was 28000. Li *et al*. reported the Au NP dimer on a thin gold film could have about 200 times the PL intensity enhancement and about 4.6 times the

emission line-width narrowing compared to Au NP dimer on a glass substrate (Figure 3.3b).[82]

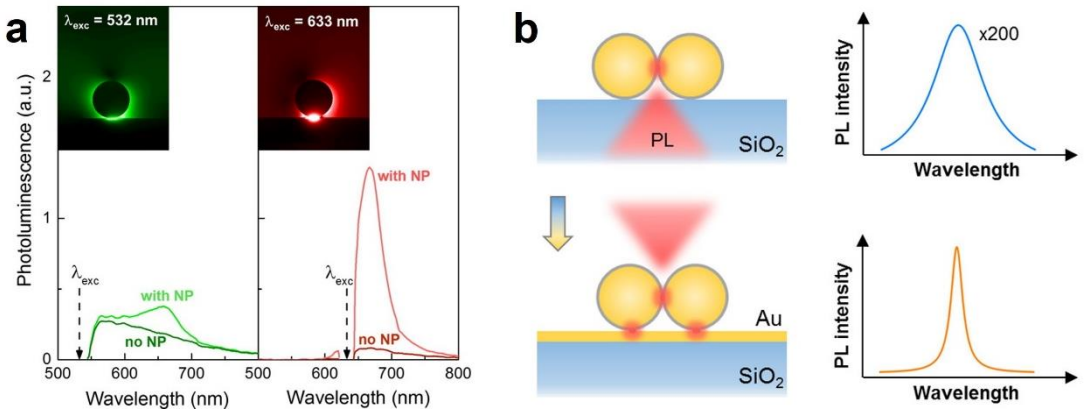

Figure 3.3 (a) PL spectrums of Al_2O_3 coated gold film with and without single Au NP under 532 nm and 633 nm excitation.[81] (b) PL excitation illustration and spectrums of Au NP dimer on a glass substrate and a thin gold film.[82]

However, all above discussed PL studies or polarization involved PL research on a single Au NP or metal-substrate-mediated Au NP hybridization system are limited in achiral regime. Widening the scope of PL polarization research, development, and control into the field of chiral research has many important potential applications for optical data storage, biosensing, bioimaging, etc.

3.1.2 Circularly polarized luminescence

In chiral plasmonic-related PL studies, circularly polarized luminescence (CPL) is a well-known and commonly used technique to study chiral PL. CPL reflects the difference in the RCP and LCP emissions of a chiral emitter (Figure 3.4), which discloses the excited state information and is associated with the magnetic dipole mo-

ment involved in the optical transition.[83]

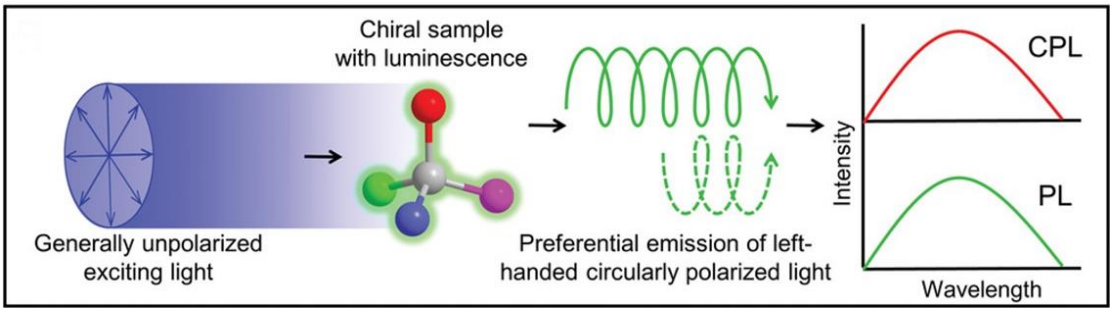

Figure 3.4 Schematic illustration of circularly polarized luminescence (CPL).[84]

CPL-active materials have found potential applications in 3D displays, [85] chiroptical materials,[86] smart memory[87] materials, and optical devices.[88, 89] Generally, to generate CPL-activity, the utilization of luminescent organic or inorganic materials is required. Both chiral and achiral chromophores can be endowed with CPL activity through self-assembly. As shown in Figure 3.5, through self-assembly, co-assembly, or doping into liquid crystals, not only achiral but also chiral building blocks could assemble into chiral nanostructures, emitting CPL.

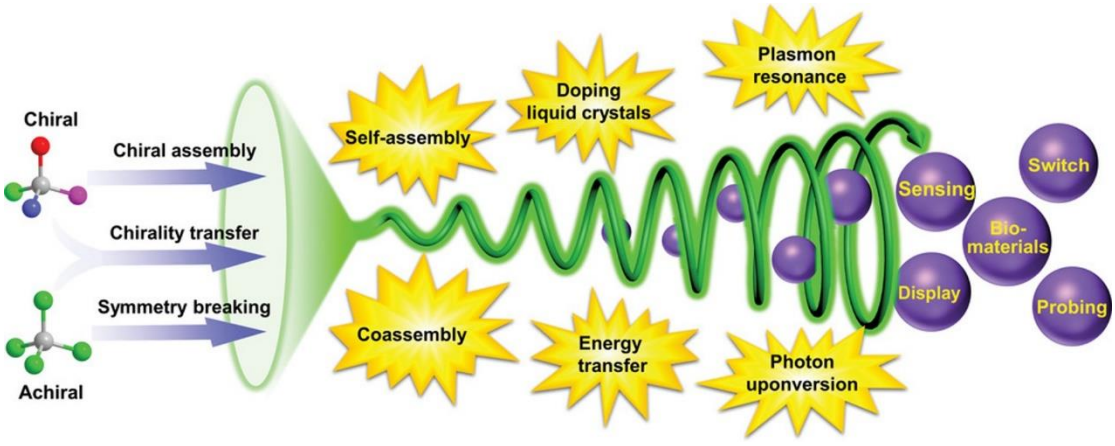

Figure 3.5 Schematic diagram of the nanoassemblies-participated CPL generation, amplification, and applications.[84]

So far, three typical methods to make CPL-active material are shown in Figure 3.6: (i) chiral luminescent assemble into chiral morphology; (ii) chiral molecules combine with achiral luminophores; (iii) chiral assembly of achiral luminescent.[84] In general, these approaches require tedious and long synthesis processes, thus the further development of fabricating inorganic CPL-active materials is impeded.

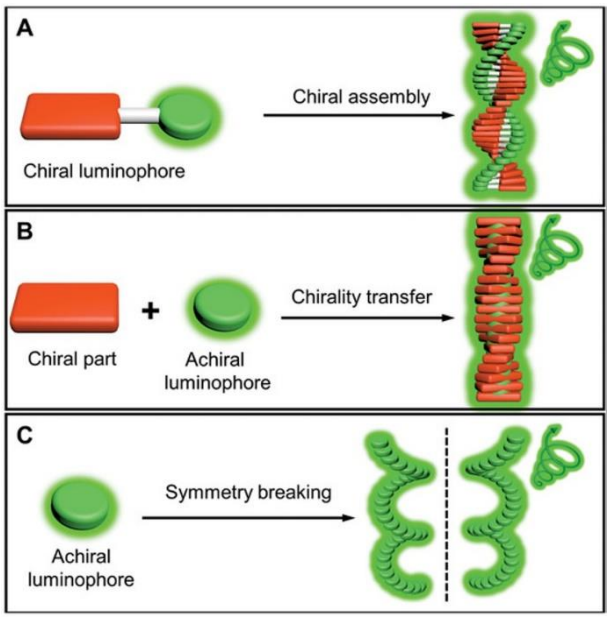

Figure 3.6 Schematic illustration of three approaches to realize CPL in nanoassemblies.[84]

Normally, to eliminate the polarized light impact originating from the coupling effect between the nonideal properties of the instrument and macroscopic anisotropies, the excitation light source used for CPL measurement is linearly polarized.[90-92] Under this condition, the CPL cannot reflect the relationships between excitation, emission circular polarization, and the helicity of chiral emitters; a condition which is causing chirality-involved PL procedure to be elusive even until now.

3.2 Experimental methodology

3.2.1 Sample preparation

A 50 μL solution of synthesized GNH was centrifuged two times, and then the centrifuged GNHs were redispersed into 100 μL DI water. A single drop of the diluted solution (about 20 μL) was casted onto a pre-cleaned ITO glass. After drying in the air for about 3min, the solution on the substrate was blown off by using a rubber suction bulb. The majority of GNH clusters were scattered into monomers with large particle-particle distance, thus, enabling the measurement of single nanoparticles.

3.2.2 Single-particle scattering and photoluminescence spectroscopy

A fluorescence microscope equipped with a home-built polarization-resolved dark-field illumination module was applied to perform the chiral scatterometries and PL spectrums of each single GNH. A linearly polarized monochromatic continuous wave (CW) laser (CNI Co., Ltd.) with wavelength of 532/593.5 nm was chose as the excitation source and a quarter-half waveplate combination was applied to produce circularly polarized light (Appendices (A)). A three-axis piezo-controlled stage was then used to move each GNH to the middle of the laser target area. The laser power was adjusted to about 80 μW to generate the PL signal. The confocal 100× micro-scope (NA 0.8, LMPlan, Olympus) focused and collected the PL or scattering signal from the sample. The signal integration time is 20s. Every signal acquisition was done

three times. The polarization-dependent effect of the beam splitter (BS, BSW10R, Thorlabs, Inc.) inside the microscope was canceled out by a polarization calibration. Using two 600 nm long pass filters (LPF, FEL0600, Thorlabs, Inc.) the 532 or 593.5 nm excitation was obstructed, while using an imaging spectrometer (Acton Sp2300, Princeton Instruments integrated with PIXIS 400 CCD camera), the signal was recorded.

As sketched in Figure 3.7, a CW laser beam traverses through a short pass filter (SPF, FES0600, Thorlabs, Inc.), a half and a quarter waveplate, generating circularly polarized light, which is then concentrated by an objective lens to excite single GNHs. The use of SPF is to eliminate the side band effect of the 593.5 nm laser. Since the 593.5 nm laser is a custom product, it has a side band wavelength at around 670 nm. The use of SPF could effectively block the side band wavelength ensuring the excited PL is generated by the 593.5 nm. The half waveplate in the optical path is to eliminate the polarization effect of the beam splitter in the excitation path. Collection of the PL emission signal is performed using the same objective; then for spectral analysis, the collected signal is sent to a spectrometer; and for image capturing, a CCD camera is used. A polarizer and a quarter waveplate are set in front of the spectrometer to check the polarization state of the PL signal. When equipped the same microscope system with a white light source, the chiral scattering spectra of the single GNH can also be measured.

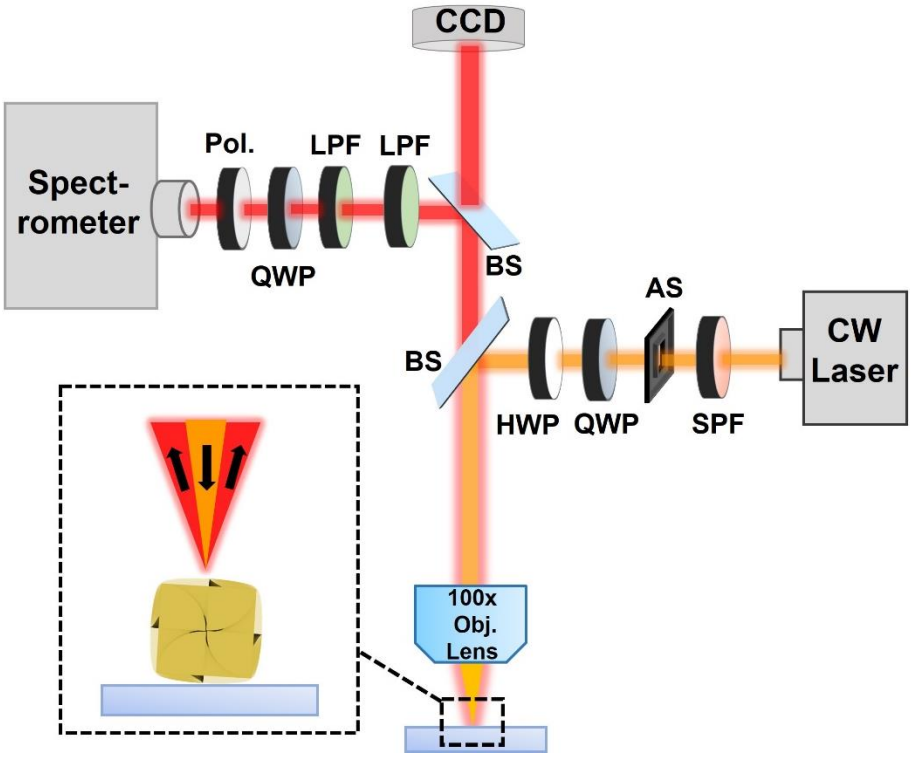

Figure 3.7 The illustration of single-particle experiment setup for polarization-resolved dark-field scattering and PL measurements. HWP: Half waveplate, QWP: Quarter waveplate, BS: Beam splitter, SPF: 600 nm short pass filter, LPF: 600 nm long pass filter, Pol.: Polarizer, AS: Aperture slot.

3.3 Chiral photoluminescence in single gold nanohelicoids

3.3.1 Selective excitation of polarization-steered chiral photoluminescence

Before measuring the PL signal, the chiral scatterometry spectra of single GNH were measured first. An obvious difference in the circularly polarized scattering intensities of the L-/R-GNH structure can be seen in Figure 3.8, manifesting a sufficiently strong chiral optical activity for studying chiral PL at the single-particle level.

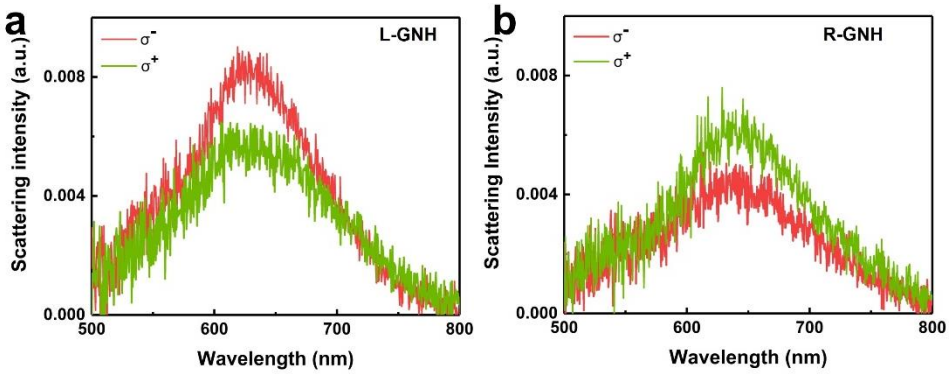

Figure 3.8 Scattering spectra of a (a) left-handed GNH (L-GNH) and a (b) right-handed GNH (R-GNH) structure (used for the 593.5 nm laser illumination) under white right circularly polarized (RCP i.e., σ^-, red) and left circularly polarized light (LCP i.e., σ^+, green) light illumination.

Using the above experimental system, PL spectrums of the GNHs generated by circularly polarized light to probe the chiral excitation and emission characteristics of GNHs were measured. The LCP and RCP excitation wavelength was set at 593.5 nm (close to the extinction main peak of the GNH) to achieve plasmon-enhanced PL excitation. As described in Figure 3.9a, the L-GNH generates a smaller PL signal in response to the LCP excitation than to the RCP one, while the PL signal of the right-handed displays a reversed intensity contrast (Figure 3.9b). These results clearly demonstrate that the GNHs with opposite handedness show a reversed absorptivity response to the RCP and LCP light. The dissymmetry factor of PL intensity is calculated by $g_{\mathrm{PL}} = 2\frac{I^+ - I^-}{I^+ + I^-}$, where I are denoted as the emission PL intensities and the superscripts "+" and "-" represent the left- and right-helicity of excitation polarization. Correspondingly, the g_{PL} for R- and L-GNH are ±0.12, respectively. In addition, it should be also noticed that the PL spectrums of GNH enantiomers show similar resonance and intensity characters with their scattering spectrums (Figure 3.8), all display-

ing a broad peak at around 640 nm, and similar intensity contrast tendency with regards to excitation light with opposite polarization helicity. Such PL-scattering, discussed later, is due to the PL signals of Au NPs generally being dominated by plasmon-modulated and enhanced radiative recombination. The intensity differences of the polarization-steered PL towards RCP and LCP excitations come from the structural chirality of the GNH. Verification of these differences was performed through the process of checking the scattering and PL spectrums of a 100 nm achiral gold nanocube. Figure 3.9c and d show that there is no difference under the LCP and RCP excitation with regard to scattering or PL intensity.

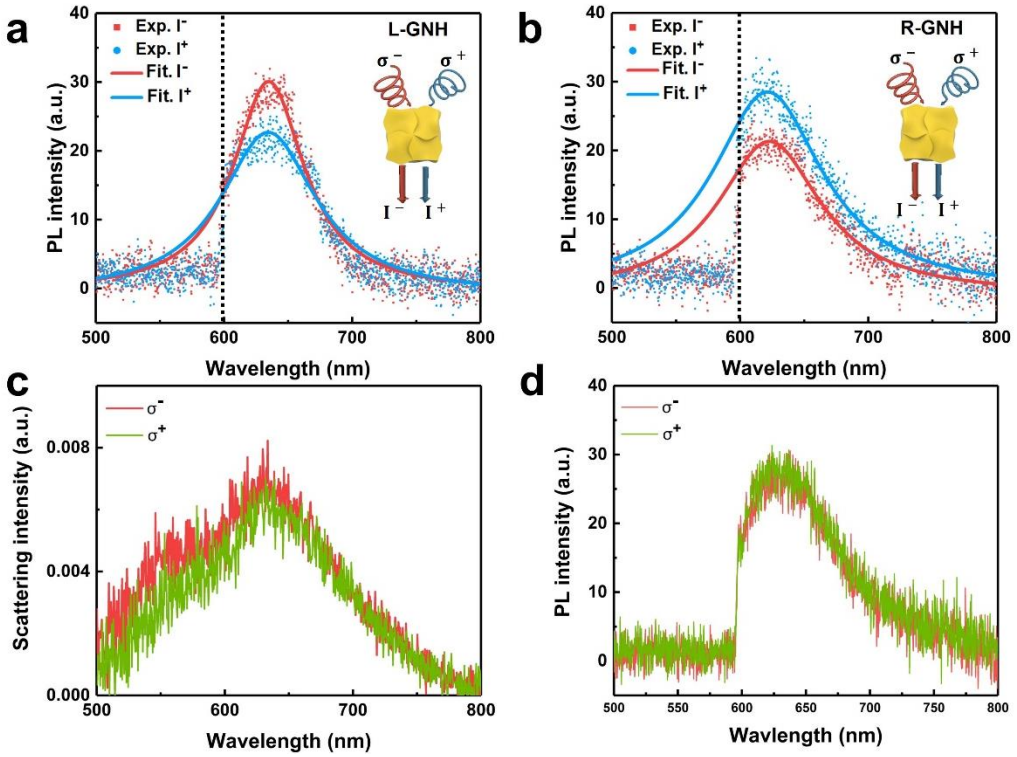

Figure 3.9 (a, b) PL spectrum of a single (a) L-GNH and (b) an R-GNH under RCP (σ^-, red) and LCP (σ^+, blue) laser excitation at 593.5 nm. The PL intensity has a cliff at 600 nm (black dashed line) is attributed to the cut-off response of the long-pass filter applied in the optical path. The solid lines show the Lorentzian fits of the raw data. (c) Scattering spectrums of an achiral nanocube with RCP (red) and LCP (green) light excitation. (d) PL spectrums of an achiral nanocube under

RCP (red) and LCP (green) laser excitation at 593.5 nm.

In order to understand the chiral features of the measured PL signals for both GNHs in Figure 3.9a and b, decomposition of the PL signals into the LCP and RCP elements was performed by combining a quarter-waveplate and a polarizer. The decomposition results are summarized in Figure 3.10. As can be seen, the dominant chiral element of the PL signal of each nanoparticle is identical to that of the excitation light, i.e., LCP (RCP) illumination produces LCP (RCP) element dominated PL irrespective of the geometric helicity of the GNH. In order to evaluate the PL helicity quantitatively, we calculated the chiral degree of polarization of the measured polarization-resolved PL, i.e., so-called polarization-resolved PL *g*-factor, defined as $g_{\mathrm{RPL}} = 2\frac{I_+ - I_-}{I_+ + I_-}$, where I are denoted as emission polarization-resolved PL intensities and the subscripts "+" and "-" refer to the helicity of emission polarization. Based on this definition, an absolute g_{RPL} value of 0.73 was found for both the RCP and LCP excitations for an achiral Au nanocube particle with similar size to GNHs, implying an excitation-polarization-independent g_{RPL} (Figure 3.10a and b). In the meanwhile, we observe from Figure 3.10c that the absolute value of g_{RPL} for the L-GNH under the RCP illumination is about 0.55, which is much smaller than that for the R-GNH under the RCP illumination (1.03 for Figure 3.10d). However, the results for the two structures under the LCP excitation reverses (1.04 for Figure 3.10e and 0.62 for Figure 3.10f). These distinctive results confirm a crucial role of geometric chirality in the chiral degrees of emission polarization. In comparison with the achiral nanocube, the

absolute g_{RPL} value of the GNHs with co-/anti-chiral excitation is enhanced/suppressed with a normalized enhancement factor of 1.41 (Figure 3.10d) and 0.75 (Figure 3.10c), supporting a polarization-steered effect.

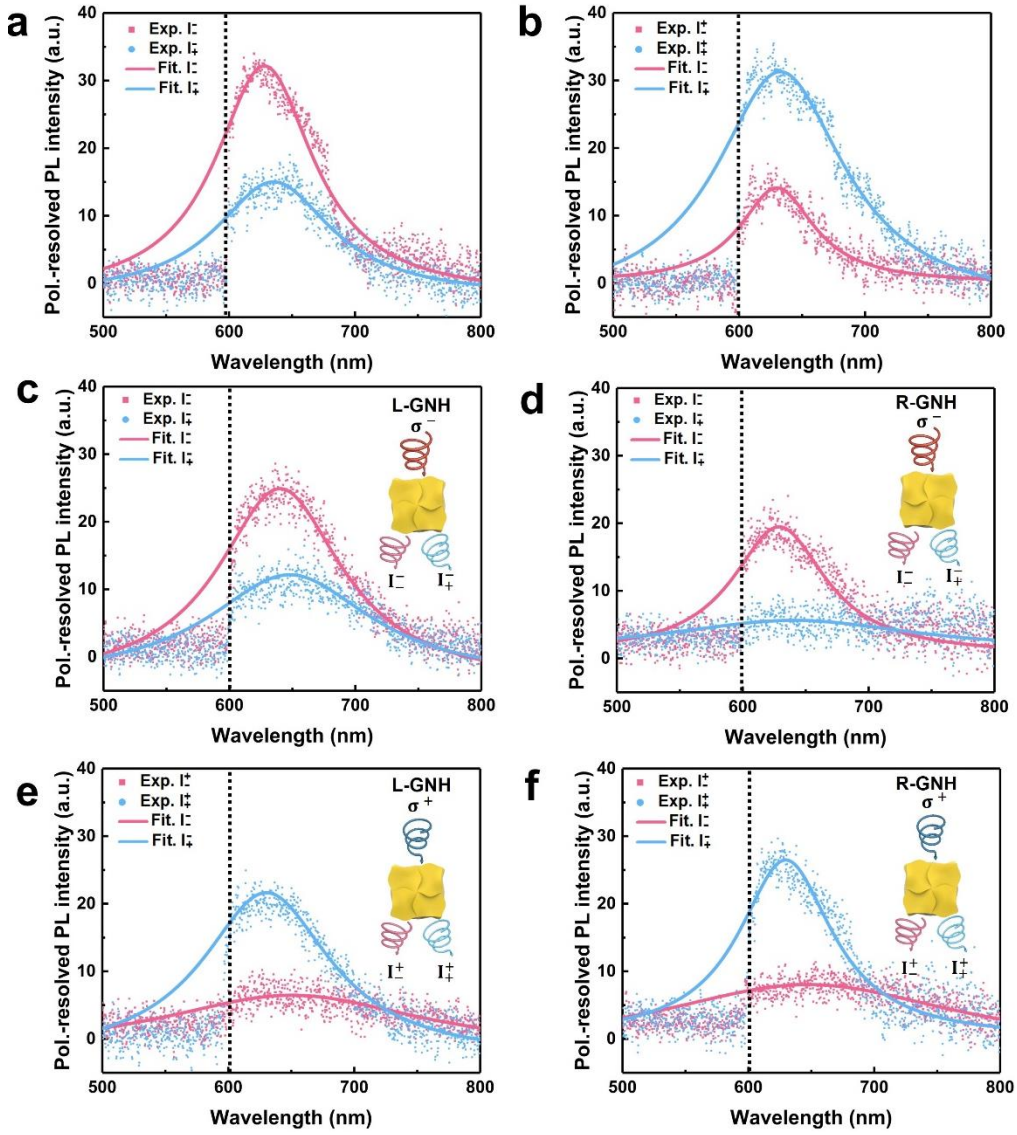

Figure 3.10 (a, b) Emission polarization-resolved PL spectrum for the achiral nanocube under the RCP (a) and LCP (b) laser excitation at 593.5 nm. (c-f) Emission polarization-resolved PL spectrum for the L-GNH (c, e) and the R-GNH (d, f) under the RCP (c, d) and LCP (e, f) laser excitation at 593.5 nm. The solid lines show the Lorentzian fits of the raw data.

To broaden understanding of the chiral activities, the aforementioned measure-

ments for the GNH enantiomers were also conducted at an excitation wavelength of 532 nm. In comparison with the excitation at 593.5 nm, the chiral PL and polarization-resolved chiral PL intensities of GNH under 532 nm excitation are much lower (Figure 3.11). This can be resulted from the larger absorptivity of GNH at 593.5 nm (highlighted with an orange point, Figure 2.4b) with respect to that at 532 nm (highlighted with a green point), thus allowing more photons at 593.5 nm to participate in the whole PL process. Besides, the g_{PL} at 532 nm is also lower than that at 593.5 nm, which is in consistence with the results in Figure 2.4c, that the GNH excited at 593.5 nm (marked with an orange point) shows larger absolute CD value than at 532 nm (marked with a green point). These observations ulteriorly suggest that the 593.5 nm light is more efficient for enhancement of the chiral PL response. Finally, the polarization-resolved chiral PL under 532 nm excitation presented in Figure 3.11c-f shows a similar scenario of the polarization-steered PL as that of the 593.5 nm excitation.

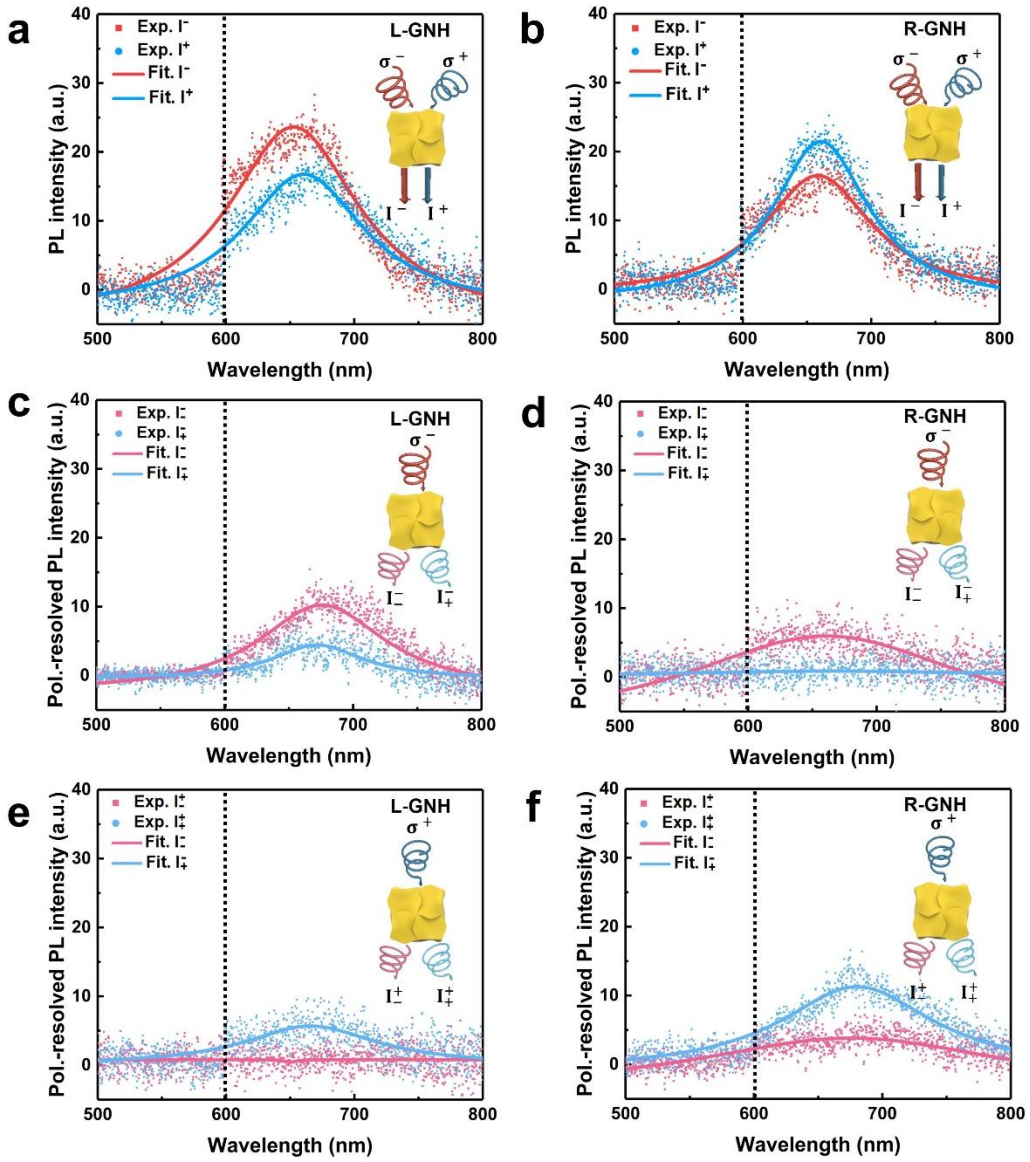

Figure 3.11 (a) PL spectrum of a single L-GNH under RCP (σ^-, red) and LCP (σ^+, blue) laser excitation at 532 nm. (b) Similar results as (a) for a single R-GNH structure. (c-f) Emission polarization-resolved PL spectrum for the L-GNH (c, e) and R-GNH (d, f) under the RCP (c, d) and LCP (e, f) laser excitation at 532 nm. The solid lines show the Lorentzian fits of the raw data.

It should be noticed that, compared with 593.5 nm results, the PL main peak under 532 nm has a little red shift. This is due to the GNH under 593.5 nm not being the same one as 532 nm. The scattering spectrums of GNHs used in 532 nm measurements are shown in Figure 3.12 whose main peaks also appear at a longer wavelength.

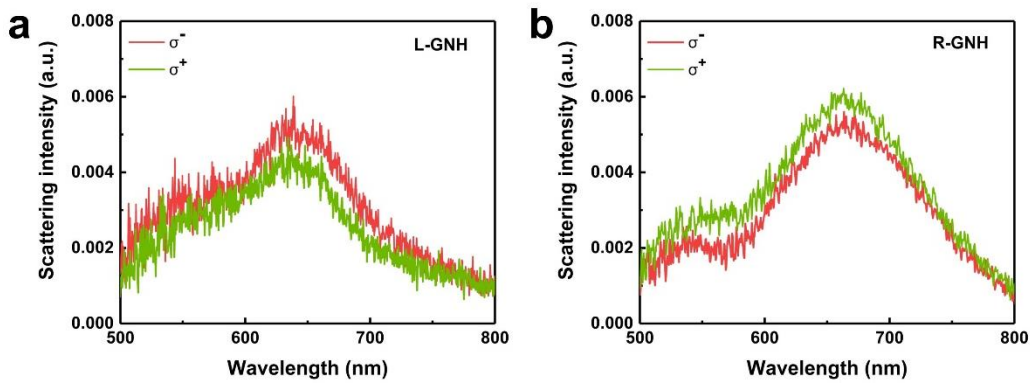

Figure 3.12 Scattering spectra of (a) a L-GNH and (b) an R-GNH used for the laser excitation conditions in Figure 3.11 (a) and (b), measured under white RCP (σ^-, red) and LCP (σ^+, green) light excitation.

3.3.2 A phenomenological model for chiral photoluminescence

In order to disclose the mechanism behind the aforementioned experimental observations, the energy band structure of gold around the X point in the first Brillouin zone is shown in Figure 3.13**.** The Figure 3.13 shows the chiral PL process:

(1) Excitation. After absorbing the incident excitation photons, electrons near the top of the *d*-band are excited into the upper *sp*-band, with holes left at the top of the *d*-band.[74] The absorption probability $Y_{abs}(\omega_{ex})$ is used to describe the probability of a single-photon absorbed by materials at the excitation frequency ω_{ex}. The pumping rate $P_{\pm}$ of the single-photon PL process is determined by the local electric field intensity $I(\omega_{ex})$. In our case, the single GNHs have significantly different optical absorptivity when excited with circularly polarized light with different handedness. Take the L-GNH as an instance. In accordance with its negative CD value at about 593.5 nm

(Figure 2.4c), it prefers to absorb RCP light, meaning more electrons can be excited into the upper *sp*-band (Figure 3.13).

(2) Relaxation. Subsequent to the upward electron excitation, the energetic electrons experience a nonradiative thermalization process, which gives rise to a broad distribution of electron energies. The population of the excited electrons relaxing to a specific emission state with angular frequency ω_{em} is determined by the relaxation probability $Y_r(\omega_{em})$.

(3) Emission. At last, the excited electrons either directly recombine with the *d*-band holes, and simultaneously emit photons, or excite the localized surface plasmon of metal nanostructures. The LSP typically decays in both the nonradiative (via ohmic loss) and radiative (far-field radiation) ways. For nanostructured noble metals, most of the PL emission arises from the radiative plasmon damping, while a small percentage is from the direct recombination of the energetic electrons with the holes left in the *d*-band.[76, 82, 93, 94] The photon emission probability is described by $Y_{em}(\omega_{em})$, and the emission oscillation direction is reconstructed by the excitation polarization state and affected by the chiral morphology of the GNH. [95-97]

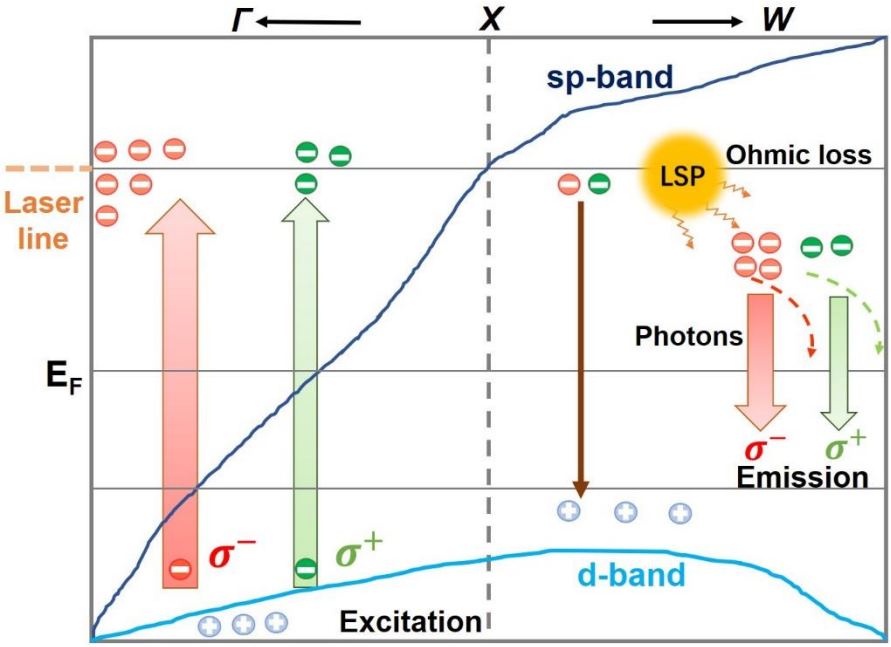

Figure 3.13 Schematic graph of the chiral PL process of the chiral nanostructures. Here take the L-GNH under 593.5 nm excitation as an example. The RCP light (red thick upward arrow) generates more *d*-band electrons of gold to the *sp*-band based on its larger absorptivity compared to that of the LCP light (green thinner upward arrow). The majority of the energetic electrons transfer to the localized surface plasmon (LSP) band while a minority of them directly recombine with the holes (brown thin downward arrow). Following this, the excited LSPs undergo either radiative decay to generate PL emission (red and green dashed arrows) or non-radiative decay leading to Ohmic loss. The PL emission can be modulated by the geometric chirality of the GNH.

According to the above discussions, we can quantitively evaluate the single-photon absorption induced luminescence of gold by a phenomenological model. Specifically, the chiral PL intensity from an elementary volume dV is written as:[98]

$$I_{\mathrm{PL-d}V}(\omega_{\mathrm{ex}}) = I(\omega_{\mathrm{ex}})Y_{\mathrm{abs}}(\omega_{\mathrm{ex}})Y_{\mathrm{r}}(\omega_{\mathrm{em}})Y_{\mathrm{em}}(\omega_{\mathrm{em}}) \tag{3.1}$$

In a phenomenological way, we can simplify and modify Equation 3.1 according to the following considerations: (i) The excitation intensity $I(\omega_{\mathrm{ex}})$ at a local elementary volume is $|E_{\mathrm{loc}}(\omega_{\mathrm{ex}})|^2$; (ii) The absorption probability $Y_{\mathrm{abs}}(\omega_{\mathrm{ex}})$ and relaxation proba-

bility $Y_r(\omega_{em})$ are constants and are related to the imaginary part of the permittivity of gold; (iii) The emission probability of radiative recombination $Y_{em}(\omega_{em})$, which is proportional to the field intensity at the emission frequency $|E_{loc}(\omega_{em})|^2$,[99] and is determined by the local field density of optical states (LDOS). In the view of the above hypothesis, the relative chiral PL intensity of nanohelicoids with different helicity describes in Equation 3.1 can be written as:

$$I_{PL}^{relative}(\omega_{ex}) = \int |E_{loc}(\omega_{ex})/E_0(\omega_{ex})|^2 \cdot |E_{loc}(\omega_{em})/E_0(\omega_{em})|^2 dV \quad (3.2)$$

where E_0 is the background electric field intensity. Thus, the relative chiral PL intensity can be evaluated by the electric fields respectively at the excitation and emission frequencies, which can be obtained from numerical simulations. As depicted in Figure 3.14, the calculated (orange line) g_{PL} spectrums of L-GNH at 593.5 nm excitation and at 532 nm excitation (green line) comply well with the experimental results (black line). The results demonstrate the dissymmetry characters of chiral nanohelicoids originates from the different spatial overlapping profile of local electric enhancement field distributions under excitation and emission.

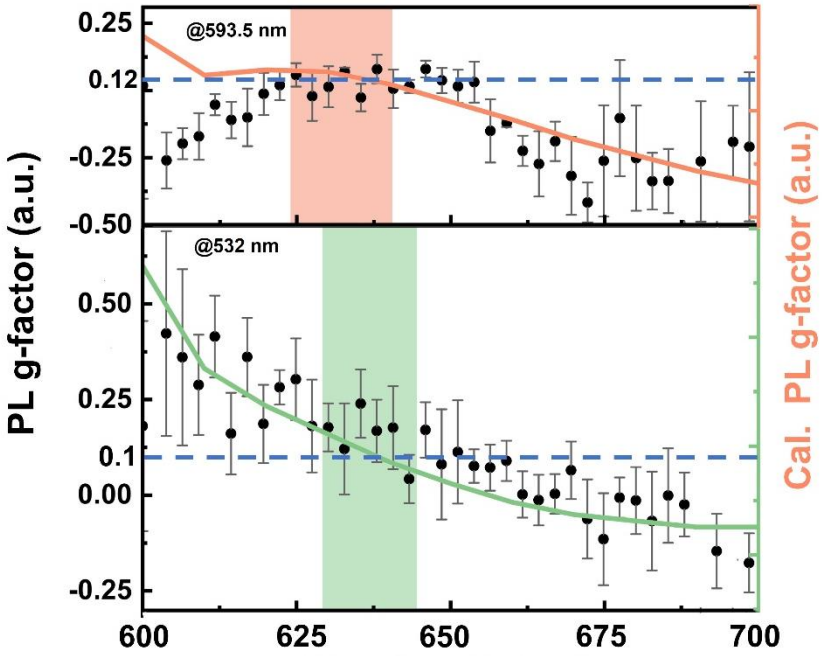

Figure 3.14 The L-GNH chiral PL *g*-factors structure under near-resonant 593.5 nm (upper panel) and off-resonant 532 nm (lower panel) illuminations. Black dots suggest experimental data while orange and green lines indicate calculation results. Blue dashed lines assert the averaged *g*-factor at the PL crests (shadowed region): 0.12 for the 593.5 nm illumination and 0.1 for the 532 nm illumination.

3.3.3 Super-chiral near-field enhancement and the chiral Purcell effect

The superchiral field and its light interactions in an optical cavity can be quantified by the local optical chirality.[45, 100, 101] The near field distribution of the optical chirality is expressed as a pseudoscalar, in term of the symmetry of time and parity:[102, 103] $C(\boldsymbol{r}) = -\frac{\varepsilon_0 \omega}{2} \mathrm{Im}[\boldsymbol{E}^*(\boldsymbol{r}) \cdot \boldsymbol{B}(\boldsymbol{r})]$, where $\boldsymbol{E}$, $\boldsymbol{B}$, ε_0, ω, are the electric field, magnetic field, permittivity of vacuum, and the angular frequency, respectively. This term can be treated as a chiral analogue to the LDOS, and manifests enhancement of chirality of the local field.[104] As depicted in Figure 3.15a and b, the simulated near-field distri-

bution of optical chirality exhibit asymmetric profile under circularly polarized light excitation. For the LCP (RCP) excitation condition, the chiral field inside the GNH (dashed 'windmill' profile) and at the corners of the GNH show positive (negative) C/C_0, where C_0 is the value of optical chirality of circularly polarized light without GNHs. A maximum optical chirality about ± 8 is gained inside the R-GNH and L-GNH hot spots, manifesting strong local chiral enhancement.

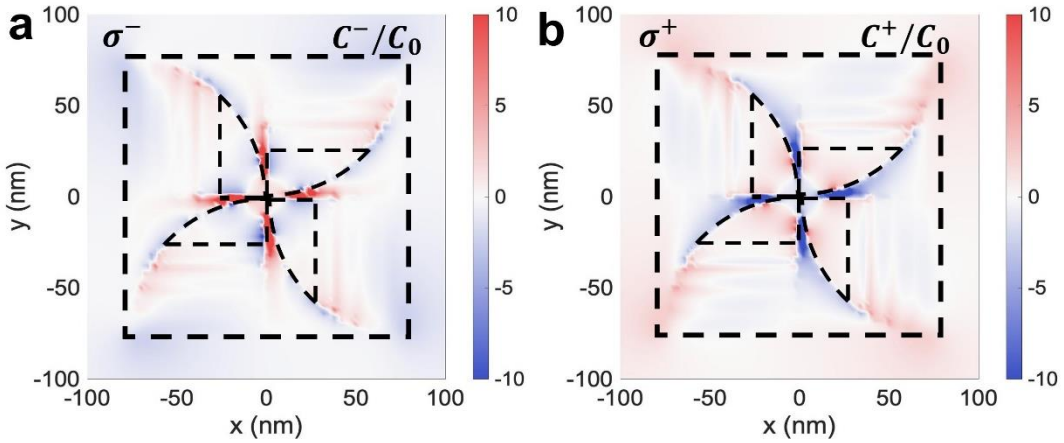

Figure 3.15 (a) Calculated near-field chirality distribution in the R-GNH under LCP 593.5 nm excitation. (b) Calculated near-field chirality distribution in the R-GNH under RCP 593.5 nm excitation.

The integration of the optical chirality inside GNHs is performed to obtain the spectral net optical chirality $\bar{C}$ (Figure 3.16a). With opposite excitation polarizations, the net optical chirality have reverse signs, which is in consistent with the flips of the dominant components depicted in Figure 3.10c-f. The net optical chirality feature at 600 nm is also in accordance with CD spectrum in Figure 2.4c as the absorption rate is closely related to C:[68] $\mathrm{CD}(\boldsymbol{r}) = -\frac{4G''}{\varepsilon_0} C(\boldsymbol{r})$, where G'' is the imaginary part of isotropic mixed electric-magnetic dipole polarizability G.[105]

Additionally, the optical chirality in the near-field accounts for the polarization feature of the far-field PL via so-called chiral Purcell effect, which ascribes to the g_{RPL} gained in experiments (Figure 3.10c-f).[106-108] The GNHs' chiral PL is modeled as uniformly distributed chiral emitters inside the GNH cavity with excitation-dependent polarization and modified spontaneous decay rate. In accordance with previous work, the modification factor of chiral molecules can be calculated via the chiral Purcell effect by:[103] $M(\boldsymbol{r}) = \frac{\Delta\Gamma(\boldsymbol{r})}{\Delta\Gamma_0} \propto -\frac{C(\boldsymbol{r})}{\omega^3 U}$. For opposite circular polarization, due to the spin-photon locking effect, i.e., $\frac{{\Gamma_0}^+(\boldsymbol{r})-{\Gamma_0}^-(\boldsymbol{r})}{{\Gamma_0}^+(\boldsymbol{r})+{\Gamma_0}^-(\boldsymbol{r})} = \pm 1$, the chiral Purcell equation can be given by:

$$M^{\pm}(\boldsymbol{r}) = \frac{\Gamma^{\pm}(\boldsymbol{r})}{\Gamma_0} \propto -\frac{C^{\pm}(\boldsymbol{r})}{\omega^3 U^{\pm}} \tag{3.3}$$

where the superscript stands for the excitation polarization state. The spontaneous decay rate is modified by the chiral Purcell equation:[102] $\frac{\Delta\Gamma(\boldsymbol{r})}{\Delta\Gamma_0} = F_C \frac{\omega_0^2}{\omega^2} \frac{\omega_0^2}{\omega_0^2+4Q^2(\omega-\omega_0)^2} \frac{C(\boldsymbol{r})}{C_{\max}} \eta_C \propto -\frac{C(\boldsymbol{r})}{\omega^3 U}$, where $\Delta\Gamma(\boldsymbol{r}) = \Gamma^+(\boldsymbol{r}) - \Gamma^-(\boldsymbol{r})$ stands for the differential decay of a chiral dipole emitter coupled to the σ^+ and σ^- circularly polarized modes of the optical cavity at frequency ω. $\Delta\Gamma_0$, F_C, ω_0, Q, $C(\boldsymbol{r})$, $C_{\max}$, η_C, and U are the unmodified differential decay, the chiral Purcell factor, the resonant frequency, the quality factor of the optical cavity, local optical chirality, maximum optical chirality, exciton orientation factor, and total energy of the cavity, respectively.

The chirality of the emitter can be expressed by the contrast of polarization-resolved PL from a 100 nm achiral nanocube. The corresponding dissymmetry factor can be expressed as: $g_A{}^{\pm} = 2\frac{I_{A+}{}^{\pm} - I_{A-}{}^{\pm}}{I_{A+}{}^{\pm} + I_{A-}{}^{\pm}}$, where $I_{A\pm}{}^{\pm}$ are the intensity of opposite chiral components of achiral nanocube PL under opposite chiral excitation. Based on

symmetry of achiral nanocube under opposite excitation, we have ${g_{\mathrm{A}}}^{+} = -{g_{\mathrm{A}}}^{-}$, that is, ${I_{\mathrm{A}+}}^{+} = {I_{\mathrm{A}-}}^{-}$ and ${I_{\mathrm{A}-}}^{+} = {I_{\mathrm{A}+}}^{-}$, respectively. Consequently, $|{g_{\mathrm{A}}}^{\pm}|$ is about $\frac{1}{3}$ in Figure 3.10a and b. In our case, the enhanced/suppressed g_{RPL} of polarization-resolved PL generated from hot spots in GNHs under opposite helicity excitation can be written as:

$$g^{\pm}(\boldsymbol{r}) = 2\frac{{I_{+}}^{\pm} - {I_{-}}^{\pm}}{{I_{+}}^{\pm} + {I_{-}}^{\pm}} = 2\frac{\Gamma^{+}(\boldsymbol{r}){I_{\mathrm{A}+}}^{\pm} - \Gamma^{-}(\boldsymbol{r}){I_{\mathrm{A}-}}^{\pm}}{\Gamma^{+}(\boldsymbol{r}){I_{\mathrm{A}+}}^{\pm} + \Gamma^{-}(\boldsymbol{r}){I_{\mathrm{A}-}}^{\pm}}$$
$$= 2\frac{C^{+}(\boldsymbol{r}){I_{\mathrm{A}+}}^{\pm}/U^{+} - C^{-}(\boldsymbol{r}){I_{\mathrm{A}-}}^{\pm}/\mathrm{U}^{-}}{C^{+}(\boldsymbol{r}){I_{\mathrm{A}+}}^{\pm}/U^{+} + C^{-}(\boldsymbol{r}){I_{\mathrm{A}-}}^{\pm}/\mathrm{U}^{-}} \tag{3.4}$$

We use a spatially averaged net value of optical chirality to consider an overall effect for $\lambda > 600$ nm:

$$g^{\pm} = 2\frac{|\overline{C^{+}}|{I_{\mathrm{A}+}}^{\pm}/U^{+} - |\overline{C^{-}}|{I_{\mathrm{A}-}}^{\pm}/U^{-}}{|\overline{C^{+}}|{I_{\mathrm{A}+}}^{\pm}/U^{+} + |\overline{C^{-}}|{I_{\mathrm{A}-}}^{\pm}/U^{-}} \tag{3.5}$$

which can be expanded in the following form:

$$|g^{+}| = 2\left|\frac{{I_{\mathrm{A}+}}^{+} - {I_{\mathrm{A}-}}^{+} + \frac{|\overline{C^{+}}| - |\overline{C^{-}}|\frac{U^{+}}{U^{-}}}{|\overline{C^{+}}|}{I_{\mathrm{A}-}}^{+}}{{I_{\mathrm{A}+}}^{+} + {I_{\mathrm{A}-}}^{+} + \frac{-|\overline{C^{+}}| + |\overline{C^{-}}|\frac{U^{+}}{U^{-}}}{|\overline{C^{+}}|}{I_{\mathrm{A}-}}^{+}}\right| = 2\left|\frac{{I_{\mathrm{A}+}}^{+} - {I_{\mathrm{A}-}}^{+} + \alpha}{{I_{\mathrm{A}+}}^{+} + {I_{\mathrm{A}-}}^{+} - \alpha}\right| \tag{3.6}$$

$$|g^{-}| = 2\left|\frac{{I_{\mathrm{A}-}}^{-} - {I_{\mathrm{A}+}}^{-} + \frac{|\overline{C^{-}}| - |\overline{C^{+}}|\frac{U^{-}}{U^{+}}}{|\overline{C^{-}}|}{I_{\mathrm{A}+}}^{-}}{{I_{\mathrm{A}-}}^{-} + {I_{\mathrm{A}+}}^{-} + \frac{-|\overline{C^{-}}| + |\overline{C^{+}}|\frac{U^{-}}{U^{+}}}{|\overline{C^{-}}|}{I_{\mathrm{A}+}}^{-}}\right| = 2\left|\frac{{I_{\mathrm{A}-}}^{-} - {I_{\mathrm{A}+}}^{-} + \beta}{{I_{\mathrm{A}-}}^{-} + {I_{\mathrm{A}+}}^{-} - \beta}\right| \tag{3.7}$$

where $\alpha = \frac{|\overline{C^{+}}| - |\overline{C^{-}}|\frac{U^{+}}{U^{-}}}{|\overline{C^{+}}|}{I_{\mathrm{A}-}}^{+}$ and $\beta = \frac{|\overline{C^{-}}| - |\overline{C^{+}}|\frac{U^{-}}{U^{+}}}{|\overline{C^{-}}|}{I_{\mathrm{A}+}}^{-}$. For R-GNHs, we have: $\frac{|\overline{C^{+}}|}{U^{+}} - \frac{|\overline{C^{-}}|}{U^{-}} < 0$ as depicted in Figure 3.16b. As a result, we have $\alpha > 0$ and $\beta < 0$ and correspondingly:

$$|g^{+}| = 2\left|\frac{{I_{\mathrm{A}+}}^{+} - {I_{\mathrm{A}-}}^{+} + \alpha}{{I_{\mathrm{A}+}}^{+} + {I_{\mathrm{A}-}}^{+} - \alpha}\right| > 2\left|\frac{{I_{\mathrm{A}+}}^{\pm} - {I_{\mathrm{A}-}}^{\pm}}{{I_{\mathrm{A}+}}^{\pm} + {I_{\mathrm{A}-}}^{\pm}}\right| = |g_{\mathrm{A}}| \tag{3.8}$$

$$|g^{-}| = 2\left|\frac{{I_{\mathrm{A}-}}^{-} - {I_{\mathrm{A}+}}^{-} + \beta}{{I_{\mathrm{A}-}}^{-} + {I_{\mathrm{A}+}}^{-} - \beta}\right| < 2\left|\frac{{I_{\mathrm{A}+}}^{\pm} - {I_{\mathrm{A}-}}^{\pm}}{{I_{\mathrm{A}+}}^{\pm} + {I_{\mathrm{A}-}}^{\pm}}\right| = |g_{\mathrm{A}}| \tag{3.9}$$

Consequently, this result confirms the enhancement/suppression of dissymmetry fac-

tors in Figure 3.10a-d.

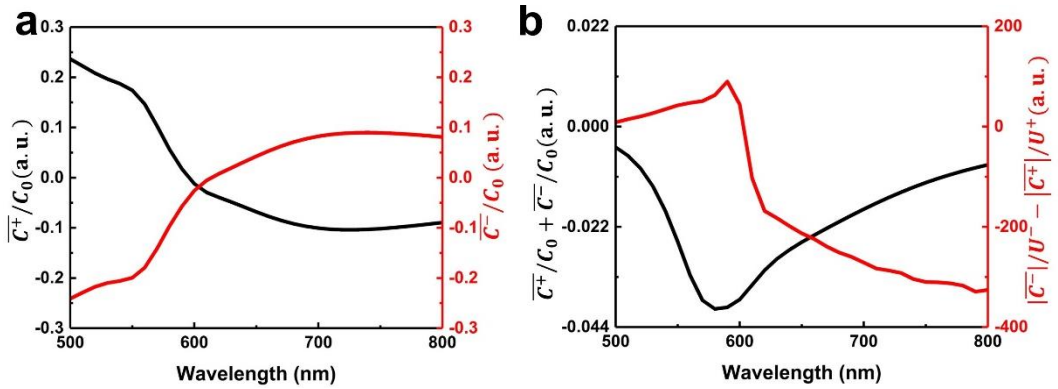

Figure 3.16 (a) The integrated net optical chirality for a L-GNH under RCP (red) and LCP (black) excitation. (b) $\frac{\overline{C^+}}{C_0}+\frac{\overline{C^-}}{C_0}$ represents the totality of the integrated optical chirality for GNHs under RCP and LCP excitation. The non-zero value relates to the chiral antenna mode of the GNHs, with the greatest dissymmetry factor appearing at about 600 nm. For λ > 600 nm, the parameter $\frac{|\overline{C^-}|}{U^-}-\frac{|\overline{C^+}|}{U^+}$ is negative, which manifests the polarization steering activity in polarization-resolved PL.

In the above process, we can also understand the asymmetric chiral response of the GNH by the chiral antenna effect. Under linearly polarized excitation, GNHs' resonant scattering response can be separated in the far field domain with a numerical method ($E_{\mathrm{LCP}}=E_x+iE_y$ and $E_{\mathrm{RCP}}=E_x-iE_y$). The dissymmetry contrast is calculated and depicted in Figure 3.17a, which is in consistence with the net optical chirality under isotropic excitation (Figure 3.16b, $\frac{C_{\mathrm{isotropic}}}{C_0}=\frac{\overline{C^+}}{C_0}+\frac{\overline{C^-}}{C_0}$), both having a valley at about 600 nm. The GNHs' chiral antenna emission procedure is also conducted experimentally through using linearly polarized light (593.5 nm and 532 nm) to generate the CPL signal of GNHs (Figure 3.17b and c). R-GNH exhibit smaller LCP PL than that of RCP, while L-GNH had a reverse scenario. Treating the linearly polarized excitation as a superposition of two excitations with reverse helicity, the enhancement

and suppression g_{RPL} in experimental polarization-resolved chiral PL results depicted in Figure 3.9a and b can be further proved by CPL results as obtained above. Although the intensities are different, the contrast and polarization feature of chiral PL signals obtained under the 593.5 nm and 532 nm excitation conditions have identical performance, which demonstrates a similar chiral-antennas-like behavior of GNHs at wavelengths ranging from 600 to 750 nm.

In addition, Appendices (B) confirms the ITO substrate has no influence on the chiral PL properties of GNHs.

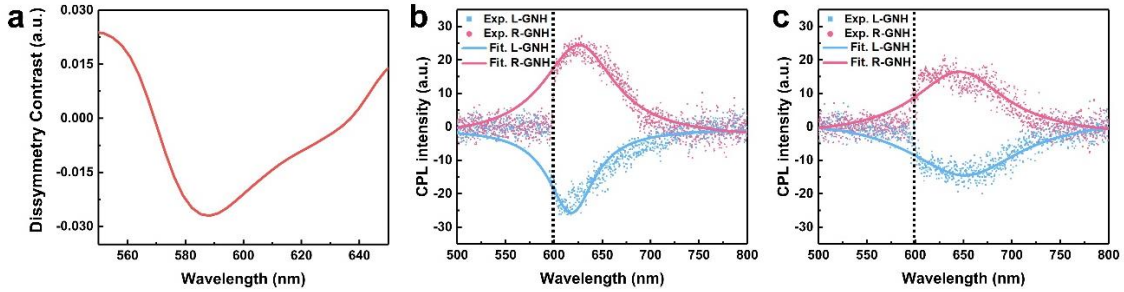

Figure 3.17 (a) Calculated dissymmetry contrast D of CPL. D= (I_{LCP} - I_{RCP})/ (I_{LCP} +I_{RCP}). I_{LCP} and I_{RCP} is derived from the x and y component of the electric field as $I_{LCP} = |E_x + iE_y|^2$ and $I_{RCP} = |E_x - iE_y|^2$. CPL spectra of the R-GNH (pink) and L-GNH (blue) under (b) 593.5 nm and (c) 532 nm laser excitation. The solid lines show the Lorentzian fits of the raw data.

Notably, the chiral PL of the GNH with another kind of morphology (Appendices (C)) has a higher dissymmetry factor, revealing that the construct of the GNH has influence on the chiral PL properties.

3.4 Conclusion

In this chapter, the chiral PL properties of GNHs at the single-particle level are experimentally studied. It was found that, the excited PL signals of GNH enantiomers have a reverse intensity trend in accordance with circular dichroism absorption, while the polarization-resolved chiral PL signal is driven by circular polarization. The phenomenological model quantifies the dissymmetry *g*-factor of chiral PL, having good concordance with our experimental results. The simulated optical super-chiral near field confirms that GNH acts as a chiral antenna via chiral Purcell effect, and leads to preferred emission of polarization-resolved chiral PL signals. Experimental observations indicate that the scattering and PL of the GNHs have single-particle level circular differential performance and specific favored emission handedness, further fostering potential application in the area of chirality-related biology imaging, biosensing, and probing.

Chapter 4 Gold nanohelicoid modulated chiral Raman scattering through a Fabry-Perot cavity

4.1 Introduction

4.1.1 Chiral gold nanoparticle modulation in nanophotonic systems

Newly appeared Au NPs with intrinsic geometric chirality have relative strong and tunable chiral optical activities in the visible region of electromagnetic spectrums, one of which possesses strong CD signals with the *g*-factor up to 0.2. Recently, the investigation of single-particle chiral scatterometry[109] and hyper-Rayleigh scattering of the GNH solution[110] extend those chiral gold nanoparticle chiroptical response properties. These chiroptical responses allow them to modulate the circular polarization of hybrid nanophotonic systems such as quantum dots or two-dimensional transition metal dichalcogenides' (TMDCs) valley polarization. For example, Miandashti *et al*. experimentally demonstrated one kind of these chiral nanoparticles could be successfully used to generate photothermal chirality of AlGaN: Er^{3+} film (Figure 4.1a).[111] The absolute temperature difference of 6K under the RCP and LCP light excitation can be achieved. Kim *et al*.[112] applied chiral nanoparticles on a monolayer WS_2, achieving a large degree of circular polarization; up to 45% (Figure 4.1b).[112] The single chiral nanoparticle makes it possible to excite valley-polarized luminescence with a linearly polarized light excitation.

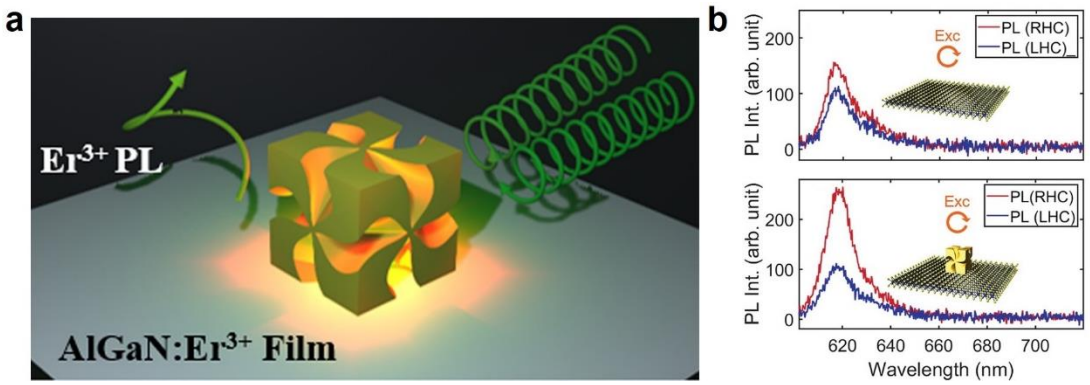

Figure 4.1 (a) Schematic illustration of chiral gold nanoparticles participated photothermal chirality excitation.[111] (b) Polarization resolved PL emission from WS_2 with and without a chiral nanoparticle on WS_2 under right circularly polarized light excitation. [112]

However, the gold nanohelicoid modulated chiroptical activities are not strong and the mechanism behind them is still not clear enough.

4.1.2 Fabry-Perot optical cavity

An optical cavity or optical resonator confines electromagnetic wave at one or more resonant frequencies. The confinement of the standing waves is realized by reflective boundaries formed by two mirrors. The FP cavity is one of the most important microcavities due to its higher resolving power and light throughput.

The FP cavity was invented in 1899,[113] and contains a gap between two mirrors with high reflectance. There are two kinds of FP resonators: planar and curved mirror FP cavities. For a planar mirror FP cavity, a normal incident light will be reflected several times, causing numerous transmission and reflection components. The propagation phase shift for light travelling a single round is expressed as:

$$\delta = \frac{4\pi}{\lambda_0} nL \tag{4.1}$$

where λ_0 is the wavelength in vacuum, n is the refractive index of the cavity medium, and L is the thickness of the cavity. The total transmission can be calculated by:[114]

$$\frac{I_t}{I_i} = \frac{(1-R)^2}{(1-R)^2+4R\ \sin^2(\delta/2)'} \tag{4.2}$$

where I_i, I_t, and R are the overall incident intensity, transmitted intensity, and the reflectance of the mirror, respectively. According to Equation 4.1 and 4.2, the condition for a resonance frequency can be expressed as:

$$\nu_m = m\frac{c}{2nL} \tag{4.3}$$

where m is an integer representing the longitudinal mode order. Now the allowed modal resonance wavelengths can be calculated by:

$$\lambda_m = \frac{2nL}{m} \tag{4.4}$$

To make the series of reflections interfere constructively, the phase shift of the light propagating in the cavity is supposed to be a multiple of 2π. According to Equation 4.3, the free spectral range (FSR) is written as:

$$\nu_f = \frac{c}{2nL} \tag{4.5}$$

The FSR represents the frequency difference between mode order m and m+1. If we do not consider effects such as material dispersion and mirror penetration phenomena, the FSR in terms of wavelength is written as:

$$\lambda_f = \frac{\lambda_m}{m+1} \tag{4.6}$$

Finesse (F) and quality factor (Q) are two important figures-of-merit of FP cavity. F is denoted as:

$$F = \frac{\nu_f}{\Delta\nu} \tag{4.7}$$

where $\Delta\nu$ is the full width at half maximum (FWHM) of the resonance peak. Q is de-

fined as:

$$Q = \frac{\nu_m}{\Delta\nu} \tag{4.8}$$

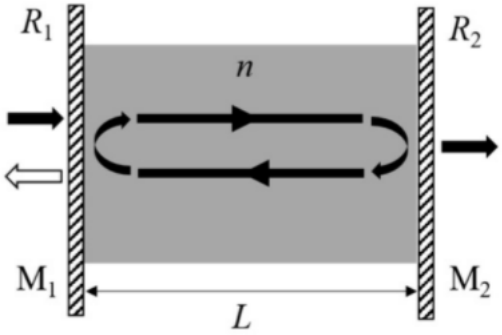

Figure 4.2 Schematic illustration of a Fabry-Perot (FP) cavity with two parallel planar mirrors.[115]

FP cavities have been found to have many useful applications in various fields. For example, a FP cavity with high *F* can be used as an interferometer in uncountable spectroscopy. FP cavity is also widely employed in lasers as a resonator to provide significant optical feedback and spectral discrimination in lasers. Additionally, FP cavity can be applied as an archetype to help study other optical resonators like ring and crystal resonators.[115] Considering FP cavity could enhance the interaction between light and matter, and has the advantage of position insensitivity, it may be a good candidate to further increase the chirality modulation response.

4.1.3 Fabry-Perot cavity coupled with plasmonic nanostructures

The electric field at the interface of metallic nanoparticles could be strongly confined and enhanced by their LSPRs; this feature allows metallic nanoparticles to be widely applied in SERS,[116] nonlinear nanophotonics,[117] biosensing,[118] nanolasing,[119]

and so on. However, the LSPRs of metallic nanoparticles generally have broad bandwidth and high radiative damping.[120] Because their resonance frequencies are extremely sensitive to the particle size, geometry, composition, and surrounding medium, in order to maximize the local field enhancement of metallic nanoparticles to the full extent, approaches such as adjusting the dimension and loading composition of nanoparticles to tune the resonances have been applied.[121, 122]

Photonic cavities could offer amplified optical modes with narrow spectral spreads and provide higher energy confinements with faster responses. Therefore, integrating plasmonic nanostructures with photonic cavities could be an effective approach to generate strong optical confinement and a high quality mode.[123] The plasmonic-cavity hybrid system can further amplify the local electric field intensity of plasmonic nanostructures and consequently enhance light-matter interaction.

Among optical cavities, FP cavities combined with plasmonic nanostructures could realize mode splitting,[124, 125] plasmon relaxation modulation,[126] optimized SERS measurement,[127, 128] etc. Shuford *et al*. combined dimer nanoparticles with a dielectric FP cavity for SERS measurement enhancement (Figure 4.3a).[127] They revealed how a silver disc dimer/ bowtie nanoparticle hybrid system improves the SERS gain. Their results indicate that the array pattern of nanoparticles could also effectively increase the SERS gain. Maier's group demonstrated that a single plasmonic nanoparticle-FP cavity system could narrow the broad localized resonance of nanoparticles, increasing the sensing figure-of-merit significantly (Figure 4.3b).[120] Such system notably improves the detection resolution, manifesting its potential applications in remote sens-

ing and dynamic biosensing. Tsukruk *et al*. studied the multibody coupling behavior of Au nanospheres (Au NSs) on a SiO_2/Si formed FP cavity (Figure 4.3c).[129] It is reported that, the Au NS positioned on the FP cavity outcouples the standing wave inside the cavity to the far field, indicating the formation of highly localized hybrid modes which is apparently different from the original pure FP cavity mode.

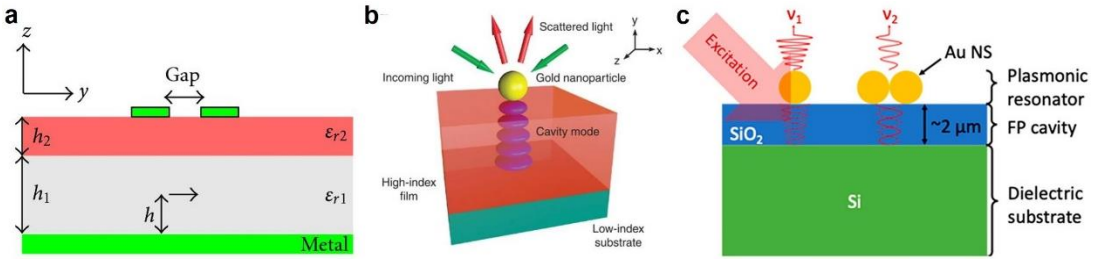

Figure 4.3 (a) Cross view of the disc dimer on top of a double layer FP cavity.[127] (b) Schematic illustration of a hybrid nanoparticle-microcavity system. The FP cavity is formed by high refractive index film deposited on low-index substrates.[120] (c) Schematic illustration of an Au nanosphere monomer and dimer on SiO_2/Si FP cavity.[129]

4.1.4 The chiral Purcell effect in a gold nanohelicoid-FP cavity coupling system

In Chapter 3, we already know that the chiral Purcell effect accounts for the far-field chiral response, so that chiral Purcell effect may also play a key role in studying the circular polarization modulation mechanism in the nanophotonic system.

The Purcell effect describes the emission modification by optical resonator. Previously, it had been demonstrated that optical resonators could also enhance the chiral emissions. Yoo *et al*. expanded the Purcell effect to the chiral light-matter interaction in an optical resonator. They came up with a figure-of-merit chiral Purcell factor F_c,

which reflects the optical resonators' ability on chiral emission modifications and could be used to evaluate the enhancement of CD signal intensity. The chiral Purcell effect is calculated by:[102]

$$F_C \equiv \frac{1}{4\pi^2}\left(\frac{\lambda_0}{N}\right)^3 \left(\frac{Q}{V_C}\right) \tag{4.9}$$

The chiral mode volume V_C is calculated by:

$$V_C \equiv -\frac{\omega U}{cC_{\max}} = \frac{U}{u_{C,\max}} \tag{4.10}$$

where $C_{\max}$, U, and $U_{C,\max}$ are the maximal optical chirality in the cavity, total energy of the cavity, and the maximum chiral energy density in the cavity, respectively. It should be noticed that, u_C is correlated with the degree of light, which is given by:[130]

$$h = -\frac{u_c}{c\omega} \tag{4.11}$$

In fact, the chiral Purcell factor is similar to the standard Purcell factor. The only difference is the mode volume, which is substituted by chiral mode volume.

Soo *et al*. assumed a diffraction-limited lateral cavity with width $L_x = L_y = \frac{\lambda_0}{2}$ as FP cavity to study the chiral Purcell effect in it. λ_0 is the lowest order resonance wavelength. They assumed that, in order to achieve high u_c, the mirrors of the cavity could preserve the polarization upon reflection.[131, 132] The resonance of FP cavity is trapped along the z with L_Z=d. As shown in the Figure 4.4, the CD enhancement $\Delta\Gamma/\Delta\Gamma_0$ could reach 10^2, thus manifesting the resonator could be used as a way to enhance the chiroptical activity as well as the dissymmetry factor. The volume-averaged dissymmetry factor can be increased up to 10^3 inside the FP resonator.

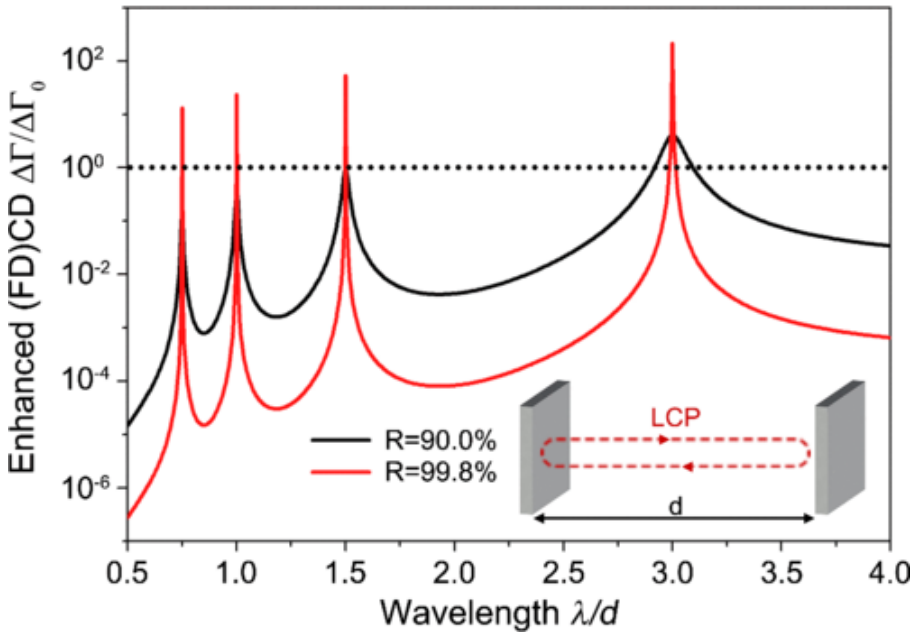

Figure 4.4 Enhanced CD of a polarization-preserved cavity. The mirror reflection coefficients are 90.0% (black line) and 99.8% (red line). The refractive index of the chiral molecule is 1.5. The illustration depicts the polarization situation in the two cavities.[102]

4.2 Experimental methodology

4.2.1 Sample preparation

A 50 μL solution of synthesized GNH was centrifuged two times, and then the centrifuged GNHs were redispersed into 100 μL DI water. A single drop of the diluted solution (about 20 μL) was casted onto a pre-cleaned Si and 1000 nm SiO_2/Si substrate. Upon drying in the air for more than 10-15min, the solution on the substrate was blown by a rubber suction bulb. The majority of GNH clusters were scattered into monomers with large particle-particle distance, thus, enabling the measurement of single nanoparticles.

4.2.2 Single-particle scattering and Raman spectroscopy

The same home-built optical system introduced in Chapter 3 was also applied to measure the chiral scatteromertries and Raman spectrums of the single GNH. A linearly polarized 532 nm/593.5 nm CW laser acted as the excitation source to excite the Si chiral Raman signal of Si or 1000 nm SiO_2/Si substrate. The laser light first traversed through a quarter and a half waveplate, generating circularly polarized light. The single GNH was positioned at the center of the laser target area. To generate the Raman signal, the power of the laser was adjusted to about 750 μW, and the integration time was limited to 8s. To block the excitation source before acquiring the Raman signal, two long pass filters were used during the 593.5 nm excitation. When the excitation source was 532 nm, two 533 nm cut-off wavelength (NF 533-17, Thorlabs, Inc.) notch filters were used. This is because, under 593.5 nm and 532 nm excitation, the silicone Raman signals are supposed to appear at around 613 nm and 547 nm, respectively. The chiral scattering spectrum of the single GNH is measured by the same microscope system equipped with a white light source.

4.3 Gold nanohelicoid modulated chiral Raman scattering through a Fabry-Perot Cavity

4.3.1 Gold nanohelicoid modulated chiral Raman scattering

According to the discussion above, FP cavities are generally composed of an op-

tically transparent medium sandwiched by two parallel reflective surfaces. In our work, considering the fabrication procedure and cost, the FP cavity we use is formed by a layer of 1000 nm SiO_2 sandwiched between Si and GNHs. Here, we only concentrate on the chiroptical modulation performance of GNHs in the FP cavity, the figure-of-merit of the cavity is less relevant. In the future, if the FP cavity with a high-quality factor is required, we could use FP cavities formed by materials with high refractive index difference. Figure 4.5 depicts the schematic illustration of the hybrid system. The circularly polarized incident white/laser light is vertically illuminated on the single GNH structure to excite the scattering signals of GNHs and Raman signals of SiO_2/Si substrate.

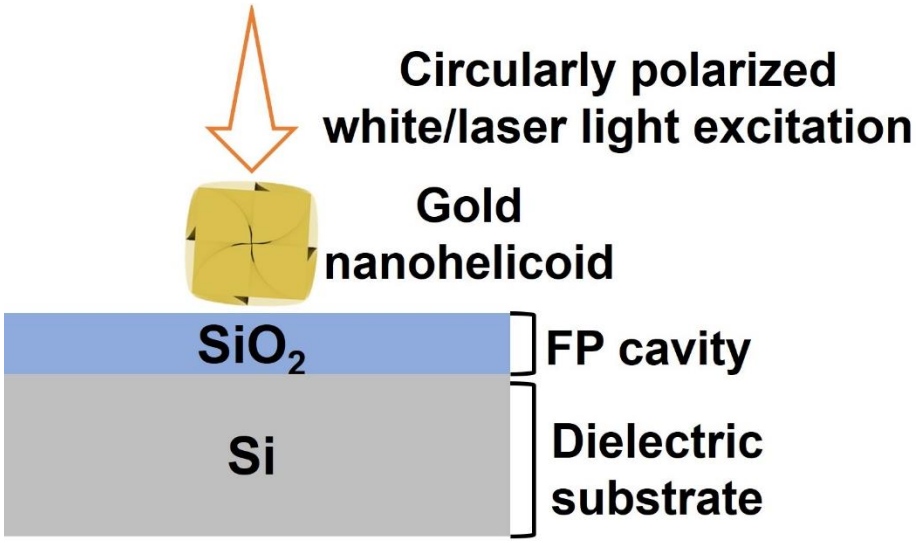

Figure 4.5 Schematic illustration of a single gold nanohelicoid on the SiO_2/Si FP cavity.

Figure 4.6a and b depicted the scattering spectra of the single GNH on the hybrid cavity system. The chiral scatterometry spectra intensities of GNH enantiomers are different under the opposite circular polarization illumination. For one specific GNH

enantiomer, the scattering spectra have two peaks, one is at 550 nm and the other is at 660 nm, and both of them are at the wavelength that is close to the original CD and absorption range of GNHs. In addition, the two peaks' intensities' trend towards RCP and LCP illumination are the same. As a comparison, the scattering spectrums of single GNH on the bare glass substrate are also measured. The scattering spectra given in Figure 4.6c and d are similar with their scattering spectra on the high refractive index ITO glass (Figure 3.8 and 3.12), but have a main peak shift from 650 nm to 600 nm; all of them only have one peak between 500 and 800 nm. This indicates that, the change of substrate refractive index has influence on the plasmonic resonance range. The smaller linewidths of the two peaks in Figure 4.6a and b are about 50 nm, which is much shorter than that of the peak with about 110 nm linewidth in Figure 4.6c and d, manifesting their origin from the standing wave resonance condition of GNH and 1000 nm SiO_2/Si substrate formed by the hybrid FP cavity system.

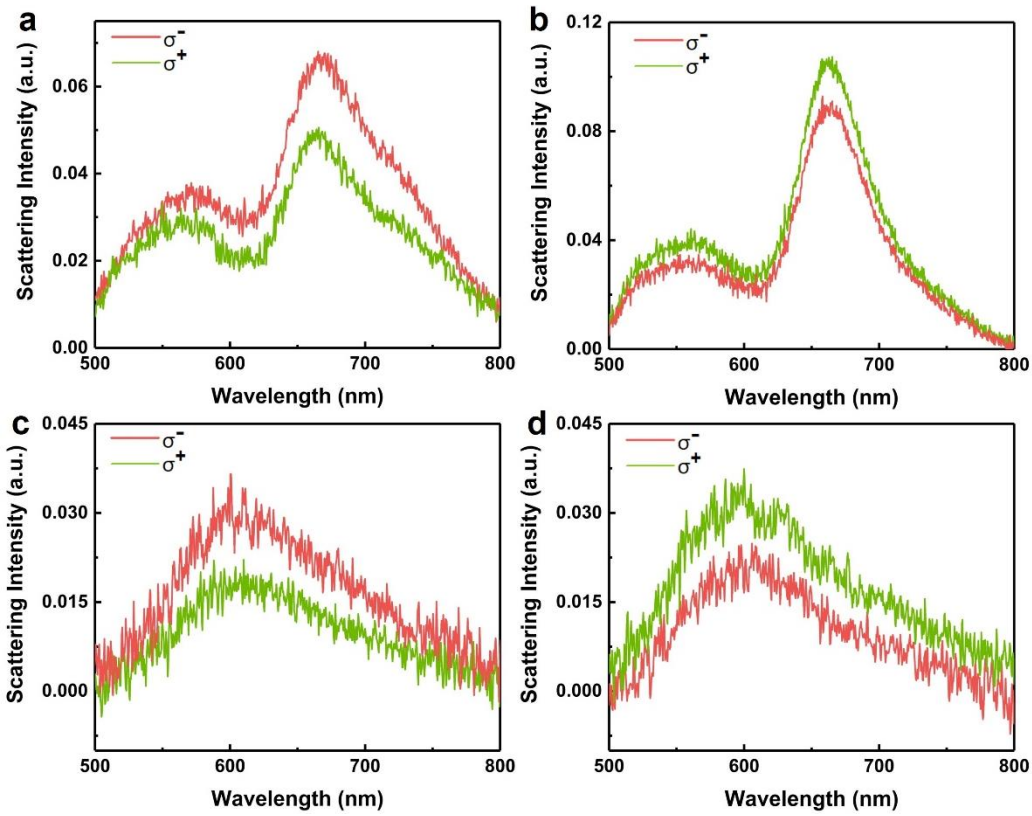

Figure 4.6 Scattering spectrums of the (a) L-GNH and the (b) R-GNH structures on the 1000 nm SiO_2/Si substrate measured under white RCP (red) and LCP (green) light illumination. The data are calculated by averaging 8 different GNHs scattering spectrums. Scattering spectrums of an (c) L-GNH and an (d) R-GNH structure on the pure glass substrate measured under white RCP (σ^-, red) and LCP (σ^+, green) light illumination.

In order to further verify the role of the hybrid FP cavity and the GNH on the scattering spectrum, the same measurements have also been done on a single achiral nanostructure. As shown in Figure 4.7a and b, achiral nanostructures do not have a scattering intensity difference under RCP and LCP illumination, and the two peaks appearing on the 1000 nm SiO_2/Si substrate are located at the same position of that of the GNH. In addition, Figure 4.7c and d show the scattering spectra of L-GNH on the pure Si and 1000 nm SiO_2/Si substrate under the illumination of white light without a circular polarization state, revealing that the two peaks of scattering spectra are at-

tributed to the formed cavity system. Therefore, we could conclude that, the interaction between the GNH and the 1000 nm SiO_2/Si substrate leads to the two strong peaks of scattering spectra and the same intensity trend of the corresponding two peaks. The mechanism of these phenomena will be discussed later.

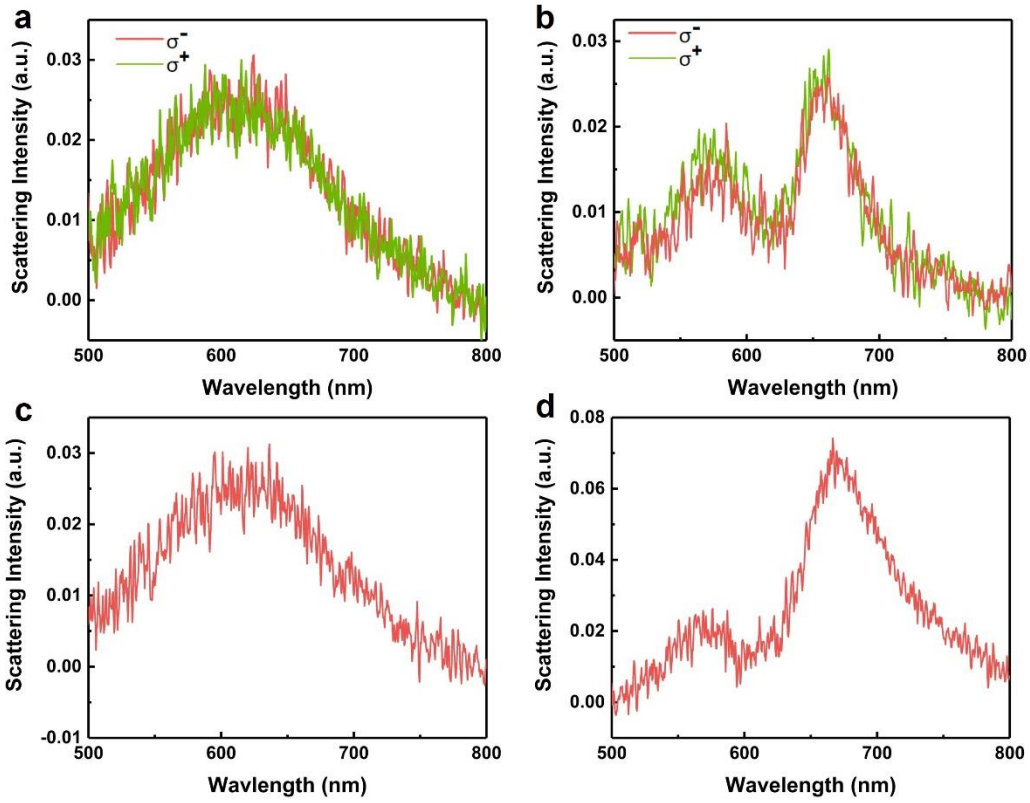

Figure 4.7 Scattering spectra of an achiral structure on (a) pure Si substrate and (b) 1000 nm SiO_2/Si substrate measured under white RCP (σ^-, red) and LCP (σ^+, green) light illumination. Scattering spectrums of a single L-GNH structure on (c) pure Si substrate and (d) 1000 nm SiO_2/Si substrate under white light illumination with no circular polarization state.

To further study the chiral modulation between the FP cavity and GNHs, we also investigated the phenomenon on another optical parameter of the hybrid system. Si Raman spectra of the SiO_2/Si substrate were measured using the same dark-field scattering measurement system with integrated CW lasers. As Figure 4.8a and b show,

under the 593.5 nm RCP light excitation, the L-GNH structure has a stronger Raman signal than that of the LCP excitation, while the Raman signal of R-GNH has a opposite intensity contrast. These experimental results clearly demonstrated that the chiroptical activity of GNH modulates the chiral Raman responses of SiO_2/Si substrate, and the properties of modulated Raman signals are in consonance with the GNH enantiomers. The results given in Figure 4.8c and d show the Raman signals of single GNH on the pure Si substrate, which also have similar results. In addition, Raman signals of the 1000 nm SiO_2/Si and Si substrate with or without the achiral nanostructure reported in Figure 4.9 do not have intensity difference towards RCP and LCP illumination. These results also prove that the Si chiral Raman property is due to the existence of the GNH.

The degree of the Raman intensity differential is evaluated by the dissymmetry factor g_R, which is defined as $g_R = \frac{I_{R+} - I_{R-}}{I_{R+} + I_{R-}}$, where I_{R+} is denoted as the Raman intensity excited by LCP light, and I_{R-} refers to the Raman intensity generated by RCP light. According to the definition, the absolute values g_R of L-GNH and R-GNH on the 1000 nm SiO_2/Si substrate are about 0.22 and 0.25, respectively. Meanwhile, the absolute values of g_R for the GNH enantiomers on the pure Si substrate are around 0.29 (L-GNH) and 0.25 (R-GNH), which are little bit larger than that of the GNH-FP hybrid cavity system.

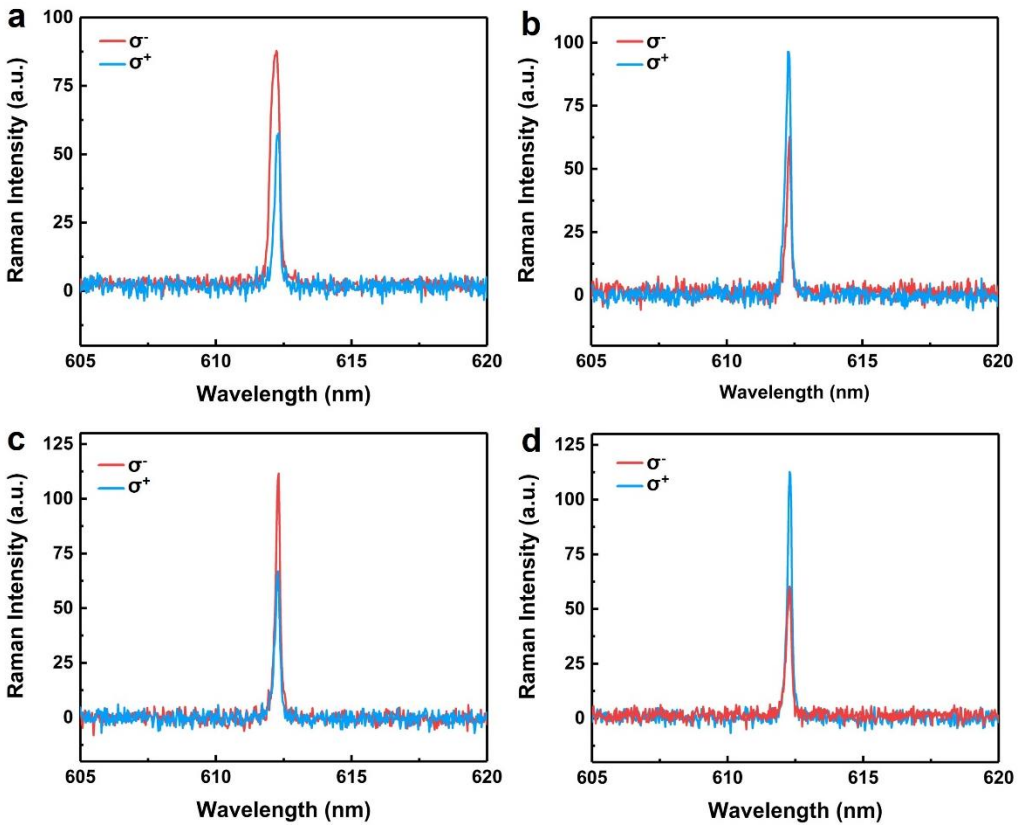

Figure 4.8 (a, b) Raman spectrums of the single (a) L-GNH and (b) R-GNH structure on 1000 nm SiO_2/Si substrate under RCP (σ^-, red) and LCP (σ^+, blue) laser excitation at 593.5 nm. (c, d) Raman spectrums of the single (c) L-GNH and (d) R-GNH structure on pure Si substrate under RCP and LCP laser excitation at 593.5 nm.

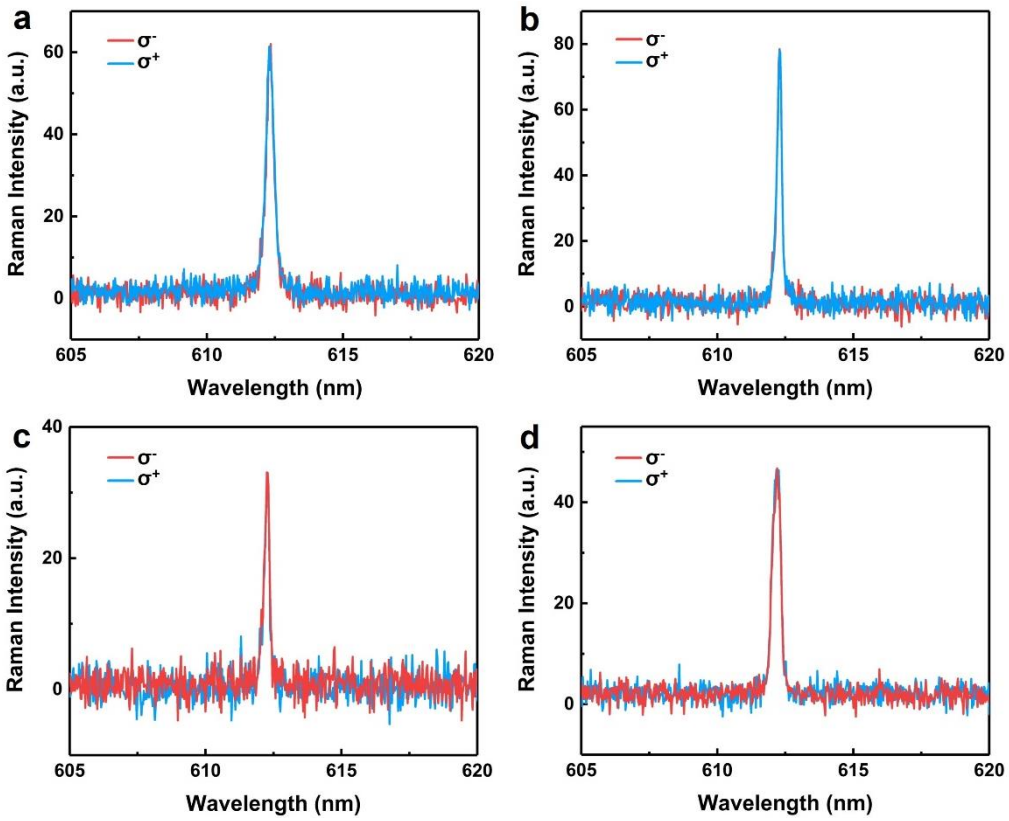

Figure 4.9 (a, b) Raman spectrums of an achiral structure on the (a) 1000 nm SiO_2/Si and (b) pure Si substrate under RCP (σ^-, red) and LCP (σ^+, blue) laser excitation at 593.5 nm. (c, d) Raman spectrums of a (c) bare 1000 nm SiO_2/Si and (d) bare Si substrate under RCP and LCP laser excitation at 593.5 nm.

To make a comparison, the above measurements for the L-/R-GNH on the SiO_2/Si and Si substrate were also conducted at 532 nm excitation. In comparison with the results of 593.5 nm illumination, the Si Raman intensities of the substrate under 532 nm excitation are smaller (Figure 4.10). Accordingly, absolute g_R values of 532 nm excitation are also smaller than that of 593.5 nm, which are about 0.21 for L-GNH and 0.14 for R-GNH on the SiO_2/Si substrate, and 0.20 (L-GNH) and 0.18 (R-GNH) for GNHs on the pure Si substrate. In the meantime, g_R values for the bare Si substrate are larger than on SiO_2/Si substrate, similar to that of the 593.5 nm excita-

tion. These observations indicate that the chiral Raman signals are determined by the intrinsic chiral performances of GNHs as shown in Figure 2.4c: GNHs have smaller chiral response at 532 nm than that at 593.5 nm. This is because both incident laser light and optical responses of substrate are modulated by the GNH. Therefore, to have chiral Raman signals with a higher dissymmetry factor, 593.5 nm illumination is better than 532 nm. This conclusion is similar to the acquisition of higher enhanced chiral PL of GNHs obtained in Chapter 3.

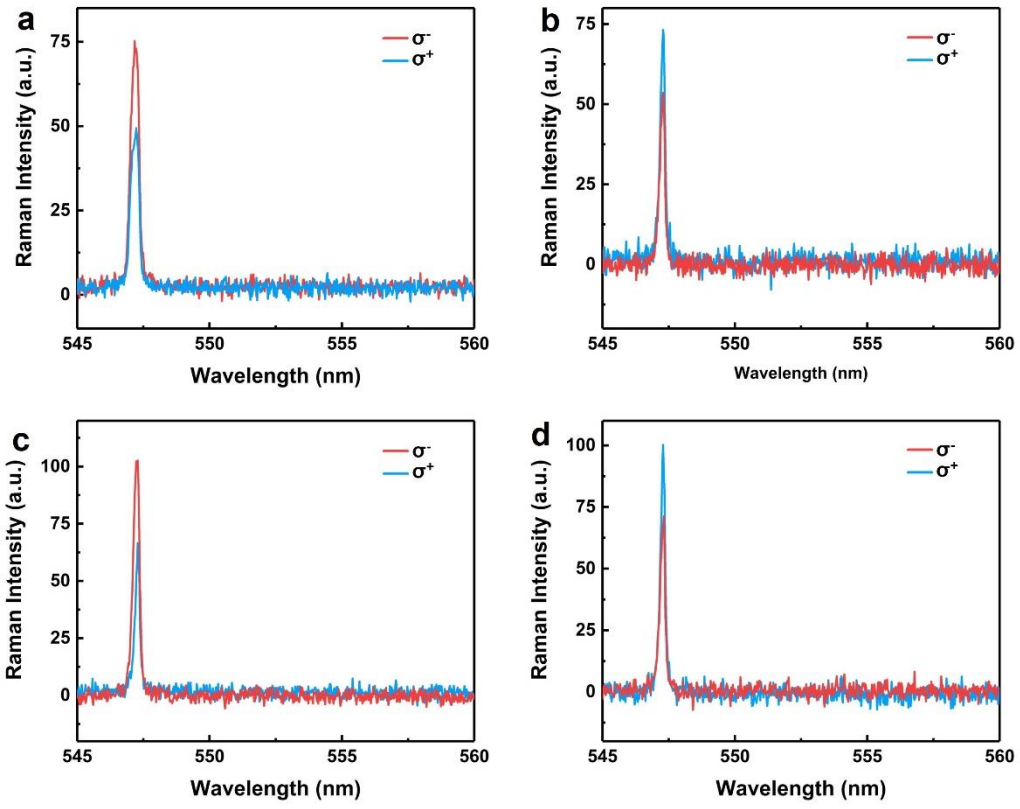

Figure 4.10 (a, b) Raman spectrums of the single (a) L-GNH and (b) R-GNH structure on the 1000 nm SiO_2/Si substrate under RCP (σ^-, red) and LCP (σ^+, blue) laser excitation at 532 nm. (c, d) Raman spectrums of the single (c) L-GNH and (d) R-GNH structure on pure Si substrate under RCP and LCP laser excitation at 532 nm.

Additionally, the scattering and Raman spectrums of GNHs on SiO_2/Si substrate with different thicknesses are given in Appendices (D).

4.3.2 An extended chiral-modulated Fabry-Perot cavity model

To understand the scattering properties of the hybrid system, relevant theoretical analysis and numerical simulations using Lumerical FDTD have been done on an extended chiral-modulated FP cavity model. The FP model describes the reflected electric field amplitude A_{FP} of an air-SiO_2-Si cavity, which can be expressed as:

$$A_{FP} = r_{air-SiO_2}A_0 + \sum_n^{\infty} t_{air-SiO_2}r_{SiO_2-Si}t_{SiO_2-air}(r_{SiO_2-air}r_{SiO_2-Si})^n e^{i\delta_n^{FP}}A_0 \quad (4.12)$$

where A_0 is the amplitude of incident electric field, t is denoted as the amplitude transmittance, r is the amplitude reflectance, and δ_{FP} is the phase difference of the FP cavity. Since $r_{SiO_2-air}r_{SiO_2-Si}$ is about 0, considering the first two terms, the reflectance of the FP cavity can be written as:

$$\rho_{FP} = \frac{I}{I_0} = \frac{AA^*}{A_0^2} = \rho_{air-SiO_2} + \tau_{air-SiO_2}\rho_{SiO_2-Si}\tau_{SiO_2-air} + 2\sqrt{\rho_{air-SiO_2}\tau_{air-SiO_2}\rho_{SiO_2-Si}\tau_{SiO_2-air}}cos\delta^{FP} \quad (4.13)$$

where the intensity reflectance $\rho = r^2$, intensity transmittance $\tau = \frac{n_2}{n_1}t^2 = 1 - \rho$, and the optical path difference induced phase difference is $\delta^{FP} = \frac{4\pi}{\lambda}n_{SiO_2}L$. L represents the thickness of the SiO_2 layer. The first two terms of reflectance in the Equation 4.13 are the reflectance of a multilayer model without FP modulation, which is written as:

$$\rho_{ML} = \rho_{air-SiO_2} + \tau_{air-SiO_2}\rho_{SiO_2-Si}\tau_{SiO_2-air} \quad (4.14)$$

According to the equation, the enhancement and suppression factor $\Delta\rho$ can be calculated by:

$$\Delta\rho_{FP} = \frac{\rho_{FP}}{\rho_{ML}} - 1 = \frac{2\sqrt{\rho_{air-SiO_2}\tau_{air-SiO_2}\rho_{SiO_2-Si}\tau_{SiO_2-air}}}{\rho_{air-SiO_2}+\tau_{air-SiO_2}\rho_{SiO_2-Si}\tau_{SiO_2-air}} cos\frac{4\pi}{\lambda} n_{SiO_2} L \quad (4.15)$$

Using Fresnel's formula and FDTD solution, the reflectance/transmittance at different interfaces, and reflectance of FP cavity can be calculated, respectively. The simulated $\Delta\rho$ of FP and calculated $\Delta\rho$ based on Fresnel's formula as a function of wavelength are plotted in Figure 4.11a. Both intensity and phase match well. The calculated spectra of the SiO_2 layers with different thicknesses also have good alignments with the experiment results.

Since the introduction of plasmonic nanoparticles on a FP cavity can induce an additional phase shift Φ_M of the reflected beam, and elongated penetration depth of the electrical magnetic wave into the upper interface of the FP cavity by a distance of ΔL. Therefore, to qualitatively analyze the scattering features of the 1000 nm SiO_2/Si substrate with the GNH on it, an extended FP model is introduced here:[120]

$$\delta^{LSP-FP} = \frac{4\pi}{\lambda_{LSP-FP}} n_{SiO_2}(L + \Delta L) + \phi_M \quad (4.16)$$

As a result, by ignoring the multi-reflected terms in FP, the scattering amplitude of the hybrid system can be expressed as:

$$A_{LSP-FP} = S^{backward}_{air-GNH-SiO_2} A_0 + t_{air-GNH-SiO_2} r_{SiO_2-Si} S^{forward}_{SiO_2-GNH-air} \delta^{LSP-FP} A_0 \quad (4.17)$$

where S is the amplitude scattering parameter. The scattering cross section $\sigma_{LCP\text{-}FP}$ is given by:

$$\sigma_{LSP-FP} = \sigma^{backward}_{air-GNH-SiO_2} + \tau_{air-GNH-SiO_2}\rho_{SiO_2-Si}\sigma^{forward}_{SiO_2-GNH-air} + 2\sqrt{\sigma^{backward}_{air-GNH-SiO_2}\rho_{SiO_2-si}\tau_{air-GNH-SiO_2}\sigma^{forward}_{SiO_2-GNH-air}} cos\delta^{LSP-FP} \quad (4.18)$$

Similar to the equation without GNHs, the first two terms in Equation 4.18 stand for the scattering cross section of the GNH on a multilayer structure without FP modulation, which is defined as:

$$\sigma_{LSP-ML} = \sigma_{air-GNH-SiO_2}^{backward} + \tau_{air-GNH-SiO_2}\rho_{SiO_2-Si}\sigma_{SiO_2-GNH-air}^{forward} \quad (4.19)$$

The simulated $\sigma_{\text{LCP-FP}}$ of FP and calculated $\sigma_{\text{LCP-ML}}$ based on Equation 4.18 and 4.19 above are shown in Figure 4.11b. In the $\sigma_{\text{LCP-ML}}$ spectrum, there are two peaks in the calculated intrinsic GNHs spectra, which is attributed to the structure of the simulated GNHs design interacting with substrate, while in the $\sigma_{\text{LCP-FP}}$ spectrum of the GNH-FP hybrid configuration, more peaks with narrower linewidths have been seen. The 150 nm single GNH has a broad scattering peak with pronounced spectral oscillations at the long wavelength edge of the visible range, whose linewidth is $\Delta\lambda_{\text{LSPR}}$ 130 nm. The FP cavity modified scattering mode of the GNH has split peaks with a linewidth $\Delta\lambda_{\text{L-SPR}}$ of 60 nm, which is 2.2 times smaller than that of the intrinsic scattering spectrum FWHM of GNHs. In the FP modulated spectrum, two peaks centered at 580 nm and 690 nm agree well with peaks under experimental observation (Figure 4.6). Figure 4.11c describes the electric field distribution in SiO_2 layer under 593.5 nm excitation, displaying a hybrid scattering mode pattern inside the cavity with scattering confined at a limited angle. The large reduction of the linewidth of each individual resonance could significantly improve the Purcell factor or break the detection resolution limit when the hybrid resonance is applied in refractive index sensing applications.[133]

The simulated enhancement and suppression factor can be written as:

$$\Delta\sigma_{LSP-FP} = \frac{\sigma_{LSP-FP}}{\sigma_{LSP-ML}} - 1 \quad (4.20)$$

and calculated factor is expressed as:

$$\Delta\sigma_{LSP-FP} = \frac{2\sqrt{\sigma^{backward}_{air-GNH-SiO_2}\rho_{SiO_2-Si}\tau_{air-GNH-SiO_2}\sigma^{forward}_{SiO_2-GNH-air}}}{\sigma^{backward}_{air-GNH-SiO_2}+\tau_{air-GNH-SiO_2}\rho_{SiO_2-Si}\sigma^{forward}_{SiO_2-GNH-air}} cos\frac{4\pi}{\lambda_{\mathrm{LSP-FP}}} n_{\mathrm{SiO_2}}(L + \Delta L) + \phi_M \quad (4.21)$$

The calculated factor as a function of wavelength is depicted in Figure 4.11d. The phase is optimized to match the result of the simulated factor. Fitted ΔL=110 nm and Φ_M=0.29π are obtained. The resonance condition of the particle-cavity to obtain a maximum reflection is modified to be written as:

$$2\pi m = \frac{4\pi}{\lambda_{\mathrm{LSP-FP}}} n_{\mathrm{SiO_2}}(L + \Delta L) + \phi_M \quad (4.22)$$

where π is the additional phase of the half wave loss, *m* is the FP mode order number at the resonance wavelength $\Delta\lambda_{LSPR}$, $n_{\mathrm{SiO_2}}$ is the refractive index of the SiO_2 layer, and *d* is the thickness of the SiO_2 layer. The matching provides the correct mode order number of each resonance. In Figure 4.11d, the coarsely matched order number of five peaks at 430 nm, 490 nm, 570 nm, 690 nm, and 860 nm are 8, 7, 6, 5, and 4 respectively. When the thickness of the FP cavity varies, the calculated peak position using the same ΔL and Φ_M still match the measured peak position well, confirming the accuracy of the extended model.

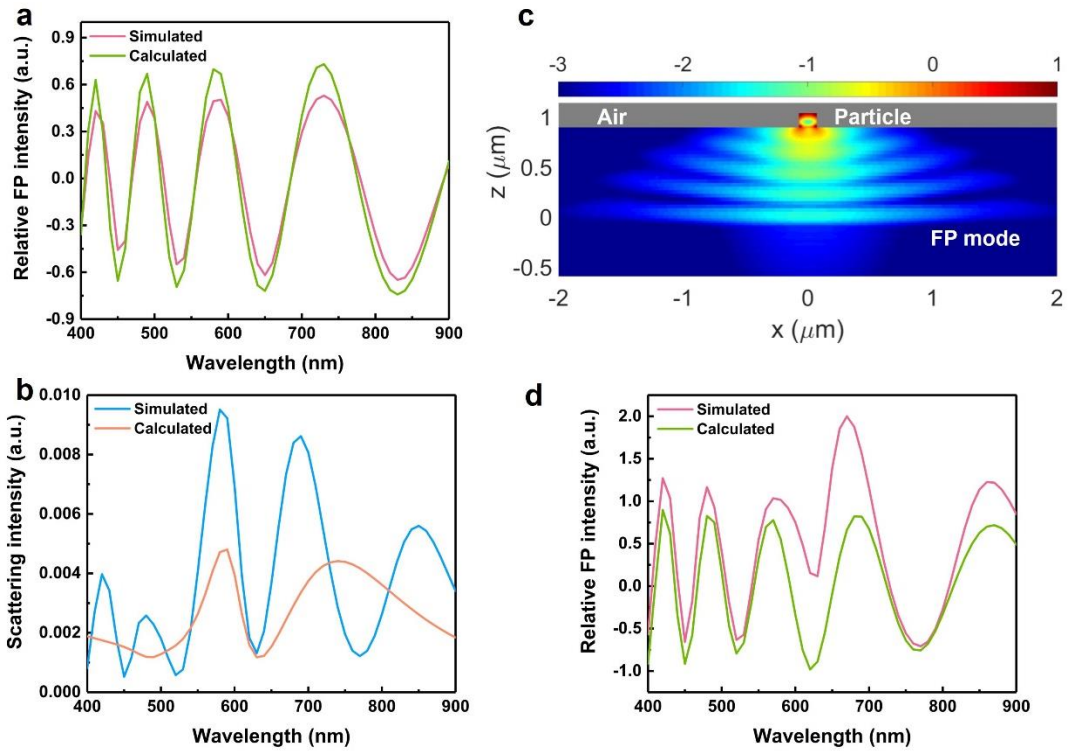

Figure 4.11 (a) Simulated and calculated relative intensity of the bare 1000 nm SiO_2/Si FP cavity. (b) Simulated and calculated scattering spectra of the GNH on the 1000 nm SiO_2/Si FP cavity. (c) Electric field distribution of a cross section of the GNH on SiO_2/Si substrate hybrid FP cavity system. (d) Simulated and calculated relative intensity of the GNH on the 1000 nm SiO_2/Si FP cavity.

The chiral properties of the hybrid system are investigated by its different extinctions to RCP and LCP. Compared with GNHs in free space, the reflection of Si substrate induces the excitation spin flipping. Thus:

$$\sigma_{LSP-FP}{}^{\pm} = \sigma_{air-GNH-SiO_2}^{backward}{}^{\pm} + \tau_{air-GNH-SiO_2}{}^{\pm}\rho_{SiO_2-Si}\sigma_{SiO_2-GNH-air}^{forward}{}^{\mp} + 2\sqrt{\sigma_{air-GNH-SiO_2}^{backward}{}^{\pm}\rho_{SiO_2-Si}\tau_{air-GNH-SiO_2}{}^{\pm}\sigma_{SiO_2-GNH-air}^{forward}{}^{\mp}}\cos\delta^{LSP-FP} \quad (4.23)$$

where the superscripts ± indicate the RCP and LCP scattering direction. Subscripts backward and forward indicate the transmission and reflection condition. Similarly,

the first two terms are the scattering cross section of the GNH on the multilayer structure without FP modulation, which can be expressed as:

$$\sigma_{LSP-ML}{}^{\pm} = \sigma_{air-GNH-SiO_2}^{backward}{}^{\pm} + \tau_{air-GNH-SiO_2}{}^{\pm}\rho_{SiO_2-Si}\sigma_{SiO_2-GNH-air}^{forward}{}^{\mp} \quad (4.24)$$

The simulated CD of GNH on the FP cavity is defined as: $CD_{LSP-FP} = \sigma_{LSP-FP}{}^{+} - \sigma_{LSP-FP}{}^{-}$. The calculated CD of GNH in the multilayer reflective model is defined as: $CD_{LSP-ML} = \sigma_{LSP-ML}{}^{+} - \sigma_{LSP-ML}{}^{-}$. CD_{LSP-FP} and CD_{LSP-ML} as functions of wavelength are plotted in Figure 4.12a.

In comparison with the simulated CD of the GNH on the infinity thick SiO_2 (green line in Figure 4.12a), the sign of the calculated CD at 550 nm flips across the calculated region. This is due to the dominant CD factor mainly originating from the reflective part (second term in Equation 4.24) in our model. Interestingly, the CD of the GNH-FP cavity hybrid system has more complex features, including several peaks and valleys. At the FP modulated resonance peaks, i.e., 590 nm and 690 nm, negative CD signs are observed. The two peaks with the same intensity contrast of the hybrid system are mainly caused by the direction change of *k* in reflection. When one specific circularly polarized light reflects from the bottom of the FP cavity, the reflection causes the spin state to change to the opposite, leading to the change of *k* direction, thus the flip of scattering signal. Qualitatively, the CD difference can be written as:

$$\Delta CD = CD_{LSP-FP} - CD_{LSP-ML} = (\sigma_{LSP-FP}{}^{+} - \sigma_{LSP-ML}{}^{+}) - (\sigma_{LSP-FP}{}^{-} - \sigma_{LSP-ML}{}^{-}) = 2(\sqrt{\sigma_{air-GNH-SiO_2}^{backward}{}^{+}\rho_{SiO_2-Si}\tau_{air-GNH-SiO_2}{}^{+}\sigma_{SiO_2-GNH-air}^{forward}{}^{-}} - \sqrt{\sigma_{air-GNH-SiO_2}^{backward}{}^{-}\rho_{SiO_2-Si}\tau_{air-GNH-SiO_2}{}^{-}\sigma_{SiO_2-GNH-air}^{forward}{}^{+}})cos\frac{4\pi}{\lambda_{LSP-FP}}n_{SiO_2}(L+\Delta L) + \phi_M \quad (4.25)$$

Simulated and calculated results using the same phase parameters are shown in Figure 4.12b, which have a good agreement in phase. When preforming the calculations of the FP cavity with different thicknesses, results also agree well.

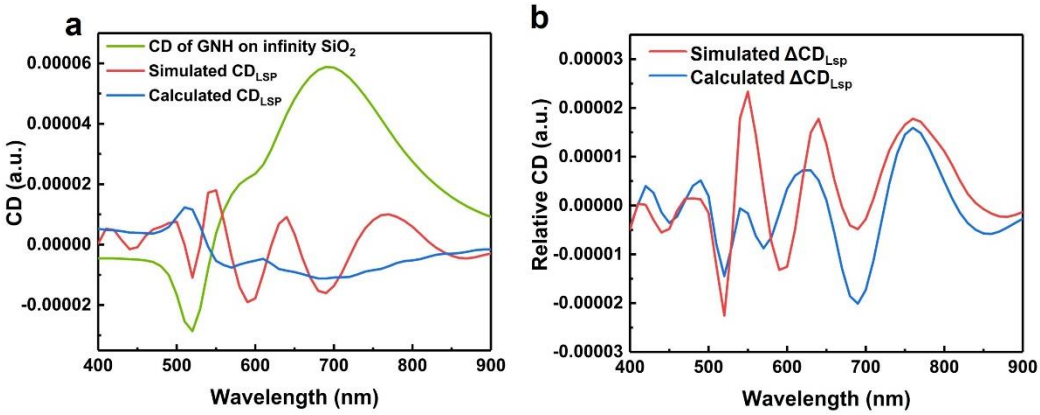

Figure 4.12 (a) The simulated (red) and calculated (blue) CD of the GNH on the 1000 nm SiO_2/Si substrate using the FP modulated model. The CD of the GNH on the infinity SiO_2 substrate. (b) The simulated (red) and calculated (blue) CD difference of the GNH on the 1000 nm SiO_2/Si substrate using the FP modulated model.

4.4 Conclusion

In this chapter, we systematically studied the chiral scattering spectra of GNHs on a FP microcavity at the single-particle level. The corresponding scattering spectra have two strong peaks with the same intensity trends under different circular polarization illumination, and both of them are corresponding to their absorption spectrum. In addition, the Si Raman intensities of the SiO_2/Si substrate under LCP and RCP light excitation are modulated by the GNH on it. The dissymmetry *g*-factor of the Raman intensity contrast can reach around 0.2. A detailed theoretical analysis including an extended FP model and numerical calculations has been given to reveal the single-

particle circularly polarized scattering spectra and chiral Raman feature of the GNHs-FP cavity hybrid system.

Chapter 5 Gold nanohelicoids based chiral molecule recognition using Raman spectroscopy

5.1 Introduction

5.1.1 Raman spectroscopy

Raman spectroscopy is a technique that utilizes the intra- and inter vibrational modes of molecules to study the structural information of the molecules. The Raman effect results from the inelastic scattering of light by matter, and it provides the insight into the low frequency modes and vibrations of systems.

When photons are scattered, dominant elastic scattering is Rayleigh scattering, and a very small amount of inelastic scattering is Raman scattering.[134] Figure 5.1 depicts the Rayleigh and Raman scattering processes, which both contain scattering incident light from a virtual state. Rayleigh scattering starts from incident photons, which are excited to the virtual state and then transit back to the ground state. During this process, there is no energy change. Raman scattering results from the incident photon emitted from the virtual state to the first excited state. The frequency of the emitted photon changes down (Stokes Raman scattering) or up (anti-Stokes Raman scattering).[135] The frequency of scattered light can be expressed as: $\omega = \omega_p \pm \omega_{\mathrm{osc}}$,[136] where ω_{osc} is the lattice or molecule vibration frequency, and ω_{p} is the frequency of incident photon. "±" represents the energy conservation state. The collision between the photon and molecules leads to different vibrational energy, thus causing

the energy and frequency shift.

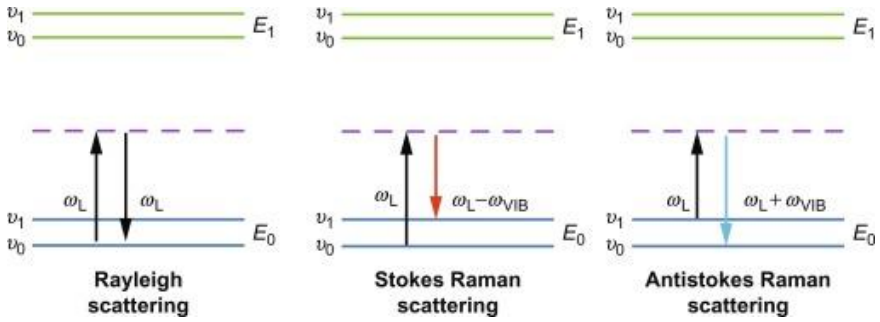

Figure 5.1 Schematic illustration of Rayleigh scattering and two kinds of Raman scattering processes.[135]

5.1.2 Surface enhanced Raman spectroscopy

SERS is a surface-sensitive spectroscopy technique that enhances the Raman scattering of molecules by the LSP induced amplification of electromagnetic fields, which allows analytes with low concentration to be sensed. The enhanced Raman spectrum of pyridine on a roughened silver film was observed in 1974, however, at that time, scientists did not discern that the enhanced spectrum accounts for new phenomena.[137] In 1977, the concept of SERS was reported, and mechanisms of the observed enhancement were proposed.[138] Subsequently, the research on SERS has grown exponentially in various fields including sensing, imaging, molecule detection, etc.[139, 140]

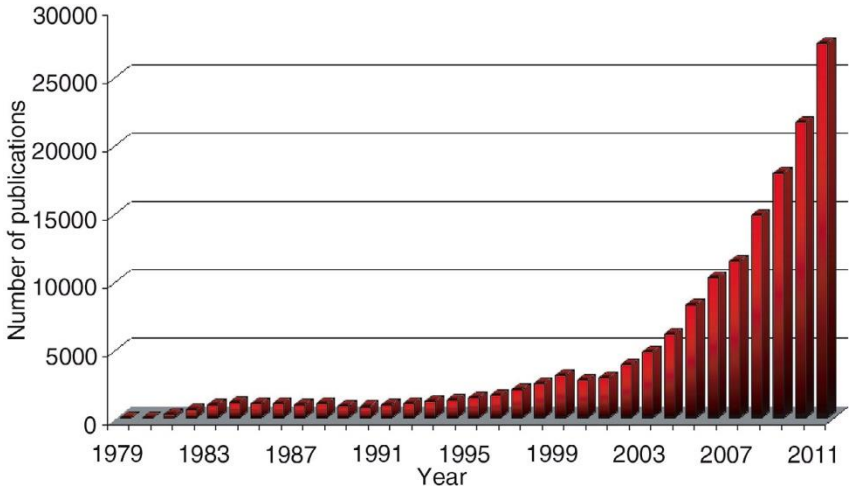

Figure 5.2 Number of publications on surface enhanced Raman (SERS) technique research.[139]

The electromagnetic enhancement is the widely accepted mechanism that causes the Raman signal enhancement.[141] The enhancement is attributed to the LSPRs induced light amplification. The electromagnetic enhancement for SERS can reach factors of ~10^{10}-10^{11} determined by the plasmonic material used for the SERS.[142] In general, the enhancement factor is estimated by the magnitude of the localized electric field to the fourth power.[141]

Another mechanism in signal enhancement is chemical enhancement. Charge transfer mechanism is a type of chemical enhancement, which occurs when the excitation wavelength is resonant with metal-molecule charge transfer electronic states. Theoretically, the chemical enhancement factor could reach up to 10^3 based on the time dependent density functional theory.[143]

Electromagnetic and chemical enhancement results lead to the resulting SERS enhancement, which is calculated by the product of the two kinds of enhancement (Figure 5.3a).[136] The effective SERS enhancement greatly relies on the interaction be-

tween adsorbed molecules and the plasmonic nanostructure interface. Au, Ag, and Copper (Cu) are three commonly used SERS substrates. Compared with Cu, Au and Ag are more often used SERS substrates because they are more stable in the air. The LSPRs of these three metals ranges from the visible to infrared region, which could satisfy most Raman measurements (Figure 5.3b). In the past few decades, scientists have been working on improving the configuration and structure of the substrate to further increase the SERS enhancement factor. In recent years, Au or Ag NPs with different shapes and coatings were developed as new category substrates for SERS measurement. Taking advantage of these new substrates, SERS have been demonstrated to have significant applications in the field of biosensing,[144] electrochemistry,[145] as well as single molecule detection.[146]

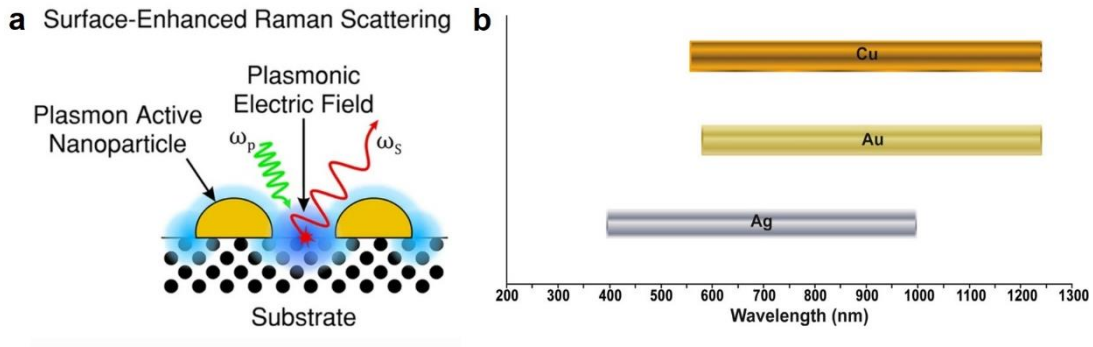

Figure 5.3 (a) Schematic illustration of SERS process.[136] (b) LSPRs range of Ag, Au and Cu.[139]

5.1.3 Raman optical activity

Raman optical activity (ROA) measures the small intensity difference between Raman scattering in RCP and LCP light. It is a chiral optical technique manifesting the vibrational optical activity.[147] The fundamental mechanism research of ROA start-

ed from Atkins and Barron.[148] Compared with vibrational circular dichroism (VCD), ROA is more sensitive on reflecting the 3D structural conformational information of chiral molecules in the solution,[149] and there is no limitation on the size and type of molecules. There are four forms of ROA, which are determined by the incident polarization and scattering geometry. The most common ROA is incident circular polarization (ICP) ROA, whose scattered intensities are excited by RCP and LCP incident light. The other form is scattered circular polarization (SCP) ROA, whose incident excitation is linearly polarized, and whose scattered light is resolved into RCP and LCP components. The last two forms are dual circular polarization one and two, whose incident and scattered light are both circularly polarized.[150] Generally, circular intensity difference (CID) is used to quantify the degree of Raman optical activity: $\Delta = \frac{I^R - I^L}{I^R + I^L}$. I^R and I^L are the scattered intensities in RCP and LCP incident light, respectively.

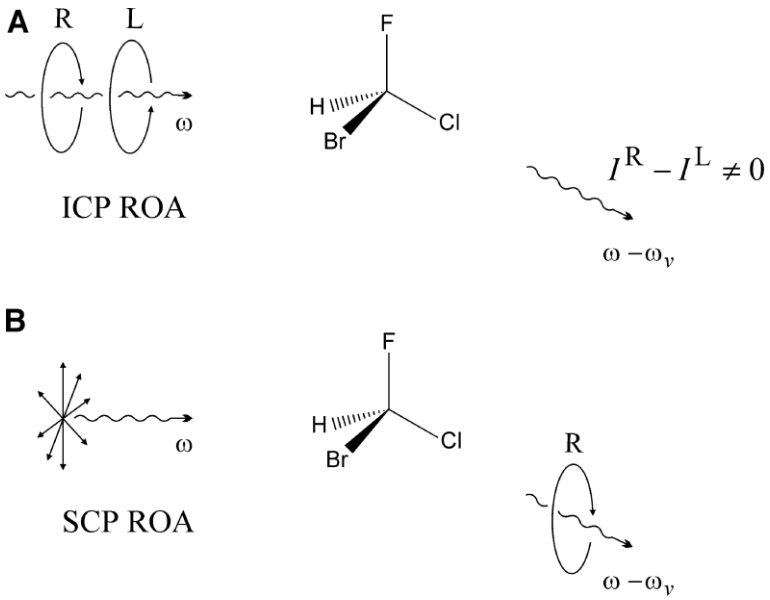

Figure 5.4 (A) Incident circular polarization (ICP) and (B) scattered circular polarization (SCP) Raman optical activity (ROA) form with incident light of angular frequency ω.[150]

ROA is widely applied in the study of proteins, viruses, carbohydrates, etc. It provides extra and intense information of the most rigid and chiral parts of the structure, and is a more sensitive technique on structural related measurement than Raman spectroscopy.[151] However, it is restricted by the intrinsic weakness scattering radiation of molecules, requiring long data accumulation times and high concentrations of the sample. Generally, the ROA intensities are three to five orders of magnitude weaker than the normal Raman scattering.[152] This is because ROA requires higher-order electric quadrupole and magnetic dipole to obtain circular intensity difference.[153] Applying SPR to the sample to excite SERS is an underlying approach to increase the intensity of ROA response. Some research has been done on surface-enhanced Raman optical activity (SEROA).[154] The theory of SEROA was first brought up by Efrima who revealed that apart from the evanescent electric field of metal surfaces, electric field gradient could also enhance the ROA signal.[155, 156] Osinska *et al*. measured the SEROA spectra of cysteine enantiomers by using a roughened silver-based system;[157] although the authors could not observe the SERS spectra of L-/ D-Cys. Ostovar *et al*. observed a chiral effect on the surface enhanced resonant Raman spectroscopic spectrum of the achiral benzotriazole dye by using an achiral SiO_2 coated Ag NP and chiral analyte.[158] However, until now, it is still hard to obtain reliable SEROA spectrum without spectral artifacts. Since the metal surface may change the circular polarization state of reflected electromagnetic waves, it induces an elliptically polarized light.[159] Additionally, it was found that the ROA signal is molecule-substrate orientation sensitive.[152, 153]

Considering the drawbacks of ROA, recently Jin's group reported a new enantioselective differentiating approach on traditional Raman spectroscopy with the assistance of chiral Au clusters.[160] However, this approach is limited in its ability to recognize all chiral molecules. This is because, the inorganic crystal interfaces formed by chiral atoms' arrays have different absorption abilities toward organic enantiomers.[161, 162]

5.2 Experimental methodology

5.2.1 Sample reparation

To assess the Raman enantio-discrimination ability of GNH, chiral molecules including cysteine (Cys), glutathione (GSH) and tryptophan (Trp) were selected. First, pre-prepared 3 mL vials of GNH solutions were centrifuged two times to remove the attached CTAB, and then the solution was redispersed in 150 μL DI water. Second, the condensed 150 μL GNH solution was mixed with 150 μL 200 μM L-/D-Cys, or 300 μM L-GSH, or 200 μM L-/D-Trp solution. When adding the L-/D-Trp to the GNH solution, the pH was adjusted to about 9 by adding propriate 0.1 M sodium hydroxide (NaOH), since the Trp is more stable in an alkaline environment.[159] After gently stirring the mixed solution overnight, 100 μL the mixture was dropped onto the 1 cm × 1 cm Piranha-etched glass. Finally, the dried sample was positioned on the sample stage of the Raman spectrometer for further measurement. Four kinds of coupled samples were made, which include L-GNH/ L-Cys, L-GNH/ D-Cys, R-GNH/ L-Cys, R-GNH/

D-Cys, L-GNH/L-Trp, L-GNH/D-Trp, R-GNH/L-Trp, R-GNH/D-Trp, L-GNH/L-GSH, and D-GNH/L-GSH.

The attachment of Cys and GSH on GNHs are due to the formation of Au-S bonding between Cys and GNHs,[163] while the attachment of Trp is due to the Au-N bonding.[164]

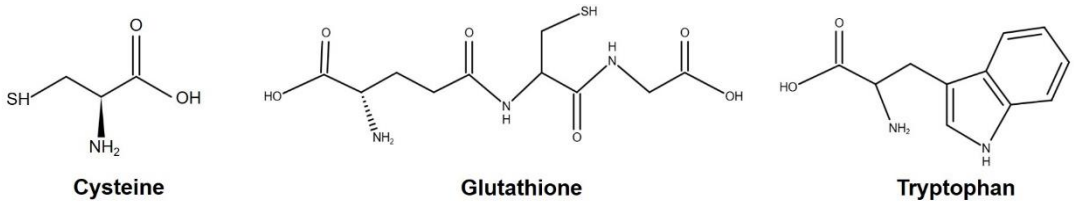

Figure 5.5 Molecular structures of cysteine, glutathione, and tryptophan.

Glass with Piranha treating is to enhance its hydrophilic ability, making the GNH mixture dispersed uniformly. Before hydrophilic treatment, glasses were cleaned by ultrasonication in acetone, ethanol, and DI water. After cleaning, they were immersed in Piranha solution (H_2SO_4 (95%–98%) / H_2O_2 (30%) = 7:3) at 100°C for 1h, and then were rinsed and ultrasonically cleaned for 30 min with pure ethanol and water.[165] The obtained functionalized glasses were dried in a stream of N_2 gas for the further sample preparation.

5.2.2 Raman characterization

The Raman spectrums of the samples were recorded by a commercial confocal Raman spectrometer (Witech alpha300 R). The sample was focused under a 100× microscope and the Raman signals were collected under 633 nm excitation. The laser

power was set to be 0.5 mW and the integration time was 15s with 2 times accumulation. The use of 633 nm rather than 532 nm as excitation source is because the gold nanohelicoid has stronger CD response (Figure 2.4c) at 633 nm. The low power of laser and long accumulation time is to avoid damaging the chiral morphology of nanohelicoids and obtain reliable signals. For each sample ten Raman spectrums were measured at different spots.

5.3 Gold nanohelicoid assisted Raman enantioselective recognition

First, we measured the CD and Raman spectrums of pure L-Cys and D-Cys as given in Figure 5.6. The CD spectra of Cys enantiomers show a mirror image CD response while the Raman spectra are almost the same indicating the Raman spectroscopy cannot be used to distinguish Cys enantiomers directly. In this work, we take advantage of GNHs for Cys enantiomers discrimination using Raman spectroscopy.

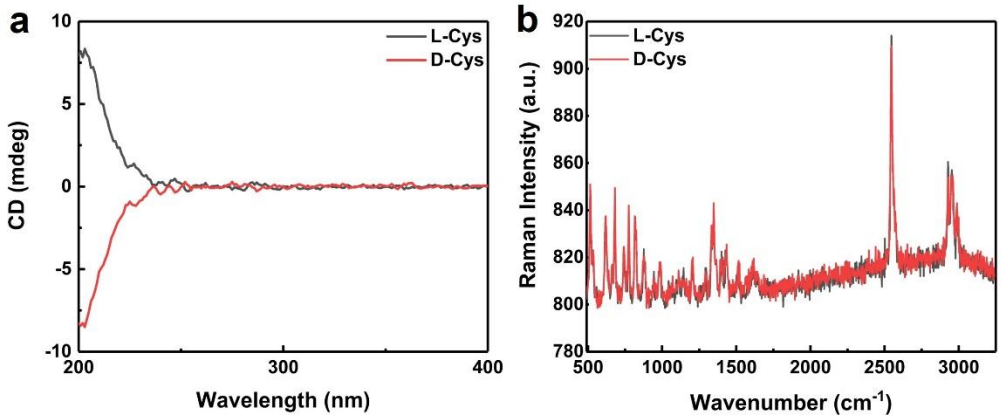

Figure 5.6 (a) CD spectra of 1 mM L-Cys and D-Cys solution. (b) Raman spectra of pure 10mM L-Cys and D-Cys.

After mixing Cys with GNHs in solution and dried on glass substrate, it is revealed that for one handedness GNH attached with L-Cys and D-Cys, their characteristic Raman peaks (497 cm^{-1}) are the same but differ in intensity. As shown in Figure 5.7a, the L-GNH/ D-Cys is apparently stronger than that of L-GNH/ L-Cys. Similar results can also be found in R-GNH mixtures (Figure 5.7b), where the intensities for R-GNH/ L-Cys are stronger than that of R-GNH/ D-Cys. The relative standard deviation (RSD) of the peak at 497 cm^{-1} of the 10 Raman spectra for L-GNH/ D-Cys, L-GNH/ L-Cys, R-GNH/ L-Cys, and R-GNH/ D-Cys are 1.5%, 2.2%, 1.7%, and 2.4%, respectively. These RSD values manifest that the collected Raman spectra have good reproducibility. The peak at 497 cm^{-1} corresponds to the S-S bond stretching of cystine. This is because during the several hours' sample drying process, Cys is easily oxidized into cystine through S-S bond formation.[160, 166]

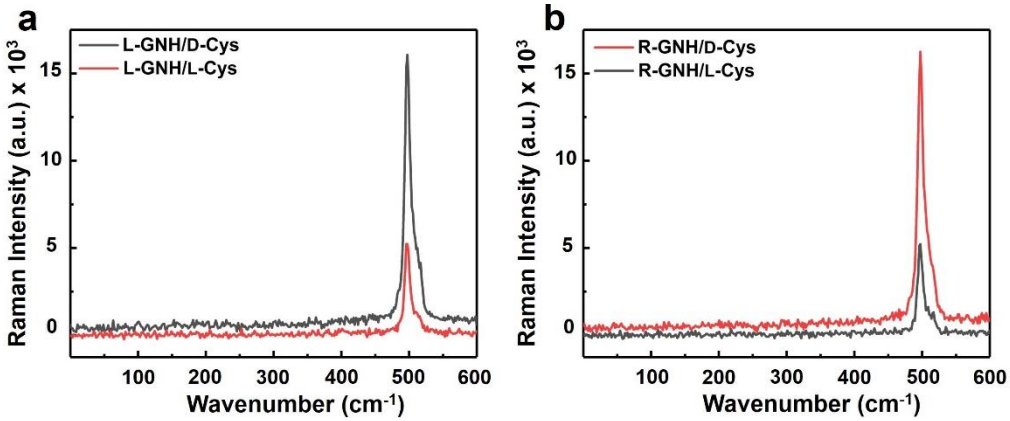

Figure 5.7 Raman spectra of (a) L-GNH/ D-Cys and L-GNH/ L-Cys and (b) R-GNH/ D-Cys and R-GNH/ L-Cys at around 497 cm^{-1}.

We use the discrimination index (Di) to quantitively evaluate the recognition abilities of the GNHs toward Cys enantiomers. The Di is correlated with the intensity differences of Raman signals, which can be written as:

$$\mathrm{Di\ (R-GNH)} = \frac{I(\mathrm{R-GNH/\ D-Cys}) - I(\mathrm{R-GNH/\ L-Cys})}{I(\mathrm{R-GNH/\ D-Cys}) + I(\mathrm{R-GNH/\ L-Cys})} \quad (5.1)$$

$$\mathrm{Di\ (L-GNH)} = \frac{I(\mathrm{L-GNH/\ D-Cys}) - I(\mathrm{L-GNH/\ L-Cys})}{I(\mathrm{L-GNH/\ D-Cys}) + I(\mathrm{L-GNH/\ L-Cys})} \quad (5.2)$$

where *I* represents the averaged intensity of 10 Raman spectra for each samples. The calculated Di of R-GNH and L-GNH are 0.613 and -0.615, respectively. It can be seen from Figure 5.8 that the Di curves of R-GNH and L-GNH show a mirror image, which is similar to their CD spectra. This feature, to some extent, also reflects the chirality degree of GNHs, manifesting that Cys enantiomers can be used as chirality indicators to detect GNHs' chirality without obtaining their absorption activity in the UV-vis region.

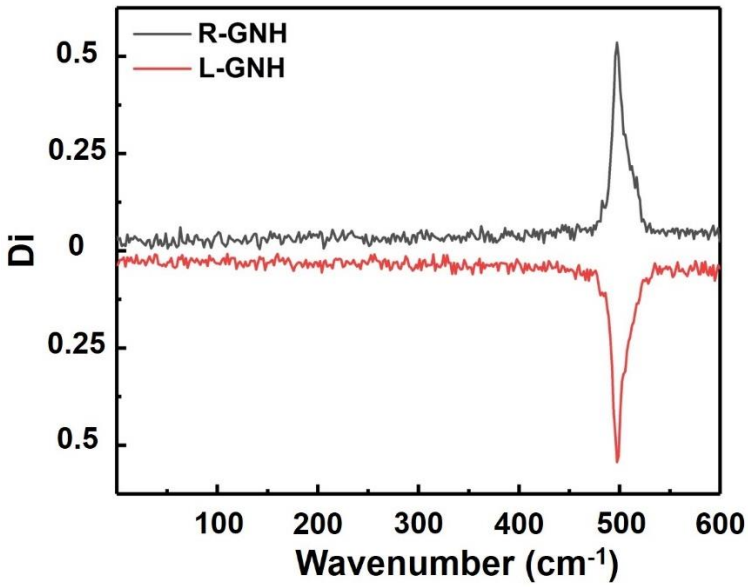

Figure 5.8 The deviation index (Di) curve of L-GNH and R-GNH.

To further confirm the enantioselective effect universality of GNHs on other chiral molecules, we also use L-GNH and R-GNH to recognize L-/D-Trp and L-GSH. As can be seen from Figure 5.9b and c, similar to cysteine results, the peak intensity at 755 cm^{-1} [167, 168] of L-GNH/D-Trp is stronger than that of L-GNH/L-Trp while R-

GNH/L-Trp is stronger than that of L-GNH/D-Trp. The Di value of L-GNH or R-GNH mixtures can be 0.23.

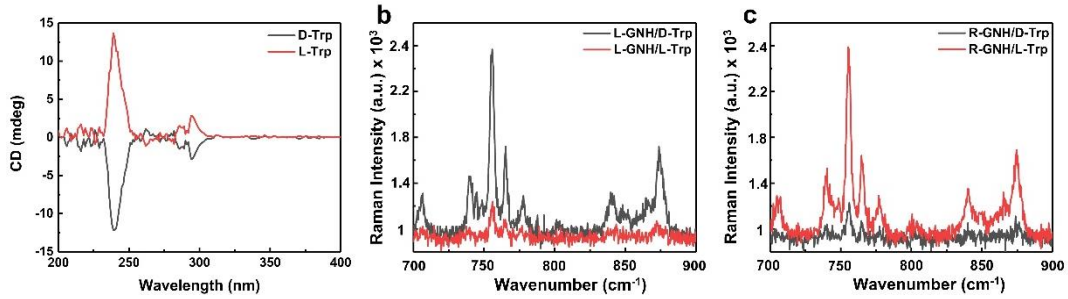

Figure 5.9 (a) CD spectra of 10 mM D-Trp and L-Trp solutions. Raman spectra of (b) L-GNH/ D-Trp and L-GNH/ L-Trp and (c) R-GNH/ D-Trp and R-GNH/ L-Trp at around 755 cm^{-1}.

Figure 5.10 depicts the enantioselective performance of GNHs on discrimination of L-GSH. The Raman peak intensity at 925 cm^{-1} [169] of L-GNH/L-GSH is about 1.7 times stronger than that of R-GNH/L-GSH.

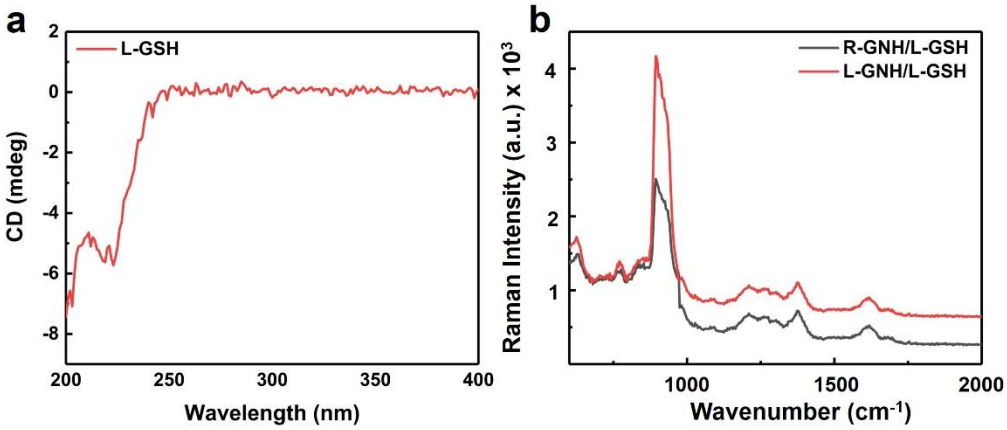

Figure 5.10 (a) CD spectra of 100 μM L-GSH solution. (b) Raman spectra of L-GNH/ L-GSH and R-GNH/ L-GSH at around 927 cm^{-1}.

In summary, the experimental results demonstrated that GNHs can be used for effective enantio-discrimination of chiral molecules by SECRS. The Raman scattering signal intensities tend to be much higher if the GNH-chiral molecules mixture is the

combination of chiral molecules and the GNH with same chiral response. Generally, SERS enhancement for target chiral molecules attached on the gold nanoparticles is nonselective. Here, it can be concluded that the enantioselective phenomenon is mainly similar to the chirality manipulation mechanism as discussed in the Chapter 3 and Chapter 4. In short, GNHs have different absorptivity towards excitation light, and also manipulate the Raman scattering light generated by chiral molecules. Additionally, GNHs also act as a kind of SECRS substrate, which enhances the specific Raman peak of different molecules effectively for their recognition. To clarify, the interaction between the GNH and chiral molecules is the interaction between two chiral objects, different from the situation discussed in previous chapters (interaction between chiral and achiral objects), deep understanding is supposed to be discussed in the future.

5.4 Conclusion

In this chapter, we found that the GNH without the combination of chiral organic molecules could directly be used for amino acid enantio-discrimination by Raman spectroscopy. It is believed that, these experimental results can be crucial to the development of both chiral inorganic nanomaterials and SECRS spectroscopy in multi-aspects: first, making common Raman spectroscopy be a supplementary and efficient tool to probe enantioselective processes, in particular, in the chirality-related in vivo, on-spot and imaging tests; second, offering a deeper understanding of the common SERS mechanism; finally, promoting techniques including spatial, configurational,

and electromagnetic development in chirality involved species analysis.

Chapter 6 Summary and outlook

6.1 Conclusion

Two works have been done on the GNH to thoroughly reveal the chiral light-matter interaction mechanism via the Chiral Purcell effect, and the last work introduced the practical application of GNHs in chiral molecules' recognition. These studies contain the details of GNHs in terms of synthesis, morphology characterization, optical properties (extinction, CD, chiral PL, chiral scatterometry, and chiral Raman), as well as related theory analyzation.

The first work is to study the chiral PL properties of the GNH at the single-particle level. The circular dichroism responses and excitation/emission polarization-resolved PL spectrums of the GNHs are measured; these measurements reveal that the innate chirality is originating from the structural helicity of the GNH, therefore inducing the observed excitation-polarization-correlated chiral PL. Two models are employed to illustrate the obtained circular-polarization-steered effect: (1) a chiral PL phenomenological model quantitatively reproduces the PL dissymmetry characteristics; (2) a chiral Purcell effect model discloses that the super-chiral near fields in the GNHs attribute to the far-field chiral responses such as the polarization-steered chiral PL. This study not only provides crucial comprehension of the physical mechanism account for luminescent chiral plasmonic nanostructures, but also broadens the research on chiral PL-active materials from achiral/chiral hybrid systems to plasmonic

nanostructures with innate geometric chirality, thereby expanding the field of applications in 3D chiral displays and sensing, as well as microstructure analysis.

In the second study, we exploit the spacing, spectral positions, as well as intensity contrast towards circularly polarized illumination of the hybrid localized modes formed by the GNH-FP-based microcavity structure. It is observed that, the Purcell factor of GNHs is improved, and the scattering spectrum has two peaks with narrower linewidth. The intensity contrast of the two peaks towards RCP and LCP white light illumination is the same, which can be analyzed by the reflective nature of FP cavity. Furthermore, the Raman signals of the Si substrate in FP cavity could have chiral features due to the GNH local field modulation. An extended FP model and calculations are used to analyze the single GNH chiral scatterometry and chiral Raman properties of the GNH-FP-based hybrid cavity system.

In the last part of the research, GNHs are used as a kind of SECRS substrate for chiral molecules' recognition. The handedness of chiral molecules is discriminated by the Raman spectroscopy intensity, and the category of the chiral molecules is recognized by specific Raman peak. The application of GNHs in Raman spectroscopy for chiroptical analysis demonstrates that under certain circumstances, the chirality modulation ability of GNHs could substitute the conventional chiroptical measurements method, offering a more feasible and simple chirality detection approach.

6.2 Future perspective

Our research studied the chiral PL properties of GNHs, the chiral related hybrid modes and modulation performance of GNH on a FP cavity, and the application of GNHs in Raman spectroscopy for the chiral molecules' probing. With the further improvement of GNHs chirality performance and deeper understanding of the chiral Purcell effect under various situations, (i) more possibilities to develop more novel nanomaterials will be provided, (ii) interesting physical phenomena could be shown, (iii) more potential practical applications in the field of optoelectronics could be offered. Some research objectives that can be further implemented are listed below:

(1) GNHs-based CPL-active nanomaterials

At present, the study on chiral PL-active micro-/nanoscale materials is still under development. Most of them are mainly realized by co-assembly of achiral luminophores with non-emissive chiral molecules.[170, 171] The PL intensity and efficiency of those micro-/nano-structures are realized by the building blocks and their arrangement. Achiral luminophores assemble based on the structure of chiral objects. During the process of assembly, chiral PL activity of achiral luminophores is acquired from their symmetry breaking. The appearance of GNHs could be a new template for achiral luminophores self-assembly. It is believed that the plasmonic property of GNH could generate chiral PL signals of the system and simultaneously enhance the PL response of the hybrid structure.

(2) Chirality modulation enhancement of GNHs composed microcavity

The current study of gold nanohelicoid modulated chiral scattering/Raman on a SiO_2/Si substrate mainly reveals the chiral modulation properties of GNHs on a FP cavity. The quality of the performances is less concentrated. In the future, to improve the figure-of-merit of the GNH-microcavity hybrid system acquiring stronger optical feedback and modes with high purity, we could substitute SiO_2/Si substrate with a high-quality factor dielectric microcavity.[172] Apart from plasmonic nanostructures on microcavity systems, coupling plasmonic nanostructures could also boost the sensitivity of the hybrid structures.[173] Additionally, a study of a FP cavity formed by a pair of handedness-preserving metasurfaces has been demonstrated to enhance the chiral light and chiral object interaction effectively.[174] Another work using FP cavity as the Raman substrate successfully realized an order of magnitude SERS enhancement from optical interference.[175] In the future, applying GNHs in the microcavity may also be a potential method to boost the sensitivity of chiral objects' detection.

(3) Creating GNH devices in chirality-related detection

The current study on the GNHs in Raman spectroscopy is just in its infancy. In the future, applying a film of GNHs to a substrate to make small, portable, cost effective and integrated devices for species-specific analysis might be an interesting research area.[176] Additionally, how to take advantage of these kinds of devices to promote Raman spectroscopy to become a novel and efficient technique in chirality involved sensing is another problem to be solved in the future.

Appendices

(A) Design of the optical path to realize circularly polarized light excitation

The polarization state of the laser beam is evaluated by degree of polarization (DoP), defined as: $\mathrm{DoP} = \frac{I_{\max} - I_{\min}}{I_{\max} + I_{\min}}$, where $I_{\max}$ ($I_{\min}$) represents the maximum (minimum) intensity of light passing a polarizer. The DoP is 1 for an ideal linear polarization and 0 for an ideal circular polarization. In our experiment, an extinction ratio of 500:1 was measured, corresponding to a DoP of about 0.996, which suggests an excellent linear polarization state.

Conventionally, the linear polarized laser beam can be transformed into a circularly polarized one by passing a quarter-wave plate (QWP). However, some other optical components in subsequent paths could introduce phase or surface reflection differences between the orthogonal polarization components, and thereby modify the beam polarization states. For example, the beam splitter can introduce reflection differences between the S- and P- polarizations, and could transform a circularly polarized beam into an elliptically polarized one. In our case, in the experiment path shown in Figure 3.7, there are two BSs in the optical path, which could influence the circular polarization state of the excitation light and detected signal.

The BSs are BSW10R from Thorlabs Inc., whose reflection profile is shown in Figure A1:

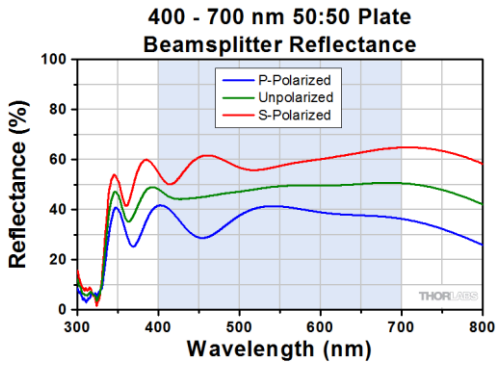

Figure A1 Beam splitter reflectance profile of the BSW10R.

For the region (600 nm-700 nm) we are interested in, the reflectance to P-/S-polarized light has a ratio of around 4:6, which is similar to the actual measured reflection ratio 4:7 using 593.5 nm/ 532 nm laser. To cancel such effect, we intentionally inserted a half-wave plate (HWP) between the BS and the QWP. As depicted in Figure A2, the fast axis angle of QWP is adjusted to generate an elliptically polarized light with short axis (SA): long axis (LA) ~ 4:7. Additionally, the angle of the HWP axis is determined according to the QWP fast axis to match the axes of ellipses to the BS coordinates. As a result, the final polarized light after the BS is perfectly circularly polarized. To confirm the circular polarization state of the beam passing the BS, a power meter and a polarizer was used to measure the output light power. By rotating the polarizer, the largest and smallest intensity of the light could be obtained. Given the optimized QWP and HWP axis orientation angles, the DoP of the RCP and LCP light on the focal plane of objects is about 0.015 and 0.009, respectively; indicating excellent circular polarization states.

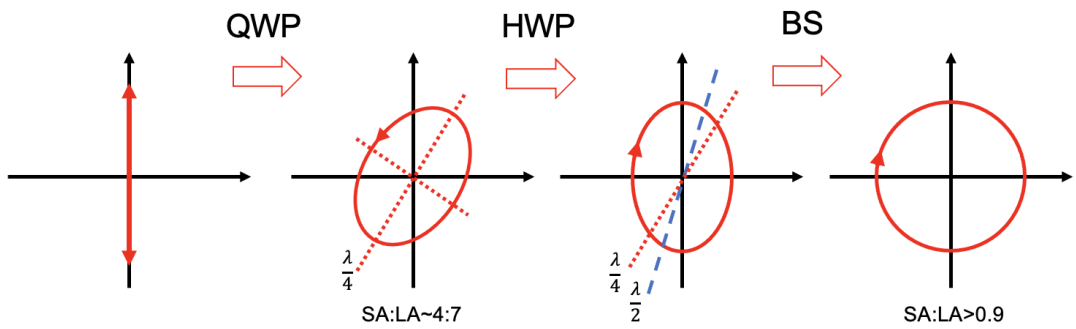

Figure A2 Schematic illustration of circularly polarized light generation with a half-quarter wave-plate combination.

As for the polarization effect of the BS in the detection path when doing the PL resolving, an interesting fact is that the PL signal experiences a transmission factor and a reflection factor through two BSs. Here is the transmission profile of the BSs we used (Figure A3):

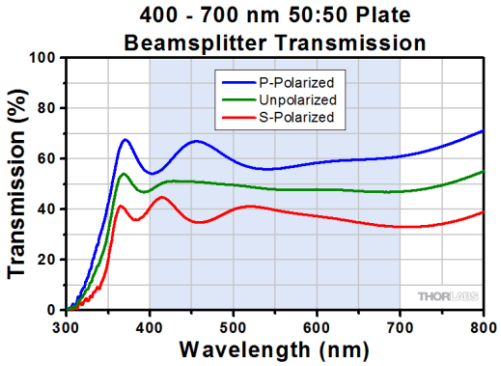

Figure A3 Beam splitter transmission profile of the BSW10R.

A ratio of around 6:4 is seen for P-/S-polarized beam. As a result, a final ratio of around: 6x4:4x6=1:1 is expected based on the alignment of two BSs. Indeed, a ratio of 25:27 has been measured in our actual test. As a result, after QWP, the intensity of right-/left-handed polarized PL can be resolved by an analyser with ±45 degree to fast axis of QWP. A test experiment has shown that, for a circularly polarized light reflected by a mirror at the focal plane of the object, the ratio of resolved intensity at analys-

er ±45 degree can reach 100:1. To make our measurements more accurate, we then normalized the above minor polarization effect caused by the BSs and experimental profile of QWP in the detection path by measuring the intensity ratio of the RCP and LCP light resolved from a linear polarized excitation. A near-unity ratio of 0.9 was obtained and used as calibration in all of the experiments.

(B) ITO substrate influence on gold nanohelicoid chiral photo-luminescence

To demonstrate the ITO substrate with high refractive index, as a homogenous material has no intrinsic chirality to influence the GNH chiral PL performance, we studied the effect of homogeneous background refractive index based on reported work.[177] Red-shift of all features (net optical chirality, $\frac{\overline{C^+}}{C_0}+\frac{\overline{C^-}}{C_0}$, $\frac{|\overline{C^-}|}{U^-}-\frac{|\overline{C^+}|}{U^+}$) can be seen spontaneously with peaks shifting and signs-flipping from about 600 nm to 700 nm (Figure A4) for an effective refractive index of 1.32 compared with an effective refractive index of 1 as shown in previous figures (Figure 3.16a and b). As a result, the critical chirality properties (e.g., sign of parameters, number of sign flip points) of such nanohelicoid-ITO complexes mainly depend on the nanohelicoid itself rather than the ITO substrate. This is consistent with our understanding that homogeneous ITO substrate has no intrinsic chirality. It should be noted that the actual size of nano-helicoids can induce red/blue-shift of spectra as well. Thus, the balance of nanoheli-coids size (120 nm-150 nm) and effective refractive index (1-1.32) can determine the

wavelength of critical points around 600 nm, but the critical curve features are always preserved, which originates from the intrinsic chirality from nanohelicoids.

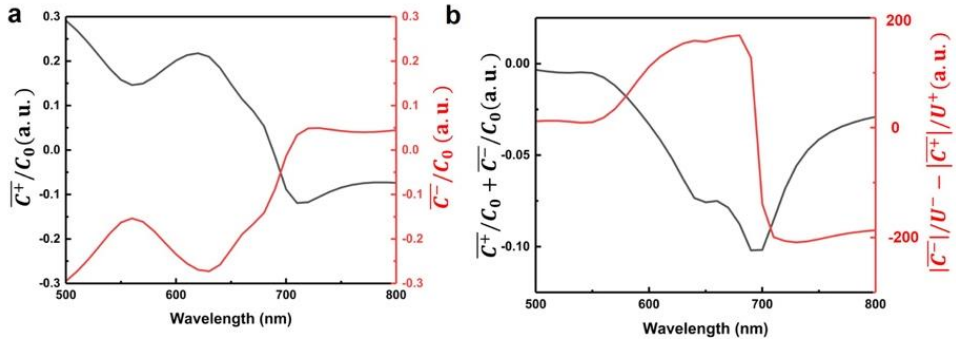

Figure A4 (a) Net optical chirality, $\frac{\overline{C^+}}{C_0} + \frac{\overline{C^-}}{C_0}$, and $\frac{|\overline{C^-}|}{U^-} - \frac{|\overline{C^+}|}{U^+}$ of a 150 nm gold nanohelicoid under a 1.32 effective refractive index. (b) $\frac{\overline{C^+}}{C_0} + \frac{\overline{C^-}}{C_0}$ represents the totality of the integrated optical chirality for GHNs under RCP and LCP excitation with an effective refractive index of 1.32. The non-zero value corresponds to the chiral antenna mode of the GNHs, with the largest dissymmetry factor appearing at about 600 nm. For $\lambda > 600$ nm, the parameter $\frac{|\overline{C^-}|}{U^-} - \frac{|\overline{C^+}|}{U^+}$ is negative, which manifests the polarization-steering effect in polarization-resolved PL.

(C) Geometric handedness dependent chiral photoluminescence

To further understand the impact of morphology on chiral PL signals, the same experiments were done on gold nanohelicoid with another structure (left-handed gold nanohelicoid II, L-GNH II). The synthesis protocol is based on the reported literature.[68] Figure A5a shows the SEM image and the corresponding 3D model of GNH II. Similar to L-GNH in the main context, when excited by RCP light, L-GNH II has a stronger PL signal due to higher absorptivity of RCP light (Figure A6a). GNH II has larger PL intensity contrast towards RCP and LCP light, and the asymmetric chiral PL *g*-factor of GNH II is 0.17 (Figure A7b). This is because the absolute CD value of

GNH II at 593.5 nm is larger than that of previous GNHs (orange points in Figure 2.4c and Figure A5c), which means GNH II has a higher degree of optical chiral response. Similarly, optical chirality of GNH II is obtained as shown in Figure A8. The value C/C_0 of GNH II can be as large as ± 15, which is significantly higher than that of GNH (± 8). This near-field analysis further confirms that the GNH II has a higher degree of optical chiral response, which can also be proved by the differential *g*-factor in Figure A6b and c when the chiral PL signals are depolarized. Figure A8 shows that the super-chirality of the structure in the outer field can be as high as 80, which means the chirality of the structure is extremely strong compared to other planar chiral structures, indicating that GNH II could have better performance than GNH in modulating PL.

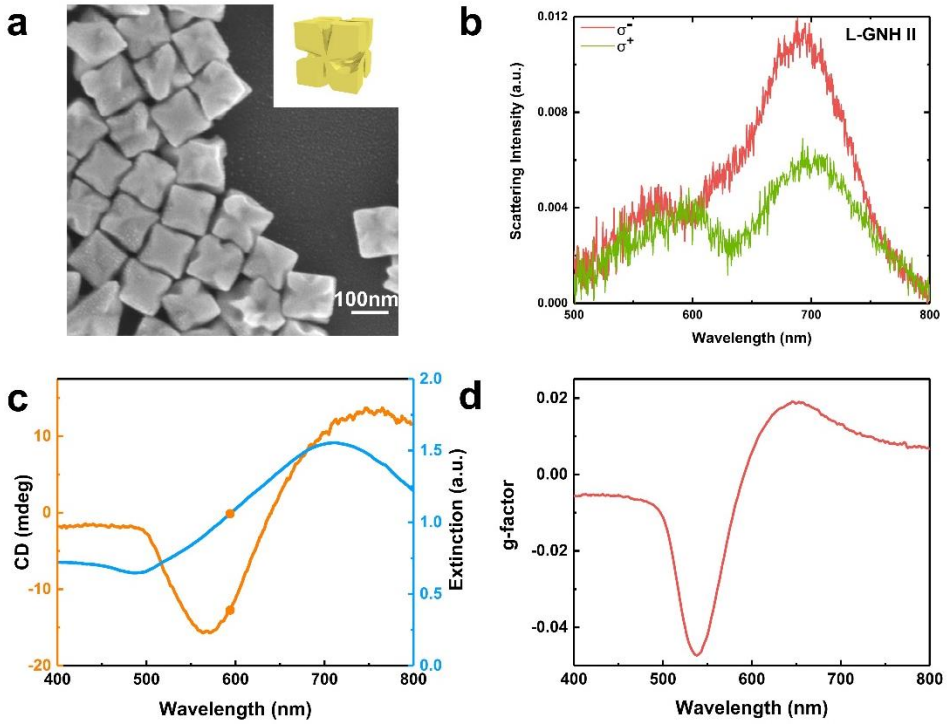

Figure A5 (a) SEM image and 3D model of left-handed gold helicoid II (GNH II). (b) Scattering spectra of left-handed GNH II used for 593.5 nm excitation under RCP (red) and LCP (green) white light illumination. (c) CD (orange) and extinction (blue) spectra of left-handed GNH II in an

aqueous medium. (d) Experimental *g*-factor spectra of left-handed GNH II.

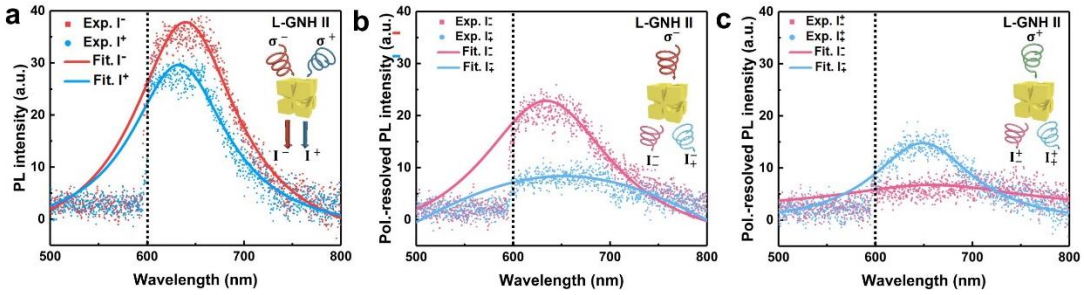

Figure A6 (a) Chiral PL spectra of a left-handed GNH II structure under the illumination of 593.5 nm RCP (red) and LCP (green) laser. (b) Emission polarization-resolved PL spectrum for a left-handed GNH II in (a) under the illumination of 593.5 nm RCP (b) and LCP (c) laser, respectively. The solid line shows the Lorentzian fits of the raw data.

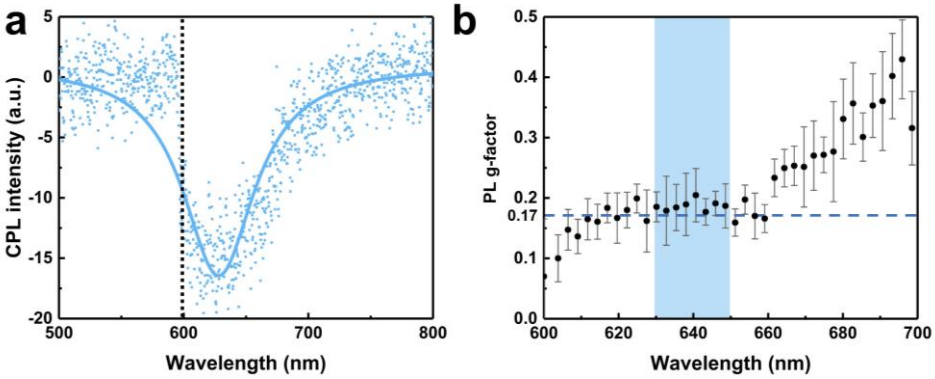

Figure A7 CPL spectrum of left-handed GNH II under 593.5 nm illumination. Dots describe the real CPL signal of GNH II. The solid line shows the Lorentzian fits of the raw data. (b) Experimental chiral PL *g*-factor spectra of left-handed GNH II which has an averaged *g*-factor of ~0.17 at the main peak region (shadowed area). The cliff at 600 nm in each PL spectrum (black dashed line) is due to the cut-off wavelength of the long-pass filter used in the optical path.

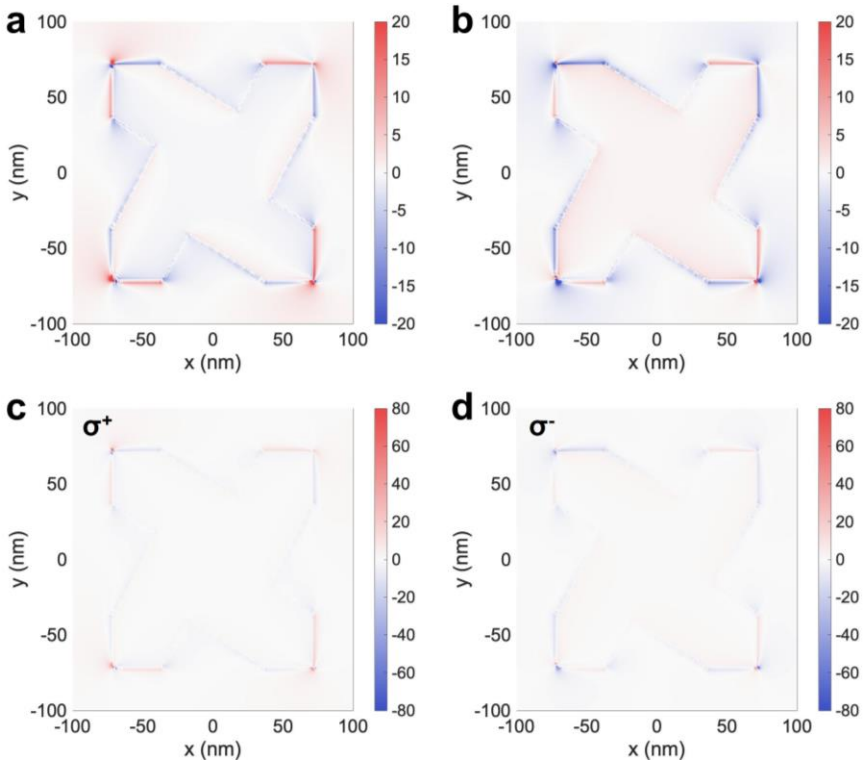

Figure A8 (a-d) Near field optical chirality distribution of right-handed GNH II under LCP (a, c) and RCP excitation (b, d). The colored bar scale of (a) and (b) is modulated to highlight the distribution inside the nanohelicoids. In (c) and (d), an actual optical chirality of 80 can be achieved at the outer corners of the nanostructure.

(D) Gold nanohelicoid modulated chiral Raman scattering on SiO_2/Si substrate with different thicknesses

Chiral scattering and Raman spectra of gold nanohelicoids on SiO_2/Si substrate with different thicknesses were also measured to further verify the influence of FP cavities, and the chiral modulation of the gold nanohelicoid. As shown in Figure A9a and b, under the SiO_2/Si substrate with SiO_2 thicknesses of 100 nm and 300 nm, the scattering spectra of the GNH only has one main peak at 500 nm – 800 nm; no splitting peaks are observed. This might be because the 100 nm and 300 nm thicknesses

are too thin when sandwiched between Si and the GNH to form an effective FP cavity. This hypothesis can be further confirmed by the scattering spectrum of the GNH on SiO_2/Si substrate with 500 nm SiO_2 thickness. As depicted in Figure A9c, though no splitting peaks appear, the main peak has a red shift and the FWHM is smaller than that of the 100 nm and 300 nm situation. The smaller FWHM indicates the increased SiO_2 thickness enhances the effectiveness of the FP cavity. The red shift of the main peak can be attributed to the formed FP cavity. The peak at a shorter wavelength is not obvious because a thickness of 500 nm is still not enough to acquire an effective FP cavity mode.

The chiral Raman Si signals of the SiO_2/Si substrate with gold nanohelicoid modulation are given in Figure A9d to i. Under the same wavelength excitations (593.5/ 532 nm), the dissymmetry factors of the Raman signals g_R are irrelevant to the thickness of the SiO_2. The g_R factors under the 593.5 nm and 532 nm excitations are about 0.20 and 0.14, respectively. The larger g_R factors under the 593.5 nm excitation are consistent with the CD response of GNHs depicted in Figure 2.4c. These results also verified that, GNHs play a major role in chiral Raman modulation procedure when FP cavity mode is not weak.

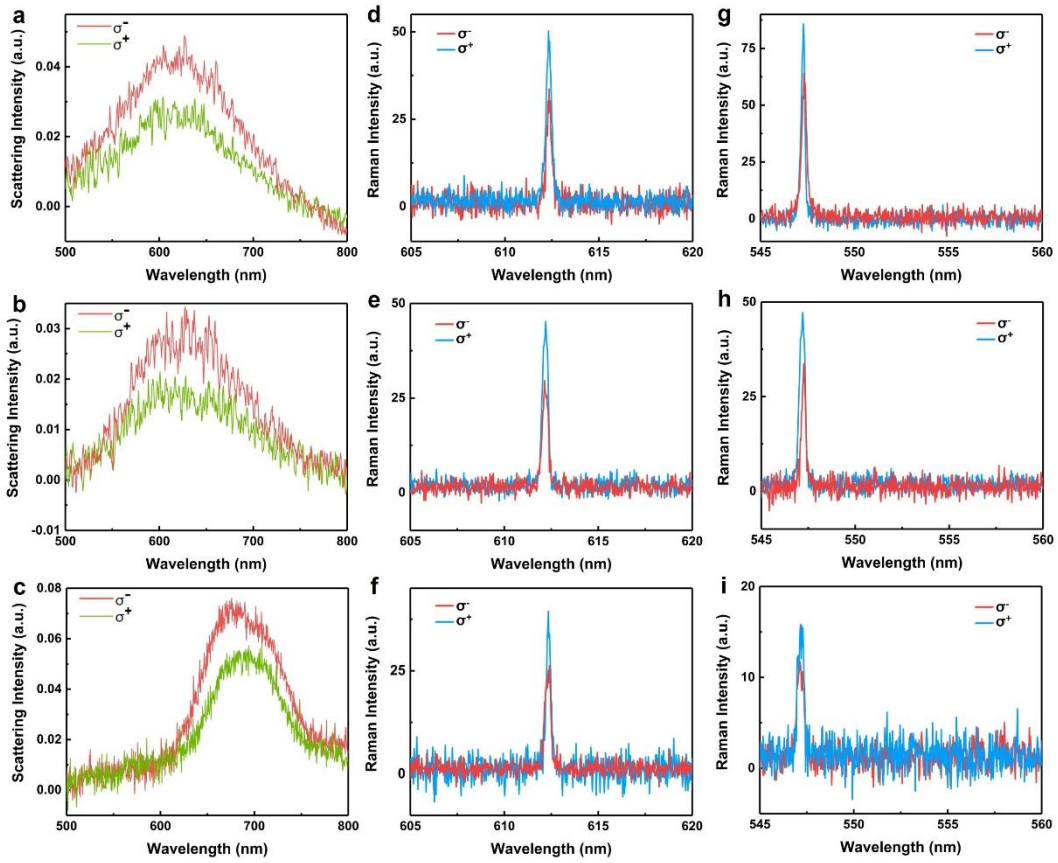

Figure A9 Scattering spectra of a L-GNH on the (a) 100 nm, (b) 300 nm, and (c) 500 nm SiO_2/Si substrate under RCP (σ^-, red) and LCP (σ^+, green) white light illumination. Raman spectra of a single L-GNH on the (d)100 nm, (e) 300 nm, and (f) 500 nm SiO_2/Si substrate under RCP (σ^-, red) and LCP (σ^+, blue) laser excitation at 593.5 nm. (b) Similar results as (d-f) for corresponding same single L-GNH on the (g)100 nm, (h) 300 nm, and (i) 500 nm SiO_2/Si substrate under RCP and LCP laser illumination at 532 nm.

References

1. Weiner, J.; Nunes, F., *Light-matter interaction: physics and engineering at the nanoscale*. Oxford University Press: 2017.
2. Bethe, H. A. J. P. r., Theory of diffraction by small holes. *Phy. Rev.* **1944,** *66* (7-8), 163.
3. Roberts, A. J. J. A., Electromagnetic theory of diffraction by a circular aperture in a thick, perfectly conducting screen. *JOSA A* **1987,** *4* (10), 1970-1983.
4. Fan, J. A.; Wu, C.; Bao, K.; Bao, J.; Bardhan, R.; Halas, N. J.; Manoharan, V. N.; Nordlander, P.; Shvets, G.; Capasso, F. J. s., Self-assembled plasmonic nanoparticle clusters. *Science* **2010,** *328* (5982), 1135-1138.
5. Choy, J. T.; Hausmann, B. J.; Babinec, T. M.; Bulu, I.; Khan, M.; Maletinsky, P.; Yacoby, A.; Lončar, M. J. N. P., Enhanced single-photon emission from a diamond–silver aperture. *Nat. Photon.* **2011,** *5* (12), 738-743.
6. Schumacher, T.; Kratzer, K.; Molnar, D.; Hentschel, M.; Giessen, H.; Lippitz, M. J. N. c., Nanoantenna-enhanced ultrafast nonlinear spectroscopy of a single gold nanoparticle. *Nat. Commun.* **2011,** *2* (1), 1-5.
7. Giannini, V.; Fernández-Domínguez, A. I.; Heck, S. C.; Maier, S. A. J. C. r., Plasmonic nanoantennas: fundamentals and their use in controlling the radiative properties of nanoemitters. *Chem. Rev.* **2011,** *111* (6), 3888-3912.
8. Bouhelier, A.; Bachelot, R.; Lerondel, G.; Kostcheev, S.; Royer, P.; Wiederrecht, G. J. P. r. l., Surface plasmon characteristics of tunable photoluminescence in single gold nanorods. *Phy.Rev.Lett.* **2005,** *95* (26), 267405.
9. Yeshchenko, O. A.; Dmitruk, I. M.; Alexeenko, A. A.; Losytskyy, M. Y.; Kotko, A. V.; Pinchuk, A. O. J. P. R. B., Size-dependent surface-plasmon-enhanced photoluminescence from silver nanoparticles embedded in silica. *Phy. Rev. B* **2009,** *79* (23), 235438.
10. Kneipp, K.; Moskovits, M.; Kneipp, H., *Surface-enhanced Raman scattering: physics and applications*. Springer Science & Business Media: 2006; Vol. 103.
11. Haynes, C. L.; McFarland, A. D.; Van Duyne, R. P., Surface-enhanced Raman spectroscopy. ACS Publications: 2005.
12. Bao, Z. Y.; Zhang, W.; Zhang, Y. L.; He, J.; Dai, J.; Yeung, C. T.; Law, G. L.; Lei, D. Y. J. A. C., Interband absorption enhanced optical activity in discrete Au@ Ag core–shell nanocuboids: probing extended helical conformation of chemisorbed cysteine molecules. *Angew. Chem.* **2017,** *129* (5), 1303-1308.
13. Zhu, Z.; Liu, W.; Li, Z.; Han, B.; Zhou, Y.; Gao, Y.; Tang, Z. J. A. n., Manipulation of collective optical activity in one-dimensional plasmonic assembly. *ACS Nano* **2012,** *6* (3), 2326-2332.
14. Lu, J.; Chang, Y.-X.; Zhang, N.-N.; Wei, Y.; Li, A.-J.; Tai, J.; Xue, Y.; Wang, Z.-Y.; Yang, Y.; Zhao, L. J. A. n., Chiral plasmonic nanochains via the self-assembly of gold nanorods and helical glutathione oligomers facilitated by cetyltrimethylammonium bromide micelles. *ACS Nano* **2017,** *11* (4), 3463-3475.
15. Purcell, E. M.; Torrey, H. C.; Pound, R. V. J. P. r., Resonance absorption by nuclear magnetic

moments in a solid. *Phy. Rev.* **1946,** *69* (1-2), 37.

16. Gérard, J.-M.; Gayral, B. J. J. o. l. t., Strong Purcell effect for InAs quantum boxes in three-dimensional solid-state microcavities. *Light. Technol.* **1999,** *17* (11), 2089-2095.
17. Boroditsky, M.; Vrijen, R.; Coccioli, R.; Bhat, R.; Yablonovitch, E. J. J. o. L. t., Spontaneous emission extraction and Purcell enhancement from thin-film 2-D photonic crystals. *Light. Technol.* **1999,** *17* (11), 2096.
18. Pelton, M. J. N. P., Modified spontaneous emission in nanophotonic structures. *Nat. Photon.* **2015,** *9* (7), 427-435.
19. Agio, M.; Cano, D. M. J. N. p., The Purcell factor of nanoresonators. *Nat. Photon.* **2013,** *7* (9), 674-675.
20. Vučković, J.; Lončar, M.; Mabuchi, H.; Scherer, A. J. P. R. E., Design of photonic crystal microcavities for cavity QED. *Phy. Rev. E* **2001,** *65* (1), 016608.
21. Xiao, Y.-F.; Liu, Y.-C.; Li, B.-B.; Chen, Y.-L.; Li, Y.; Gong, Q. J. P. R. A., Strongly enhanced light-matter interaction in a hybrid photonic-plasmonic resonator. *Phy. Rev. A* **2012,** *85* (3), 031805.
22. De Tommasi, E.; Esposito, E.; Romano, S.; Crescitelli, A.; Di Meo, V.; Mocella, V.; Zito, G.; Rendina, I. J. L. R. d. N. C., Frontiers of light manipulation in natural, metallic, and dielectric nanostructures. *Riv. del Nuovo Cim.* **2021**, 1-68.
23. Raether, H., Surface plasmons on smooth surfaces. In *Surface plasmons on smooth and rough surfaces and on gratings*, Springer: 1988; pp 4-39.
24. Ritchie, R. H. J. P. r., Plasma losses by fast electrons in thin films. *Phy. Rev.* **1957,** *106* (5), 874.
25. Otto, A. J. Z. f. P. A. H.; nuclei, Excitation of nonradiative surface plasma waves in silver by the method of frustrated total reflection. *Physik* **1968,** *216* (4), 398-410.
26. Welford, K. J. O.; Electronics, Q., Surface plasmon-polaritons and their uses. *Opt. Quantum Electron* **1991,** *23* (1), 1-27.
27. Juan, M. L.; Righini, M.; Quidant, R. J. N. p., Plasmon nano-optical tweezers. *Nat. Photon.* **2011,** *5* (6), 349.
28. Li, M.; Cushing, S. K.; Wu, N. J. A., Plasmon-enhanced optical sensors: a review. *Analyst* **2015,** *140* (2), 386-406.
29. Berini, P.; De Leon, I. J. N. p., Surface plasmon–polariton amplifiers and lasers. *Nat. Photon.* **2012,** *6* (1), 16-24.
30. Kim, S.; Jin, J.; Kim, Y.-J.; Park, I.-Y.; Kim, Y.; Kim, S.-W. J. N., High-harmonic generation by resonant plasmon field enhancement. *Nature* **2008,** *453* (7196), 757-760.
31. Klein, M. W.; Enkrich, C.; Wegener, M.; Linden, S. J. S., Second-harmonic generation from magnetic metamaterials. *Science* **2006,** *313* (5786), 502-504.
32. Schietinger, S.; Aichele, T.; Wang, H.-Q.; Nann, T.; Benson, O. J. N. l., Plasmon-enhanced upconversion in single NaYF4: Yb3+/Er3+ codoped nanocrystals. *Nano Lett* **2010,** *10* (1), 134-138.
33. Prodan, E.; Radloff, C.; Halas, N. J.; Nordlander, P. J. s., A hybridization model for the plasmon response of complex nanostructures. *Science* **2003,** *302* (5644), 419-422.
34. Scholl, J. A.; Koh, A. L.; Dionne, J. A. J. N., Quantum plasmon resonances of individual metallic nanoparticles. *Nature* **2012,** *483* (7390), 421-427.
35. Hentschel, M.; Schäferling, M.; Duan, X.; Giessen, H.; Liu, N. J. S. a., Chiral plasmonics. *Sci.*

Adv. **2017,** *3* (5), e1602735.

36. Schellman, J. A. J. C. R., Circular dichroism and optical rotation. *Chem. Rev.* **1975,** *75* (3), 323-331.
37. Yoo, S. J. S., Korea, Korea University. Chiral light-matter interaction in metamaterials. Korea University, 2015.
38. Hu, Z.; Meng, D.; Lin, F.; Zhu, X.; Fang, Z.; Wu, X. J. A. O. M., Plasmonic circular dichroism of gold nanoparticle based nanostructures. *Adv. Opt. Mater.* **2019,** *7* (10), 1801590.
39. Yoo, S.; Park, Q.-H. J. N., Metamaterials and chiral sensing: a review of fundamentals and applications. *Nanophotonics* **2019,** *8* (2), 249-261.
40. Wen, Y.; Li, Z.; Jiang, J. J. C. C. L., Delving noble metal and semiconductor nanomaterials into enantioselective analysis. *Chin. Chem. Lett.* **2019,** *30* (9), 1565-1574.
41. Solomon, M. L.; Saleh, A. A.; Poulikakos, L. V.; Abendroth, J. M.; Tadesse, L. F.; Dionne, J. A. J. A. o. c. r., Nanophotonic platforms for chiral sensing and separation. *Acc. Chem. Res.* **2020,** *53* (3), 588-598.
42. Kumar, J.; Liz-Marzán, L. M. J. B. o. t. C. S. o. J., Recent advances in chiral plasmonics—towards biomedical applications. *Bull. Chem. Soc. Jpn.* **2019,** *92* (1), 30-37.
43. Cao, Z.; Gao, H.; Qiu, M.; Jin, W.; Deng, S.; Wong, K. Y.; Lei, D. J. A. M., Chirality Transfer from Sub-Nanometer Biochemical Molecules to Sub-Micrometer Plasmonic Metastructures: Physiochemical Mechanisms, Biosensing, and Bioimaging Opportunities. *Adv. Mater.* **2020,** *32* (41), 1907151.
44. Slocik, J. M.; Govorov, A. O.; Naik, R. R. J. N. l., Plasmonic circular dichroism of peptide-functionalized gold nanoparticles. *Nano Lett* **2011,** *11* (2), 701-705.
45. Govorov, A. O.; Fan, Z.; Hernandez, P.; Slocik, J. M.; Naik, R. R. J. N. l., Theory of circular dichroism of nanomaterials comprising chiral molecules and nanocrystals: plasmon enhancement, dipole interactions, and dielectric effects. *Nano Lett* **2010,** *10* (4), 1374-1382.
46. Wu, X.; Xu, L.; Ma, W.; Liu, L.; Kuang, H.; Yan, W.; Wang, L.; Xu, C. J. A. F. M., Gold core-DNA-silver shell nanoparticles with intense plasmonic chiroptical activities. *Adv. Funct. Mater.* **2015,** *25* (6), 850-854.
47. Zhu, F.; Li, X.; Li, Y.; Yan, M.; Liu, S. J. A. c., Enantioselective circular dichroism sensing of cysteine and glutathione with gold nanorods. *Anal. Chem.* **2015,** *87* (1), 357-361.
48. Wang, R.-Y.; Wang, P.; Liu, Y.; Zhao, W.; Zhai, D.; Hong, X.; Ji, Y.; Wu, X.; Wang, F.; Zhang, D. J. T. J. o. P. C. C., Experimental observation of giant chiroptical amplification of small chiral molecules by gold nanosphere clusters. *J. Phys. Chem. C* **2014,** *118* (18), 9690-9695.
49. Ma, W.; Kuang, H.; Xu, L.; Ding, L.; Xu, C.; Wang, L.; Kotov, N. A. J. N. c., Attomolar DNA detection with chiral nanorod assemblies. *Nat. Commun.* **2013,** *4* (1), 1-8.
50. Sun, M.; Xu, L.; Bahng, J. H.; Kuang, H.; Alben, S.; Kotov, N. A.; Xu, C. J. N. c., Intracellular localization of nanoparticle dimers by chirality reversal. *Nat. Commun.* **2017,** *8* (1), 1-10.
51. Wu, X.; Xu, L.; Liu, L.; Ma, W.; Yin, H.; Kuang, H.; Wang, L.; Xu, C.; Kotov, N. A. J. J. o. t. A. C. S., Unexpected chirality of nanoparticle dimers and ultrasensitive chiroplasmonic bioanalysis. *J. Am. Chem. Soc.* **2013,** *135* (49), 18629-18636.
52. Gao, F.; Sun, M.; Ma, W.; Wu, X.; Liu, L.; Kuang, H.; Xu, C. J. A. M., A Singlet Oxygen Generating Agent by Chirality-dependent Plasmonic Shell-Satellite Nanoassembly. *Adv.Mater.* **2017,** *29* (18), 1606864.
53. Li, S.; Xu, L.; Ma, W.; Wu, X.; Sun, M.; Kuang, H.; Wang, L.; Kotov, N. A.; Xu, C. J. J. o. t.

A. C. S., Dual-mode ultrasensitive quantification of microRNA in living cells by chiroplasmonic nanopyramids self-assembled from gold and upconversion nanoparticles. *J. Am. Chem. Soc.* **2016,** *138* (1), 306-312.

54. Sun, M.; Qu, A.; Hao, C.; Wu, X.; Xu, L.; Xu, C.; Kuang, H. J. A. M., Chiral Upconversion Heterodimers for Quantitative Analysis and Bioimaging of Antibiotic-Resistant Bacteria In Vivo. *Adv.Mater.* **2018,** *30* (50), 1804241.
55. Kuzyk, A.; Schreiber, R.; Zhang, H.; Govorov, A. O.; Liedl, T.; Liu, N. J. N. m., Reconfigurable 3D plasmonic metamolecules. *Nat. Mater.* **2014,** *13* (9), 862-866.
56. Schreiber, R.; Luong, N.; Fan, Z.; Kuzyk, A.; Nickels, P. C.; Zhang, T.; Smith, D. M.; Yurke, B.; Kuang, W.; Govorov, A. O. J. N. c., Chiral plasmonic DNA nanostructures with switchable circular dichroism. *Nat. Commun.* **2013,** *4* (1), 1-6.
57. Gansel, J. K.; Thiel, M.; Rill, M. S.; Decker, M.; Bade, K.; Saile, V.; von Freymann, G.; Linden, S.; Wegener, M. J. S., Gold helix photonic metamaterial as broadband circular polarizer. *Science* **2009,** *325* (5947), 1513-1515.
58. Smith, K. W.; McCarthy, L. A.; Alabastri, A.; Bursi, L.; Chang, W.-S.; Nordlander, P.; Link, S. J. A. n., Exploiting evanescent field polarization for giant chiroptical modulation from achiral gold half-rings. *ACS Nano* **2018,** *12* (11), 11657-11663.
59. Zhao, Y.; Belkin, M.; Alù, A. J. N. c., Twisted optical metamaterials for planarized ultrathin broadband circular polarizers. *Nat. Commun.* **2012,** *3* (1), 1-7.
60. Qiu, M.; Zhang, L.; Tang, Z.; Jin, W.; Qiu, C. W.; Lei, D. Y. J. A. F. M., 3D metaphotonic nanostructures with intrinsic chirality. *Adv. Funct. Mater.* **2018,** *28* (45), 1803147.
61. Decker, M.; Ruther, M.; Kriegler, C.; Zhou, J.; Soukoulis, C.; Linden, S.; Wegener, M. J. O. l., Strong optical activity from twisted-cross photonic metamaterials. *Opt. Lett.* **2009,** *34* (16), 2501-2503.
62. Decker, M.; Zhao, R.; Soukoulis, C.; Linden, S.; Wegener, M. J. O. l., Twisted split-ring-resonator photonic metamaterial with huge optical activity. *Opt. Lett.* **2010,** *35* (10), 1593-1595.
63. Kaschke, J.; Wegener, M. J. O. l., Gold triple-helix mid-infrared metamaterial by STED-inspired laser lithography. *Opt. Lett.* **2015,** *40* (17), 3986-3989.
64. Kuzyk, A.; Schreiber, R.; Fan, Z.; Pardatscher, G.; Roller, E.-M.; Högele, A.; Simmel, F. C.; Govorov, A. O.; Liedl, T. J. N., DNA-based self-assembly of chiral plasmonic nanostructures with tailored optical response. *Nature* **2012,** *483* (7389), 311-314.
65. Shen, X.; Asenjo-Garcia, A.; Liu, Q.; Jiang, Q.; García de Abajo, F. J.; Liu, N.; Ding, B. J. N. l., Three-dimensional plasmonic chiral tetramers assembled by DNA origami. *Nano Lett* **2013,** *13* (5), 2128-2133.
66. Wang, R.-Y.; Wang, H.; Wu, X.; Ji, Y.; Wang, P.; Qu, Y.; Chung, T.-S. J. S. M., Chiral assembly of gold nanorods with collective plasmonic circular dichroism response. *Nano Lett* **2011,** *7* (18), 8370-8375.
67. Fu, X.; Wang, Y.; Huang, L.; Sha, Y.; Gui, L.; Lai, L.; Tang, Y. J. A. M., Assemblies of metal nanoparticles and Self-Assembled peptide Fibrils—Formation of double helical and Single-Chain arrays of metal nanoparticles. *Adv.Mater.* **2003,** *15* (11), 902-906.
68. Lee, H.-E.; Ahn, H.-Y.; Mun, J.; Lee, Y. Y.; Kim, M.; Cho, N. H.; Chang, K.; Kim, W. S.; Rho, J.; Nam, K. T. J. N., Amino-acid-and peptide-directed synthesis of chiral plasmonic gold nanoparticles. *Nature* **2018,** *556* (7701), 360-365.

69. Lee, H.-E.; Kim, R. M.; Ahn, H.-Y.; Lee, Y. Y.; Byun, G. H.; Im, S. W.; Mun, J.; Rho, J.; Nam, K. T. J. N. c., Cysteine-encoded chirality evolution in plasmonic rhombic dodecahedral gold nanoparticles. *Nat. Commun.* **2020,** *11* (1), 1-10.

70. Kim, H.; Im, S. W.; Cho, N. H.; Seo, D. H.; Kim, R. M.; Lim, Y. C.; Lee, H. E.; Ahn, H. Y.; Nam, K. T. J. A. C., γ-Glutamylcysteine-and Cysteinylglycine-Directed Growth of Chiral Gold Nanoparticles and their Crystallographic Analysis. *Angew. Chem.* **2020,** *132* (31), 13076-13083.

71. Im, S. W.; Ahn, H. Y.; Kim, R. M.; Cho, N. H.; Kim, H.; Lim, Y. C.; Lee, H. E.; Nam, K. T. J. A. M., Chiral surface and geometry of metal nanocrystals. *Adv. Mater.* **2020,** *32* (41), 1905758.

72. Cho, N. H.; Byun, G. H.; Lim, Y.-C.; Im, S. W.; Kim, H.; Lee, H.-E.; Ahn, H.-Y.; Nam, K. T. J. A. n., Uniform chiral gap synthesis for high dissymmetry factor in single plasmonic gold nanoparticle. *ACS Nano* **2020,** *14* (3), 3595-3602.

73. Ahn, H.-Y.; Lee, H.-E.; Jin, K.; Nam, K. T. J. J. o. M. C. C., Extended gold nano-morphology diagram: synthesis of rhombic dodecahedra using CTAB and ascorbic acid. *J. Mater. Chem. C* **2013,** *1* (41), 6861-6868.

74. Mooradian, A. J. P. R. L., Photoluminescence of metals. *Phys. Rev. Lett.* **1969,** *22* (5), 185.

75. Boyd, G.; Yu, Z.; Shen, Y. J. P. R. B., Photoinduced luminescence from the noble metals and its enhancement on roughened surfaces. *Phy. Rev. B* **1986,** *33* (12), 7923.

76. Hu, H.; Duan, H.; Yang, J. K.; Shen, Z. X. J. A. N., Plasmon-modulated photoluminescence of individual gold nanostructures. *ACS Nano* **2012,** *6* (11), 10147-10155.

77. Zhang, W.; Cheng, Y.; Zhao, J.; Wen, T.; Hu, A.; Gong, Q.; Lu, G. J. T. J. o. P. C. C., Photoluminescence Quantum Yield from Gold Nanorods: Dependence on Excitation Polarization. *J. Phys. Chem. C* **2019,** *123* (14), 9358-9363.

78. Rao, W.; Li, Q.; Wang, Y.; Li, T.; Wu, L. J. A. N., Comparison of photoluminescence quantum yield of single gold nanobipyramids and gold nanorods. *ACS Nano* **2015,** *9* (3), 2783-2791.

79. Lumdee, C.; Yun, B.; Kik, P. G., Gap-Plasmon Enhanced Gold Nanoparticle Photoluminescence. *ACS Photonics* **2014,** *1* (11), 1224-1230.

80. Tittl, A.; Yin, X.; Giessen, H.; Tian, X.-D.; Tian, Z.-Q.; Kremers, C.; Chigrin, D. N.; Liu, N. J. N. l., Plasmonic smart dust for probing local chemical reactions. *Nano Lett* **2013,** *13* (4), 1816-1821.

81. Lumdee, C.; Yun, B.; Kik, P. G. J. A. P., Gap-plasmon enhanced gold nanoparticle photoluminescence. *ACS Photonics* **2014,** *1* (11), 1224-1230.

82. Li, G.-C.; Zhang, Y.-L.; Jiang, J.; Luo, Y.; Lei, D. Y. J. A. n., Metal-substrate-mediated plasmon hybridization in a nanoparticle dimer for photoluminescence line-width shrinking and intensity enhancement. *ACS Nano* **2017,** *11* (3), 3067-3080.

83. Riehl, J. P.; Richardson, F. S. J. C. R., Circularly polarized luminescence spectroscopy. *Chem. Rev.* **1986,** *86* (1), 1-16.

84. Sang, Y.; Han, J.; Zhao, T.; Duan, P.; Liu, M. J. A. M., Circularly polarized luminescence in nanoassemblies: generation, amplification, and application. *Adv.Mater.* **2020,** *32* (41), 1900110.

85. Yang, D.; Han, J.; Liu, M.; Duan, P. J. A. M., Photon upconverted circularly polarized luminescence via triplet–triplet annihilation. *Adv.Mater.* **2019,** *31* (45), 1805683.

86. Kim, Y.; Yeom, B.; Arteaga, O.; Yoo, S. J.; Lee, S.-G.; Kim, J.-G.; Kotov, N. A. J. N. m.,

Reconfigurable chiroptical nanocomposites with chirality transfer from the macro-to the nanoscale. *Nat. Mater.* **2016,** *15* (4), 461-468.

87. Hayasaka, H.; Miyashita, T.; Tamura, K.; Akagi, K. J. A. F. M., Helically π-stacked conjugated polymers bearing photoresponsive and chiral moieties in side chains: reversible photoisomerization-enforced switching between emission and quenching of circularly polarized fluorescence. *Adv. Funct. Mater.* **2010,** *20* (8), 1243-1250.
88. Chen, S.; Katsis, D.; Schmid, A.; Mastrangelo, J.; Tsutsui, T.; Blanton, T. J. N., Circularly polarized light generated by photoexcitation of luminophores in glassy liquid-crystal films. *Nature* **1999,** *397* (6719), 506-508.
89. Furumi, S. J. P. j., Self-assembled organic and polymer photonic crystals for laser applications. *Polym. J* **2013,** *45* (6), 579-593.
90. Harada, T.; Kuroda, R.; Moriyama, H. J. C. P. L., Solid-state circularly polarized luminescence measurements: Theoretical analysis. *Chem.Phys.Lett.* **2012,** *530*, 126-131.
91. Harada, T. J. P. J., Application of a polarized modulation technique in supramolecular science: chiroptical measurements of optically anisotropic systems. *Polym. J* **2018,** *50* (8), 679-687.
92. Harada, T.; Hayakawa, H.; Watanabe, M.; Takamoto, M. J. R. o. S. I., A solid-state dedicated circularly polarized luminescence spectrophotometer: Development and application. *Rev. Sci. Instrum.* **2016,** *87* (7), 075102.
93. Huang, D.; Byers, C. P.; Wang, L.-Y.; Hoggard, A.; Hoener, B.; Dominguez-Medina, S.; Chen, S.; Chang, W.-S.; Landes, C. F.; Link, S. J. A. n., Photoluminescence of a plasmonic molecule. *ACS Nano* **2015,** *9* (7), 7072-7079.
94. Andersen, S. K.; Pors, A.; Bozhevolnyi, S. I. J. A. P., Gold photoluminescence wavelength and polarization engineering. *ACS Photonics* **2015,** *2* (3), 432-438.
95. Yin, T.; Jiang, L.; Shen, Z. J. C. P. B., Recent Progress on Photoluminescence from Plasmonic Nanostructures: Phenomenon, Mechanism, and Application. *Chin.Phys.B* **2018,** *27* (9), 097803.
96. Yin, T.; Jiang, L.; Dong, Z.; Yang, J. K.; Shen, Z. X. J. N., Energy transfer and depolarization in the photoluminescence of a plasmonic molecule. *Nanoscale* **2017,** *9* (5), 2082-2087.
97. Jiang, L.; Yin, T.; Dong, Z.; Hu, H.; Liao, M.; Allioux, D.; Tan, S. J.; Goh, X. M.; Li, X.; Yang, J. K. J. A. P., Probing vertical and horizontal plasmonic resonant states in the photoluminescence of gold nanodisks. *ACS Photonics* **2015,** *2* (8), 1217-1223.
98. Beversluis, M. R.; Bouhelier, A.; Novotny, L. J. P. R. B., Continuum generation from single gold nanostructures through near-field mediated intraband transitions. *Phys. Rev. B* **2003,** *68* (11), 115433.
99. Viarbitskaya, S.; Teulle, A.; Marty, R.; Sharma, J.; Girard, C.; Arbouet, A.; Dujardin, E. J. N. m., Tailoring and imaging the plasmonic local density of states in crystalline nanoprisms. *Nat. Mater.* **2013,** *12* (5), 426-432.
100. Tang, Y.; Cohen, A. E. J. S., Enhanced enantioselectivity in excitation of chiral molecules by superchiral light. *Science* **2011,** *332* (6027), 333-336.
101. Hendry, E.; Carpy, T.; Johnston, J.; Popland, M.; Mikhaylovskiy, R.; Lapthorn, A.; Kelly, S.; Barron, L.; Gadegaard, N.; Kadodwala, M. J. N. n., Ultrasensitive detection and characterization of biomolecules using superchiral fields. *Nat. Nanotechnol.* **2010,** *5* (11), 783-787.
102. Yoo, S.; Park, Q.-H. J. P. r. l., Chiral light-matter interaction in optical resonators. *Phy. Rev.*

Lett. **2015,** *114* (20), 203003.

103. Wu, Z.; Li, J.; Zhang, X.; Redwing, J. M.; Zheng, Y. J. A. M., Room-temperature active modulation of valley dynamics in a monolayer semiconductor through chiral Purcell effects. *Adv.Mater.* **2019,** *31* (49), 1904132.
104. Poulikakos, L. V.; Thureja, P.; Stollmann, A.; De Leo, E.; Norris, D. J. J. N. l., Chiral light design and detection inspired by optical antenna theory. *Nano Lett* **2018,** *18* (8), 4633-4640.
105. Tang, Y.; Cohen, A. E. J. P. r. l., Optical chirality and its interaction with matter. *Phy. Rev. Lett.* **2010,** *104* (16), 163901.
106. Wang, Z.; Wang, Y.; Adamo, G.; Teng, J.; Sun, H. J. L.; Reviews, P., Induced optical chirality and circularly polarized emission from achiral CdSe/ZnS quantum dots via resonantly coupling with plasmonic chiral metasurfaces. *Laser & Photonics Rev.* **2019,** *13* (3), 1800276.
107. Du, W.; Wen, X.; Gérard, D.; Qiu, C.-W.; Xiong, Q. J. S. C. P., Mechanics; Astronomy, Chiral plasmonics and enhanced chiral light-matter interactions. *SCIENCE CHINA Physics, Mechanics, Astronomy*

2020, *63* (4), 1-11.

108. Meinzer, N.; Hendry, E.; Barnes, W. L. J. P. R. B., Probing the chiral nature of electromagnetic fields surrounding plasmonic nanostructures. *Phy. Rev. B* **2013,** *88* (4), 041407.
109. Karst, J.; Cho, N. H.; Kim, H.; Lee, H.-E.; Nam, K. T.; Giessen, H.; Hentschel, M. J. A. n., Chiral scatterometry on chemically synthesized single plasmonic nanoparticles. *ACS Nano* **2019,** *13* (8), 8659-8668.
110. Ohnoutek, L.; Cho, N. H.; Allen Murphy, A. W.; Kim, H.; Răsădean, D. M.; Pantoş, G. D.; Nam, K. T.; Valev, V. K. J. N. l., Single nanoparticle chiroptics in a liquid: optical activity in hyper-Rayleigh scattering from Au helicoids. *Nano Lett* **2020,** *20* (8), 5792-5798.
111. Rafiei Miandashti, A.; Khosravi Khorashad, L.; Kordesch, M. E.; Govorov, A. O.; Richardson, H. H. J. A. n., Experimental and Theoretical Observation of Photothermal Chirality in Gold Nanoparticle Helicoids. *ACS Nano* **2020,** *14* (4), 4188-4195.
112. Kim, S.; Lim, Y. C.; Kim, R. M.; Fröch, J. E.; Tran, T. N.; Nam, K. T.; Aharonovich, I. J. S., A single chiral nanoparticle induced valley polarization enhancement. *Small* **2020,** *16* (37), 2003005.
113. Ismail, N.; Kores, C. C.; Geskus, D.; Pollnau, M. J. O. e., Fabry-Pérot resonator: spectral line shapes, generic and related Airy distributions, linewidths, finesses, and performance at low or frequency-dependent reflectivity. *Opt. Express* **2016,** *24* (15), 16366-16389.
114. Saleh, B. E.; Teich, M. C., *Fundamentals of photonics*. john Wiley & sons: 2019.
115. Bitarafan, M. H.; DeCorby, R. G. J. S., On-chip high-finesse Fabry-Perot microcavities for optical sensing and quantum information. *Sensors* **2017,** *17* (8), 1748.
116. Xie, W.; Schlücker, S. J. C. C., Surface-enhanced Raman spectroscopic detection of molecular chemo-and plasmo-catalysis on noble metal nanoparticles. *Chem. Comm.* **2018,** *54* (19), 2326-2336.
117. Panoiu, N. C.; Sha, W.; Lei, D.; Li, G. J. J. o. O., Nonlinear optics in plasmonic nanostructures. *J Opt.* **2018,** *20* (8), 083001.
118. Doria, G.; Conde, J.; Veigas, B.; Giestas, L.; Almeida, C.; Assunção, M.; Rosa, J.; Baptista, P. V. J. S., Noble metal nanoparticles for biosensing applications. *Sensors* **2012,** *12* (2), 1657-1687.
119. Wang, D.; Bourgeois, M. R.; Lee, W.-K.; Li, R.; Trivedi, D.; Knudson, M. P.; Wang, W.;

Schatz, G. C.; Odom, T. W. J. N. l., Stretchable nanolasing from hybrid quadrupole plasmons. *Nano Lett* **2018,** *18* (7), 4549-4555.

120. Schmidt, M. A.; Lei, D. Y.; Wondraczek, L.; Nazabal, V.; Maier, S. A. J. N. c., Hybrid nanoparticle–microcavity-based plasmonic nanosensors with improved detection resolution and extended remote-sensing ability. *Nat. Commun.* **2012,** *3* (1), 1-8.
121. Adato, R.; Yanik, A. A.; Amsden, J. J.; Kaplan, D. L.; Omenetto, F. G.; Hong, M. K.; Erramilli, S.; Altug, H. J. P. o. t. N. A. o. S., Ultra-sensitive vibrational spectroscopy of protein monolayers with plasmonic nanoantenna arrays. *Proc. Natl. Acad. Sci. U. S. A.* **2009,** *106* (46), 19227-19232.
122. Alu, A.; Engheta, N. J. N. p., Tuning the scattering response of optical nanoantennas with nanocircuit loads. *Nat. Photon.* **2008,** *2* (5), 307-310.
123. Yang, X.; Ishikawa, A.; Yin, X.; Zhang, X. J. A. n., Hybrid photonic− Plasmonic crystal nanocavities. *ACS Nano* **2011,** *5* (4), 2831-2838.
124. Ameling, R.; Giessen, H. J. N. l., Cavity plasmonics: large normal mode splitting of electric and magnetic particle plasmons induced by a photonic microcavity. *Nano Lett* **2010,** *10* (11), 4394-4398.
125. Abhilash, T.; Balasubrahmaniyam, M.; Patra, A.; Kasiviswanathan, S. J. A. p. l., Plasmon resonance mediated enhancement in Fabry-Perot cavity modes. *Appl. Phys. Lett.* **2014,** *104* (24), 241112.
126. Chu, G.; Yin, H.; Jiang, H.; Qu, D.; Shi, Y.; Ding, D.; Xu, Y. J. T. J. o. P. C. C., Ultrafast optical modulation of rationally engineered photonic–plasmonic coupling in self-assembled nanocrystalline cellulose/silver hybrid material. *J. Phys. Chem. C* **2016,** *120* (48), 27541-27547.
127. Polemi, A.; Shuford, K. L. J. J. o. N., Sensing properties of a Fabry-Perot dielectric structure and dimer nanoparticles. *Nanotechnology* **2012,** *2012*.
128. Alessia, P.; Kevin, L. S., Fabry–Perot effect on dimer nanoantennas. *Photonics and Nanostructures - Fundamentals and Applications* **2012,** *10* (1), 36-45.
129. Zhang, S.; Panikkanvalappil, S. R.; Kang, S.; Smith, M. J.; Yu, S.; El-Sayed, M.; Tsukruk, V. V. J. T. J. o. P. C. C., Enhancing Plasmonic–Photonic Hybrid Cavity Modes by Coupling of Individual Plasmonic Nanoparticles. *J. Phys. Chem. C* **2019,** *123* (39), 24255-24262.
130. Bliokh, K. Y.; Nori, F. J. P. R. A., Characterizing optical chirality. *Phy. Rev. A* **2011,** *83* (2), 021803.
131. Kristensen, P. T.; Van Vlack, C.; Hughes, S. J. O. l., Generalized effective mode volume for leaky optical cavities. *Opt. Lett.* **2012,** *37* (10), 1649-1651.
132. Yao, P.; Manga Rao, V.; Hughes, S. J. L.; Reviews, P., On-chip single photon sources using planar photonic crystals and single quantum dots. *Laser & Photonics Rev.* **2010,** *4* (4), 499-516.
133. Wang, B.; Yu, P.; Wang, W.; Zhang, X.; Kuo, H. C.; Xu, H.; Wang, Z. M. J. A. O. M., High-Q Plasmonic Resonances: Fundamentals and Applications. *Adv. Opt. Mater.* **2021,** *9* (7), 2001520.
134. Placzek, G., *The rayleigh and raman scattering*. Lawrence Radiation Laboratory: 1959; Vol. 526.
135. Jacob, L. J.; Deigner, H.-P., Nanoparticles and nanosized structures in diagnostics and therapy. In *Precision Medicine*, Elsevier: 2018; pp 229-252.

136. Jones, R. R.; Hooper, D. C.; Zhang, L.; Wolverson, D.; Valev, V. K. J. N. r. l., Raman techniques: Fundamentals and frontiers. **2019,** *14* (1), 1-34.

137. Fleischmann, M.; Hendra, P. J.; McQuillan, A. J. J. C. p. l., Raman spectra of pyridine adsorbed at a silver electrode. *Chem. Phys. Lett.* **1974,** *26* (2), 163-166.

138. Jeanmaire, D. L.; Van Duyne, R. P. J. J. o. e. c.; electrochemistry, i., Surface Raman spectroelectrochemistry: Part I. Heterocyclic, aromatic, and aliphatic amines adsorbed on the anodized silver electrode. *J. Electroanal. Chem.* **1977,** *84* (1), 1-20.

139. Sharma, B.; Frontiera, R. R.; Henry, A.-I.; Ringe, E.; Van Duyne, R. P. J. M. t., SERS: Materials, applications, and the future. *Mater. Today* **2012,** *15* (1-2), 16-25.

140. Chang, R., *Surface enhanced Raman scattering*. Springer Science & Business Media: 2013.

141. Stiles, P. L.; Dieringer, J. A.; Shah, N. C.; Van Duyne, R. P. J. A. R. A. C., Surface-enhanced Raman spectroscopy. *Annu. Rev. Anal. Chem.* **2008,** *1*, 601-626.

142. Camden, J. P.; Dieringer, J. A.; Wang, Y.; Masiello, D. J.; Marks, L. D.; Schatz, G. C.; Van Duyne, R. P. J. J. o. t. A. C. S., Probing the structure of single-molecule surface-enhanced Raman scattering hot spots. *J. Am. Chem. Soc.* **2008,** *130* (38), 12616-12617.

143. Jensen, L.; Aikens, C. M.; Schatz, G. C. J. C. S. R., Electronic structure methods for studying surface-enhanced Raman scattering. *Chem. Soc. Rev.* **2008,** *37* (5), 1061-1073.

144. Yuen, J. M.; Shah, N. C.; Walsh Jr, J. T.; Glucksberg, M. R.; Van Duyne, R. P. J. A. c., Transcutaneous glucose sensing by surface-enhanced spatially offset Raman spectroscopy in a rat model. *Anal. Chem.* **2010,** *82* (20), 8382-8385.

145. Flood, A. H.; Stoddart, J. F.; Steuerman, D. W.; Heath, J. R. J. S., Whence molecular electronics? *Science* **2004,** *306* (5704), 2055-2056.

146. Kleinman, S. L.; Ringe, E.; Valley, N.; Wustholz, K. L.; Phillips, E.; Scheidt, K. A.; Schatz, G. C.; Van Duyne, R. P. J. J. o. t. A. C. S., Single-molecule surface-enhanced Raman spectroscopy of crystal violet isotopologues: theory and experiment. *J. Am. Chem. Soc.* **2011,** *133* (11), 4115-4122.

147. Nafie, L. A. J. C. p., Theory of resonance Raman optical activity: The single electronic state limit. *Chem. Phys.* **1996,** *205* (3), 309-322.

148. Atkins, P.; Barron, L. J. M. P., Rayleigh scattering of polarized photons by molecules. *Mol. Phys.* **1969,** *16* (5), 453-466.

149. Parchaňský, V.; Kapitán, J.; Bouř, P. J. R. A., Inspecting chiral molecules by Raman optical activity spectroscopy. *RSC Adv.* **2014,** *4* (100), 57125-57136.

150. Zhu, F.; Isaacs, N. W.; Hecht, L.; Barron, L. D. J. S., Raman optical activity: a tool for protein structure analysis. *Structure* **2005,** *13* (10), 1409-1419.

151. Polavarapu, P. L., *Chiral analysis: advances in spectroscopy, chromatography and emerging methods*. Elsevier: 2018.

152. Chulhai, D. V.; Jensen, L. J. T. J. o. P. C. A., Simulating surface-enhanced raman optical activity using atomistic electrodynamics-quantum mechanical models. *J. Phys. Chem. A* **2014,** *118* (39), 9069-9079.

153. Janesko, B. G.; Scuseria, G. E. J. T. J. o. P. C. C., Molecule− Surface Orientational Averaging in Surface Enhanced Raman Optical Activity Spectroscopy. *J. Phys. Chem. C* **2009,** *113* (22), 9445-9449.

154. Das, M.; Gangopadhyay, D.; Šebestík, J.; Habartová, L.; Michal, P.; Kapitán, J.; Bouř, P. J. C. C., Chiral detection by induced surface-enhanced Raman optical activity. *Chem. Comm.* **2021**.

155. Efrima, S. J. T. J. o. c. p., Raman optical activity of molecules adsorbed on metal surfaces: theory. *J. Chem. Phys.* **1985,** *83* (3), 1356-1362.
156. Efrima, S. J. C. p. l., The effect of large electric field gradients on the Raman optical activity of molecules adsorbed on metal surfaces. *Chem. Phys. Lett.* **1983,** *102* (1), 79-82.
157. Osińska, K.; Pecul, M.; Kudelski, A. J. C. P. L., Circularly polarized component in surface-enhanced Raman spectra. *Chem. Phys. Lett.* **2010,** *496* (1-3), 86-90.
158. Rocks, L.; Faulds, K.; Graham, D.; Parchaňský, V.; Bouř, P.; Blanch, E. W. J. N. c., Through-space transfer of chiral information mediated by a plasmonic nanomaterial. *Nat. Mater.* **2015,** *7* (7), 591-596.
159. Abdali, S.; Blanch, E. W. J. C. S. R., Surface enhanced Raman optical activity (SEROA). *Chem. Soc. Rev.* **2008,** *37* (5), 980-992.
160. Sun, X.; Kong, H.; Zhou, Q.; Tsunega, S.; Liu, X.; Yang, H.; Jin, R.-H. J. A. C., Chiral Plasmonic Nanoparticle Assisted Raman Enantioselective Recognition. *Anal. Chem.* **2020,** *92* (12), 8015-8020.
161. Gellman, A. J.; Huang, Y.; Feng, X.; Pushkarev, V. V.; Holsclaw, B.; Mhatre, B. S. J. J. o. t. A. C. S., Superenantioselective chiral surface explosions. *J. Am. Chem. Soc.* **2013,** *135* (51), 19208-19214.
162. Hazen, R. M.; Filley, T. R.; Goodfriend, G. A. J. P. o. t. N. A. o. S., Selective adsorption of L- and D-amino acids on calcite: Implications for biochemical homochirality. *Proc. Natl. Acad. Sci. U. S. A.* **2001,** *98* (10), 5487-5490.
163. Kokkin, D. L.; Zhang, R.; Steimle, T. C.; Wyse, I. A.; Pearlman, B. W.; Varberg, T. D. J. T. J. o. P. C. A., Au–S bonding revealed from the characterization of diatomic gold sulfide, AuS. **2015,** *119* (48), 11659-11667.
164. Radenković, S.; Antić, M.; Savić, N. D.; Glišić, B. Đ. J. N. J. o. C., The nature of the Au–N bond in gold (III) complexes with aromatic nitrogen-containing heterocycles: The influence of Au (III) ions on the ligand aromaticity. *New J. Chem.* **2017,** *41* (21), 12407-12415.
165. Huang, J.; Kim, F.; Tao, A. R.; Connor, S.; Yang, P. J. N. m., Spontaneous formation of nanoparticle stripe patterns through dewetting. *Nat. Mater.* **2005,** *4* (12), 896-900.
166. Kong, H.; Sun, X.; Yang, L.; Liu, X.; Yang, H.; Jin, R.-H., Chirality Detection by Raman Spectroscopy: The Case of Enantioselective Interactions between Amino Acids and Polymer-Modified Chiral Silica. *Anal. Chem.* **2020,** *92* (21), 14292-14296.
167. Mutalikdesai, A.; Zoabi, A.; Kumar, V. B.; Abu-Reziq, R.; Hassner, A.; Gedanken, A., Enantioselective Separation of Racemic Tryptophan with Sonochemically Prepared Egg Albumin Microspheres. *ChemistrySelect* **2018,** *3* (14), 4004-4008.
168. Tu, Q.; Eisen, J.; Chang, C. J. J. o. b. o., Surface-enhanced Raman spectroscopy study of indolic molecules adsorbed on gold colloids. *J. Biomed. Opt* **2010,** *15* (2), 020512.
169. Kuligowski, J.; El-Zahry, M. R.; Sánchez-Illana, Á.; Quintás, G.; Vento, M.; Lendl, B. J. A., Surface enhanced Raman spectroscopic direct determination of low molecular weight biothiols in umbilical cord whole blood. *Analyst* **2016,** *141* (7), 2165-2174.
170. Deng, Y.; Wang, M.; Zhuang, Y.; Liu, S.; Huang, W.; Zhao, Q. J. L. S.; Applications, Circularly polarized luminescence from organic micro-/nano-structures. *Light Sci. Appl.* **2021,** *10* (1), 1-18.
171. Liu, M.; Zhang, L.; Wang, T. J. C. r., Supramolecular chirality in self-assembled systems. *Chem. Rev.* **2015,** *115* (15), 7304-7397.

172. Shen, Y.; Zhou, J.; Liu, T.; Tao, Y.; Jiang, R.; Liu, M.; Xiao, G.; Zhu, J.; Zhou, Z.-K.; Wang, X. J. N. c., Plasmonic gold mushroom arrays with refractive index sensing figures of merit approaching the theoretical limit. *Nat. Commun.* **2013,** *4* (1), 1-9.

173. Bahramipanah, M.; Dutta-Gupta, S.; Abasahl, B.; Martin, O. J. J. A. n., Cavity-coupled plasmonic device with enhanced sensitivity and figure-of-merit. *ACS Nano* **2015,** *9* (7), 7621-7633.

174. Bao, J.; Liu, N.; Tian, H.; Wang, Q.; Cui, T.; Jiang, W.; Zhang, S.; Cao, T. J. R., Chirality enhancement using Fabry–Pérot-like cavity. *Research* **2020,** *2020*.

175. Guo, Y.; Jiang, S.; Chen, X.; Mattei, M.; Dieringer, J. A.; Ciraldo, J. P.; Van Duyne, R. P. J. T. J. o. P. C. C., Using a Fabry–Perot cavity to augment the enhancement factor for surface-enhanced raman spectroscopy and tip-enhanced Raman spectroscopy. *J. Phys. Chem. C* **2018,** *122* (26), 14865-14871.

176. Bhatt, G.; Bhattacharya, S. J. J. o. M., Biosensors on chip: a critical review from an aspect of micro/nanoscales. *J. Micro Nano-Manuf.* **2019,** *2* (2), 198-219.

177. Cui, X.; Qin, F.; Ruan, Q.; Zhuo, X.; Wang, J. J. A. F. M., Circular gold nanodisks with synthetically tunable diameters and thicknesses. *Adv. Funct. Mater.* **2018,** *28* (11), 1705516.